Accretion, winds and jets: High-energy emission from young stellar objects

Dissertation
zur Erlangung des Doktorgrades
des Departments Physik
der Universität Hamburg

vorgelegt von

Hans Moritz Günther

aus Hamburg

Hamburg
2009

Gutachter der Dissertation:	Prof. Dr. J. H. M. M. Schmitt Prof. Dr. E. Feigelson
Gutachter der Disputation:	Prof. Dr. P. H. Hauschildt Prof. Dr. G. Wiedemann
Datum der Disputation:	13.03.2009
Vorsitzender des Prüfungsausschusses:	Dr. R. Baade
Vorsitzender des Promotionsausschusses:	Prof. Dr. R. Klanner
Dekan der MIN Fakultät:	Prof. Dr. A. Frühwald (bis 28.02.2009) Prof. Dr. H. Graener (ab 01.03.2009)

Zusammenfassung

Sterne entstehen durch Gravitationsinstabilitäten in molekularen Wolken. Wegen der Erhaltung des Drehimpulses geschieht der Kollaps nicht sphärisch, sondern das Material fällt zunächst auf eine Akkretionsscheibe zusammen. In dieser Doktorarbeit wird hochenergetische Strahlung von Sternen untersucht, die noch aktiv Material von ihrer Scheibe akkretieren, aber nicht mehr von einer Staub- und Gashülle verdeckt sind. In dieser Phase nennt man Sterne der Spektraltypen A und B Herbig Ae/Be (HAeBe) Sterne, alle späteren Sterne heißen klassische T Tauri Sterne (CTTS); eigentlich werden beide Typen über spektroskopische Merkmale definiert, aber diese fallen mit den hier genannten Entwicklungsstadien zusammen. In dieser Arbeit werden CTTS und HAeBes mit hochauflösender Spektroskopie im Röntgen- und UV-Bereich untersucht und Simulationen für diese Stadien gezeigt.

Für zwei Sterne werden Röntgenspektren reduziert und vorgestellt: Der CTTS V4046 Sgr wurde mit *Chandra* für 100 ks beobachtet. Die Lichtkurve dieser Beobachtung zeigt einen Flare und die Triplets der He Isosequenz (Si XIII, Ne IX und O VII) deuten auf hohe Dichten im emittierenden Plasma hin. Die zweite Beobachtung enthält Daten für den HAeBe Stern HD 163296, die in 130 ks mit *XMM-Newton* gewonnen wurden. Diese Lichtkurve zeigt nur wenig Aktivität und die Elementhäufigkeiten entsprechen dem für aktive Sterne üblichem Muster. Das Triplet von O VII ist vergleichbar mit koronalen Quellen, also beeinflussen weder hohe Dichten noch ein starkes UV Feld die Emission.

Aus diesen und ähnlichen Beobachtungen, läßt sich schließen, dass mindestens drei Prozesse zur hochenergetischen Emission vom CTTS beitragen: Zum Einen haben diese Sterne aktive Koronen ähnlich denen normaler Hauptreihensterne, zum Zweiten bildet sich ein starker Akkretionsschock auf der Sternoberfläche, der das von der Scheibe einfallende Material auf mehrere Millionen Kelvin heizt und zum Dritten haben manche CTTS energiereiche Jets. Schocks in diesen Jets können das Material so weit erwärmen, dass es im Röntgenbereich leuchtet. Koronen sind bereits gut studiert; für die anderen beiden Mechanismen werden in dieser Arbeit Modelle vorgestellt. Der Akkretionsschock wird in einem ein-dimensionalen Modell behandelt, welches aber kein Ionisationsgleichgewicht voraussetzt. Die Vereinfachung auf nur eine Dimension ist zulässig, weil das Magnetfeld Bewegungen senkrecht zur Feldrichtung unterdrückt. Die Strahlungsverluste des als optisch dünn angenommenen Gases werden mit CHIANTI berechnet. Eine Kombination aus diesem Modell und koronalem Gas wird an die Beobachtungen von TW Hya und V4046 Sgr angepasst. Für beide Sterne reichen relativ geringe Massenakkretionsraten, um die Röntgenleuchtkraft zu erklären (2×10^{-10} $M_\odot$/yr bzw. 3×10^{-11} $M_\odot$/yr).

In dieser Arbeit wird ein Modell vorgestellt, das die weiche Emission in der Umgebung von DG Tau durch Schockwellen entlang des Jets erklärt. Schockgeschwindigkeiten zwischen 400 und 500 km s^{-1} sind notwendig, um das beobachteten Spektrum zu erzeugen. Bei Dichten $> 10^5$ cm^{-3} ist die Ausdehnung des Schocks so klein, dass erklärt ist, warum er in optischen Beobachtungen nicht entdeckt wird.

Da im Röntgenbereich die spektrale Auflösung nicht für eine Linienprofilanalyse ausreicht, werden UV Daten dafür herangezogen. Die Linienprofile im UV Bereich der mit *FUSE* beobachteten CTTS sind bis zu 500 km s^{-1} breit. Vermutlich tragen Akkretion und Winde zu der Emission bei, aber im Moment können die Akkretionsmodelle die Linienprofile, besonders die Breite, noch nicht erklären.

HAeBe Sterne besitzen heißes, koronales Plasma, genau wie CTTS. Akkretionsschocks tragen kaum zur Emission bei; das Triplet von O VII weist auf einen Ursprung in Jets ähnlich wie bei DG Tau hin. Ein vergleichbares Modell kann auch hier die Röntgenemission erklären.

Abstract

Stars form by gravitational collapse from giant molecular clouds. Due to the conservation of angular momentum this collapse does not happen radially, but the matter forms circumstellar disk first and is consequently accreted from the disk onto the star. This thesis deals with the high-energy emission from young stellar objects, which are on the one hand still actively accreting from their disk, and on the other hand are no longer deeply obscured by their natal cloud. Stars of spectral type B and A are called Herbig Ae/Be (HAeBe) stars in this stage, all stars of later spectral type are termed classical T Tauri stars (CTTS); strictly speaking both types are defined by spectroscopic signatures, which are equivalent to the evolutionary stage described above. In this thesis CTTS and HAeBes are studied through high-resolution X-ray and UV spectroscopy and through detailed physical simulations.

Spectroscopic X-ray data is reduced and presented for two targets: The CTTS V4046 Sgr was observed with *Chandra* for 100 ks, using a high-resolution grating spectrometer. The lightcurve contains one flare and the He-like triplets of Si XIII, Ne IX and O VII indicate high densities in the X-ray emitting regions. The second target is the HAeBe HD 163296, which was observed with *XMM-Newton* for 130 ks. The lightcurve shows only moderate variability, the elemental abundance follows a pattern, that is usual for active stars. The He-like triplet of O VII exhibits line ratios similar to coronal sources, indicating that neither a high density nor a strong UV-field is present in the region of the X-ray emission.

Using these and similar observations, it can be concluded that at least three mechanisms contribute to the observed high-energy emission from CTTS: First, those stars have active coronae similar to main-sequence stars, second, the accreted material passes through a strong accretion shock at the stellar surface, which heats it to a few MK, and, third, some CTTS drive powerful outflows. Shocks within these jets can heat the matter to X-ray emitting temperatures. The first is already well characterised; for the latter two scenarios models are presented in this thesis. The accretion shock is treated in a stationary 1D model, taking non-equilibrium ionisations explicitly into account. The magnetic field is strong enough to suppress motion perpendicular to the field lines, so the use of a 1D geometry is justified. The radiative loss is calculated as optically thin emission with the CHIANTI database. A combination of simulated post-shock cooling zone spectra and coronal gas is fitted to the observations of the CTTS TW Hya and V4046 Sgr. Both stars require only small mass accretion rates to power the X-ray emission (2×10^{-10} $M_\odot$/yr and 3×10^{-11} $M_\odot$/yr, respectively).

The CTTS DG Tau is heavily absorbed and the observed soft X-ray emission originates spatially offset from the star. In this thesis a physical model is presented which explains the emission by a shock front travelling along the ejected jet. Shock velocities between 400 and 500 km s^{-1} are required to explain the observed spectrum. For a electron density $> 10^5$ cm^{-3} all shock dimensions are so small that they remain undetectable in optical observations as observed.

The spectral resolution in X-rays is not sufficient to analyse the line profiles, so UV data is used for this purpose. Line profiles extend up to 500 km s^{-1} in sample of CTTS observed with *FUSE*. Likely contribution from both, infalling and outflowing gas, contributes to the observed emission. The current models do not explain the observed line profiles in detail, especially the line width causes problems.

HAeBe stars have hot plasma, which can only be explained as an active corona, similar to the CTTS. Accretion does not contribute significantly to the X-ray emission, instead the line ratios in the He-like triplets point to an origin in the outflows, similar to the CTTS jets. A model comparable to DG Tau reproduces the observed emission.

Contents

Chapter 1

Introduction

Compared to human life the sky seems to be eternal, revolving without change around the celestial pole. Still, people observed comets or "shooting stars" already early in the evolution of mankind and interpreted them, depending on their culture, either as happy or evil omen. Also, within just a few nights each observer will recognise that our Sun, the moon and the planets move along the celestial sphere with respect to the stars. The stars themselves, however, appear immortal. Only rare events, such as galactic supernovae, the death of a massive star, can be seen by the naked eye. One of the most prominent observations of this sort was the supernova (SN) in 1054, which is mentioned in a number of contemporary sources. The most noted observations were recorded by Chinese astronomers of the Song and the Liao dynasty, but more recently also Japanese and European documents have been uncovered with hints on this SN. These sightings, distributed over several months, allow us today to determine the date of the explosion and even reconstruct the lightcurve, so that the type of the SN according to the modern classification scheme can the established (Collins et al. 1999). Today that specific object is the beautiful Crab Nebula. More historic SN include the SN 1572 and SN 1604, which were observed by Tycho Brahe and Johannes Kepler respectively.

Other evolutionary stages in the life of stars develop on much longer time scales and are thus not directly visible within a human lifespan. It was not until the middle of the last century that astronomers discovered the early stages of stellar evolution.

Still, the birth of stellar and planetary systems only takes a few million years. Thus all star forming regions which provide us with beautiful pictures today (Fig. 1.1 to 1.3) did not exist when the last dinosaurs walked on earth or even the first modern birds or mammals evolved.
In this chapter an overview of the stellar lifecycle is given with particular emphasis on the early stages of stellar evolution and the development of low-mass stars. Specific observations and models corresponding the evolutionary phases of special importance to this thesis will be discussed in Chapter 2.

1.1 From clouds to stars

Not all baryon mass of our galaxy is contained in luminous stars, about half of it remains in the interstellar medium and in turn a significant portion of that resides in dense and cool molecular clouds. Along the galactic equator these clouds are seen as black spots, obscuring the light of background stars. They are relatively cool with temperatures of ten Kelvin in the interior to thousand Kelvin at the outer boundaries, where they are illuminated by other stars. One example of such a cloud is shown in Fig. 1.1. These objects consist mostly of hydrogen in molecular form, the most abundant element in the cosmos, but a surprisingly large range of other molecules also forms under these conditions. Some of the elements condense on dust grains and in turn the grain surface provides an environment for more chemical reactions. These clouds are not static, but constantly in motion. Strong, cool flows can disturb their structure and in recent years the importance of turbulence has been discovered. If parts of the cloud are sufficiently cold, they collapse due to self-gravity. A sim-

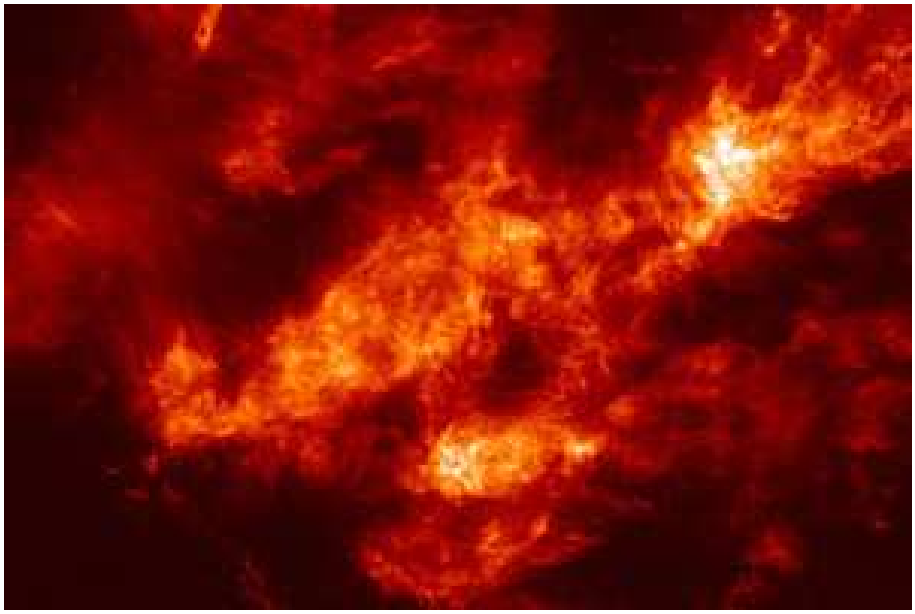

Figure 1.1: An image of the Taurus molecular cloud, one of the closest star forming regions in infrared light. Credits: Five College Radio Astronomy Observatory/Gopal Narayanan/Mark Heyer

ple criterion for the critical mass, given the temperature and thus the thermal pressure was provided by J. Jeans. The higher the temperature, the higher is the critical mass, because the thermal pressure counteracts the gravitational contraction. If the mass exceeds the so-called Jeans mass, the collapse to a first proto-star happens relatively fast on a time scale of only 10^5 years. The matter is heated up by compression and eventually the thermodynamical pressure slows down the infall and stops the contraction. In this phase the objects can only be seen in infrared (IR) light, because they are deeply hidden within the molecular cloud and in all other wavelength regimes the extinction is far too high to detect these sources with current instruments. In this stage they are called class I IR sources.

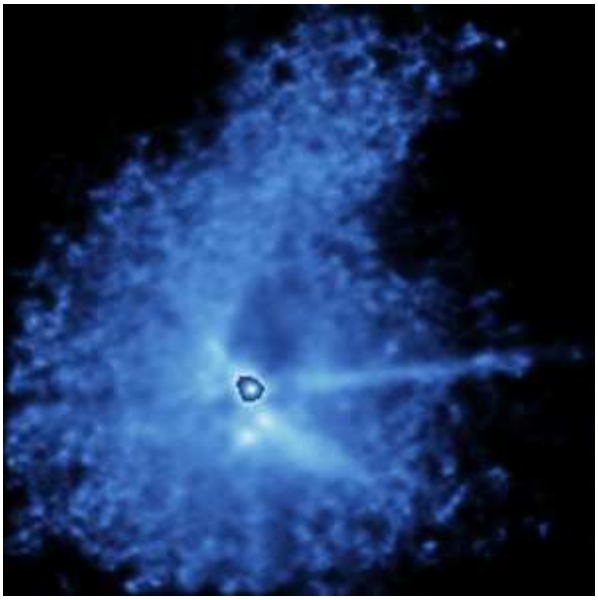

Figure 1.2: False-colour image of the T Tau binary system. The disk is inhomogeneous and some indications of outflow structures can be seen from the central star to in opposite directions (to the upper left and lower right). Credit: C. & F. Roddier (IfA, Hawaii), CFHT

Many of these have powerful bipolar outflows, taking the form of highly collimated jets (Fig. 1.2). These jets inject mass and momentum back in its parent natal cloud, possibly an important contribution to its energy budget (e. g. Banerjee et al. 2007). They also drive the subsonic turbulence that is observed in the cloud material. Furthermore, the jets are fas-

Figure 1.3: False-colour image of the star forming region W5 from *Spitzer*. Red is dust, white and green mark hot gas. The young, massive, hot stars in white cones possibly trigger further star formation, when the hot gas streams out and compresses the surrounding cloud. Credit: Lori Allen, Xavier Koenig (Harvard-Smithsonian CfA) et al., JPL-Caltech, NASA

cinating objects in their own right. Along the jet direction several shocks can develop when faster material catches up with slower material and where the jet interacts with the interstellar medium a bow shock heats up the material. All these shocks can be observed as diffuse emission regions in Hα, the so-called Herbig-Haro objects, and their pictures belong to the most beautiful objects in our cosmos. All the time the matter keeps falling in from the surrounding envelope, but due to the conservation of angular momentum the matter cannot accrete directly on the star, instead it builds up a disk approximately in Keplerian rotation around the central object. The residual gas and dust in the envelope is either accreted onto the disk or blown out of the system by stellar winds and outflows. In this stage the stars become optically visible, they are now termed classical T Tauri stars (CTTS) or class II IR sources. The proto-typical system of this class is T Tau itself (Fig. 1.2). Similar to the original cloud the disk consists of gas and dust grains. Its surface is irradiated by the galactic UV background and from the central star, consequently it can reach a few thousand Kelvin. The disk-midplane is much cooler, protected by the outer layers and over time the dust settles gravitationally down there. This is the environment of planet formation, but the exact growth mechanism is not yet clear. Small grains will grow through coagulation, in other words, they stick together after collisions. When they reach sufficient mass gravity can help to pull more proto-planetesimals together. At the same time the planets can migrate inwards or outwards, depending on the physical conditions in the disk. The time scale of disk-dispersal sets the time available for planet formation and migration.

Three processes take matter from the disk: Some of it is accreted onto proto-planets, some is accreted onto the central star and the rest is blown out of the system by the combined pressure of radiation, and the stellar and disk winds. When the circumstellar envelope ceases to supply matter to the disk these processes reduce the disk mass of the system. Eventually, after a few Myr the disk becomes thin, and the mass accretion rate onto the central star drops. This system has now reached the phase of the

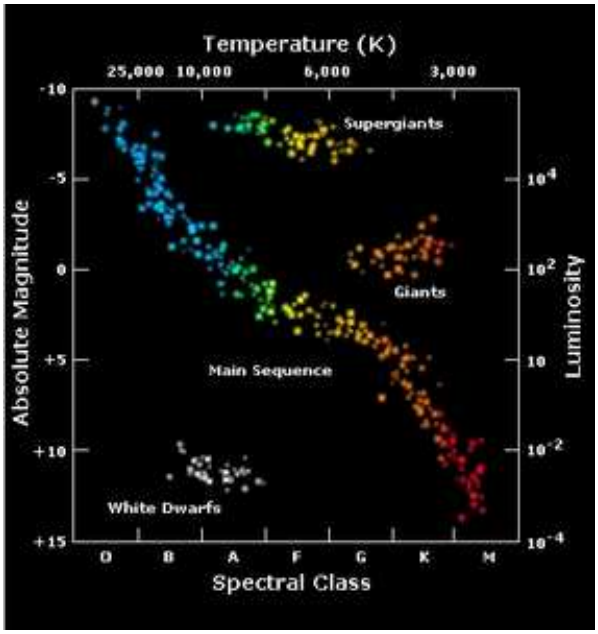

Figure 1.4: Schematic Hertzsprung-Russel (HR) digram. Credit: ESA

weak-lined T Tauri stars (WTTS), which are class III IR sources.

Through all this time the star continues to contract and consequently its core temperature rises. During the T Tauri phase it already burns deuterium in its interior. Still, it further contracts, until the temperature required for fusion of hydrogen is reached. Then the star stabilises for a time much longer than its evolution to this point took.

1.2 The main-sequence

The star is now said to be on the main-sequence (MS) and stays in hydrostatic equilibrium, as long as the fusion process can supply sufficient energy to balance the energy lost to radiation. Stars of higher mass are much brighter and hotter than low mass stars; this is conventionally displayed on a Hertzsprung-Russel (HR) diagram (Fig. 1.4). The lower mass stars reside in the lower, right corner of the diagram, they shine in red with luminosities comparable to the sun or below.

Stars of high mass (upper left in Fig. 1.4) are much brighter than the cool stars, therefore, they use up their energy budget much faster. The lifetime on the MS of an O-type star with $10^4 - 10^5$ times the solar luminosity can be less then 10^7 years, whereas the sun will stay on the MS for roughly 10^{10} years and lower mass stars even longer. This fact is used to determine the age of stellar populations: The most massive star still on the MS indicates the age of e. g. a stellar cluster.

1.3 The last phases in stellar life

When stars with a mass below roughly 2.5 solar masses reach the end of their lifetime on the MS, the hydrogen burning in their core ceases and cannot supply sufficient pressure any longer to keep the star in equilibrium. It ascends to the giant branch, because the star collapses until the electrons in the core are Fermi-Dirac degenerated and the temperatures reach values high enough to burn helium. In a so-called Helium-flash the brightness of the star increases by several orders of magnitude and the high core temperature reverses the electron degeneration, the stars move up in the HR-diagram into the region of the Giants. A stable phase with core helium burning and a surrounding shell of hydrogen burning develops with a lower luminosity. During this time the star loses a significant portion of its mass. The star again increases in brightness when the helium burning is not possible in the core any longer, but just in an outer shell. This state is called “asymptotic giant branch”. The burning is unsteady and the star ejects shells, which form planetary nebulas. After the exhaustion of hydrogen and helium burning the star contracts until only the quantum-mechanical effect of an degenerated electron gas can stop further compression. This is the stage of a white dwarf, the last phase of stellar evolution for low mass stars (on the bottom left in Fig. 1.4).

More massive stars can explode in super-nova explosions which eject large quantities of mass in the interstellar medium enriched with heavy elements. The ejecta mix with the gas clouds and from this reservoir the next generation of stars and planetary systems can form.

Chapter 2

Young stars

This chapter gives an overview of two classes of young pre-main-sequence (PMS) objects: The CTTS already mentioned above and the Herbig Ae/Be (HAeBe) stars. On the one hand, CTTS are low mass ($M_* < 3M_\odot$), cool stars with a convective envelope, mostly of spectral type G to K. Some authors encompass a wider range of objects in this class from F to M, the former are often called intermediate mass T Tauri stars. CTTS are traditionally defined by a spectroscopic signature, their Hα equivalent width has to be larger than 10 Å, those stars with lower values are termed WTTS. Many TTS are time-variable objects and their Hα line fluctuates around the dividing line. Therefore, a more physical definition distinguishes between CTTS as objects which are actively accreting material from a circumstellar disk and WTTS, also called naked TTS (NTTS), where the accretion has already ceased and the disk is thin or even absent.

On the other hand, HAeBes are PMS objects of spectral type A or B with emission lines. In many respects they are similar to the CTTS: Both types accrete material, although the accretion mechanism may be different in the more massive stars. HAeBes do not have a convective envelope, so they cannot generate magnetic fields in a solar-like dynamo. HAeBes are much more luminous, but due to the faster evolution and the smaller number of A and B-type stars less HAeBes have been studied in detail. Even more massive stars of O-type cannot be observed in a stage comparable to the CTTS and HAeBes, since their evolution is so fast that they are completely covered by the molecular cloud until they reach the MS.

In this chapter observational characteristics and theoretical explanations for the observed phenomena of CTTS (Sect. 2.1) and HAeBes (Sect. 2.2) are presented. Although the level of detail has increased in the observations and better models have been developed in recent years, many open questions remain. Some of them are tackled in this thesis and those are collected in Sect. 2.3. Sect. 2.4 provides a short introduction into the observational methods of X-ray astronomy, the tool employed in most chapters of this thesis.

2.1 Classical T Tauri stars

The majority of this thesis deals with observations and models of CTTS in the high energy regime. Section 2.1.1 summarises the observational characteristics of CTTS, before Sect. 2.1.2 explains our current understanding of accretion related phenomena and Sect. 2.1.3 the theories of outflows.

2.1.1 Observations

Disks

CTTS are still surrounded by circumstellar disks, as evidenced by the IR excess. Interferometric radio observations show that these disks do not reach down to the stellar surface, but are truncated at a few stellar radii as Eisner et al. (2006) proved for the best-studied CTTS TW Hya.

The upper layers of its disk are heated by the stellar radiation to about 2 000-3 000 K and even the molecular hydrogen in the surface is radiatively excited to the rotational-vibrational states, mostly by the stellar Lyα radiation.

The decay to the ground state can be observed in the UV and FUV by the *Hubble Space Telescope (HST)*/STIS and the *Far Ultraviolet Spectroscopic Explorer (FUSE)* (Herczeg et al. 2002, 2004). Recent adaptive optics observations in the IR allow to trace molecular hydrogen further out from the central star for several CTTS (Beck et al. 2008), but it is unclear if the gas resides in a disk or is ejected in a wind and how it is heated. It is generally expected that the disks of CTTS are the environments of planet formation, but the stellar variability introduces great uncertainties in the usual methods to detect planets. Setiawan et al. (2008) arouse great interest, when they announced the existence of a planet orbiting the CTTS TW Hya, based on high-resolution spectroscopy. In follow-up observations other groups could not confirm the detection, e. g. the proposed period vanished in space-based photometry from the Canadian *MOST* mission in a second observing run (Rucinski et al. 2008) and also other ground-based radial velocity measurements favour a cool spot on the stellar surface over a hot Jupiter as the most likely cause of the observed radial-velocity variations (Huélamo et al. 2008).
Nevertheless there is evidence from 7 mm radio observations that the dust grains in the disks around older CTTS have grown to pebbles with sizes of the order of a few cm (Testi et al. 2003; Rodmann et al. 2006). Schegerer et al. (2006) looked for the signatures of more complex materials and found emission of crystalline silicates in circumstellar disks of CTTS.

Outflows

Undoubtly there is a cool wind, which can be seen in forbidden optical lines (Lamzin et al. 2004), ejected from the disk and most likely the star. The temperature of the stellar wind in TW Hya is still a matter of debate. Dupree et al. (2005) argue that it can reach the formation temperature of O VI (300 000 K) based on FUV data, but Johns-Krull & Herczeg (2007) show this to be an unlikely explanation of the observed line profiles. A useful probe is the He I line at 10830 Å. Edwards et al. (2003, 2006) use it to study a larger sample of CTTS, and find a relation between the wind acceleration and the accretion, where the inflow could ultimately power the outflow. Some CTTS like DG Tau and RW Aur even show highly collimated outflows, which are often bipolar. In the outflows several "knots" develop, where internal shocks heat up the gas, so that it radiates in optical lines, mostly in Hα; they are called Herbig-Haro (HH) objects. In some cases line shifts and proper motion studies allow to measure their velocity and trace the jet back to the central star. In crowded star forming regions this can be ambiguous and most large outflows are driven by younger objects, but McGroarty & Ray (2004) identify five CTTS, whose outflows reach distances larger than a parsec from the star. More common are micro-jets which extend only a few hundred AU. High spatial resolution either from space-based instruments or by adaptive optics is needed to resolve the structures on small scales. Fig. 2.1 shows combined images from spectro-astrometry with *HST*/STIS, where long slit spectra were taken on seven slightly displaced slit positions on the sky. The images combined from different wavelengths corresponding to different radial velocities show that the fast components of the jet are more collimated than the slower flows and reach deprojected velocities up to 600 km/s. In some younger objects and also in the CTTS DG Tau X-ray emission could be resolved in the jet. Up to 5″ from the central star, that is $\approx$ 1000 AU deprojected with the inclination of the jet at the distance of DG Tau, emission could be detected (Güdel et al. 2005, 2008). On the other extreme, Schneider & Schmitt (2008) resolved a significant offset of only 50 AU between the soft X-ray emission and the hard, stellar component.

The compostion of the outflows from CTTS is uncertain, specifically their gas-to-dust ratio could deviate from the interstellar medium. Several driving mechanisms for winds and outflows are possible and consequently different launching regions. The disk can launch a cool, molecular, wide-angle outflow (Takami et al. 2004), stellar winds possibly have higher temperatures.

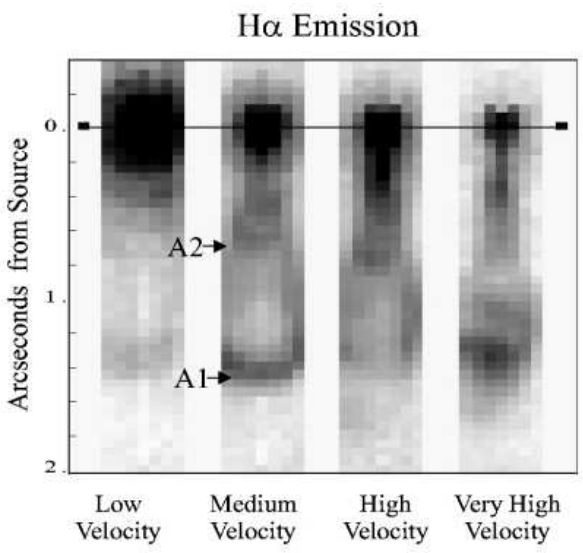

Figure 2.1: Image of the DG Tau jet taken with the *HST*. Within 1″ of DG Tau the faster components are more collimated. "Very high velocity" here means ≈ 400 km/s on the plane of the sky. Taken from Bacciotti et al. (2000).

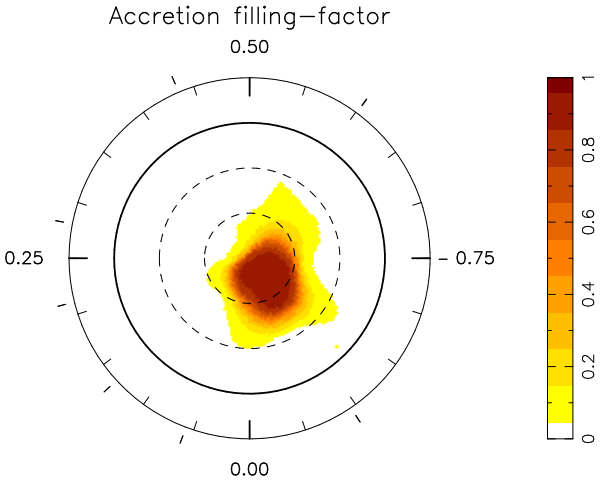

Figure 2.2: Map of the local accretion filling factor on V2129 Oph derived from combined fits to Zeemann-signatures or photospheric lines and the Ca II IR triplet. Taken from Donati et al. (2007).

Accretion

The disk is truncated by the stellar magnetic field at a few stellar radii roughly at the corotation radius. The inner disk rim is ionised and due to the Lorentz-force the matter follows the magnetic field lines. These funnels emit in lines of hydrogen. Often the Balmer series, Paβ and Brγ line profiles are observed to deduce the accretion geometry and estimate the mass flux rate through the funnels onto the stellar surface (Muzerolle et al. 1998a,b; Lawson et al. 2004). The average temperature in the funnels from this data is 6 000 to 10 000 K. Bary et al. (2008) present observations in the IR of the Brackett and Paschen series. They explain the observed line ratios with a relatively cool gas of only 1 000 K, which is photoexcited by the energetic stellar radiation.

The footpoints of the accretion funnels on the stellar surface can now be mapped with Doppler-imaging techniques, an example is given in Fig. 2.2. The surface filling factor f, the fraction of the stellar surface, that is covered by the accretion footpoints, is typically a few percent or less.

On the stellar surface a strong shock develops, which converts most of the kinetic energy of the infalling material into heat; the post-shock gas reaches a few 10^6 K. After passing through the shock front the plasma cools down radiatively. This cooling radiation can be observed in X-rays and other spectral bands. A review of the observational situation before the advent of high-resolution grating spectroscopy with the current generation of X-ray telescopes on *XMM-Newton* and *Chandra* is given by Feigelson & Montmerle (1999). Kastner et al. (2002) presented the first grating spectrum of a CTTS. They observed TW Hya, the closest object of its kind with a distance of 57 pc. Contrary to the known spectra of stellar coronae the He-like triplet of O VII shows a very low ratio of the forbidden (f) to intercombination (i) line, this can be caused by strong UV-fields or high densities in the emission region. The stellar radiation field is too weak to explain this effect, so Kastner et al. (2002) attribute it to the post-shock accretion zone. Since, this line ratio has been confirmed in an *XMM-Newton* observation of TW Hya (Stelzer & Schmitt 2004) and similar, although less extreme, line ratios have been observed in other CTTS (BP Tau (Schmitt et al. 2005), V4046 Sgr (Chapter 3), MP Mus (Argiroffi et al. 2007) and RU Lup (Robrade & Schmitt

2007)). A notable exception is the higher mass system T Tau (Güdel et al. 2007b).
Depending on the exact geometry of the post-shock cooling zone, some of the radiation does not escape, but heats the underlying photosphere. This produces an additional continuum from the UV to the IR, which raises the level of the photospheric continuum. Thus the spectral lines seem to be filled-up in continuum normalised spectra relative to MS-stars of the same spectral type. This effect is called "veiling". Similar to line emission the amount of veiling present in a system can also be used to estimate the mass accretion rate.

The star itself

In the early days of X-ray observations with *Einstein* the source identification of at least some sources in crowded star forming regions was ambiguous (Feigelson & Decampli 1981) and with *ROSAT* there was still a considerable amount of source confusion, and the spectral characterisation had to rely on coarse spectra (Feigelson & Kriss 1989; Neuhäuser et al. 1995), but now surveys of star forming regions with the new generation of instruments are available. Two prominent examples are the "Chandra Orion Ultradeep Project (COUP)", which identified more than a thousand sources and delivered a large number of lightcurves for variability analysis and CCD spectra suitable for fits of two-temperature models (Preibisch et al. 2005) and the "XMM-Newton extended survey of the Taurus molecular cloud (XEST)", where a larger region of the sky was sampled in short exposures and a few targets have additional grating spectroscopy (Güdel et al. 2007a).
In many respects the central star behaves similar to MS analogues of the same spectral type. Generally young stars are more active and thus exhibit a higher level of X-ray activity. Nevertheless the X-ray luminosity in CTTS is only half of the luminosity observed in the slightly more evolved WTTS (Preibisch et al. 2005). The reason for this difference is not yet clear. Gregory et al. (2007) suggest, that this difference might not be intrinsic, but due to absorption in the accretion columns. It has also been suggested, that the accreted matter cools down parts of the corona, but no detailed simulations have been published on this idea yet. Undoubtly CTTS show an excess of soft emission compared to MS stars of comparable luminosity (Robrade & Schmitt 2007; Güdel & Telleschi 2007).
CTTS posses strong magnetic fields on their surface, which cover a significant part of the photosphere. Johns-Krull et al. (1999) find an average surface field of 2.6 ± 0.3 kG on BP Tau using Zeemann-splitting, the fields on other CTTS are of the same order of magnitude (Valenti & Johns-Krull 2004; Yang et al. 2005), but on some stars they are not ordered on large scales. The observations are not well represented by a simple dipole, but require higher-order components (Donati et al. 2007).

2.1.2 The magnetically funnelled infall model

Uchida (1983) and Koenigl (1991) introduced the magnetically funnelled infall model for CTTS to overcome some shortcomings of the previously favoured boundary layer model, where the disk was believed to reach down to the stellar surface. Shu et al. (1994) developed in much detail the X-wind model, one model for the accretion onto dipolar field-lines, where simultaneously to the accretion process a wind is driven from the inner rim of the disk. In a simple dipole configuration the infall impacts at high stellar latitudes. Figure 2.3 shows a sketch of the geometry. For rotationally symmetric fields the accretion spot will take the form of ring at constant latitude, but observations of photometric variability in CTTS show that the funnels impact in distinct spots.
The large-scale accretion geometry is controlled by the stellar magnetic field, which is complex in reality, but the field strength of higher-order contributions drops faster than the dipole field with increasing distance to the star. The simulations of the full magneto-hydrodynamic equations from the inner disk edge to the stellar photosphere started off with dipole fields, investigating e. g. an inclination between the axis of rotation and the symmetry axis of the magnetic field (Romanova et al. 2004). More

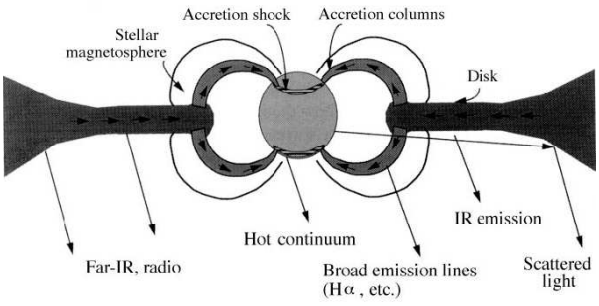

Figure 2.3: Model of disk accretion, taken from Hartmann (1998).

complicated fields showed different modes of accretion. For a combination of a dipole and a quadrupole field the emission might occur in hot spots at high latitudes and in the equatorial region simultaneously (Long et al. 2007).

Complementary are extrapolations of the stellar magnetic field, which is reconstructed with Zeemann Doppler-imaging. Assuming a potential field configuration the magnetic field lines can be calculated for a simple set of boundary conditions. Some field lines thread the disk and they can potentially carry an accretion stream. The footpoints of these field lines are distributed over the stellar surface and not all concentrated on high latitudes (Gregory et al. 2006; Jardine et al. 2008). Furthermore this technique shows the path of the accreting matter and thus the column density towards the star can be estimated (Gregory et al. 2007).

This all allows to estimate the infall velocity, which the material reaches, when it impacts on the stellar surface. Even the advanced simulations confirm that the impact velocity is basically given by the free-fall velocity, although some accretion funnels may be slowed down beforehand and loose kinetic energy to the magnetic field. Assuming a simple one-dimensional geometry of the accretion spot and a stationary post-shock cooling zone Calvet & Gullbring (1998) simulated the gas dynamics and found that the underlying photoshere is heated to roughly 20 000 K, enough to explain the optical veiling and the UV continuum excess. In fact, observations of the Balmer and Paschen continua can be used to constrain the mass accretion rate by comparison to these models. Lamzin (1998) developed a similar model, but he concentrated on the high-energy (line) emission. His X-ray spectra were synthesised for the resolution of the detectors on *ROSAT* and *ASCA* and thus do not resolve the density-sensitive He-like triplets, which turn out to provide a powerful diagnostic for the infall density (see Chapter 4). His model also treats the pre-shock zone, which gets ionised by the energetic radiation originating in the post-shock zone in much detail and predicts line ratios and line profiles, which can be used as a diagnostic of the physical conditions in this range (Gomez de Castro & Lamzin 1999; Lamzin 2003b,a). A step forward for the interpretation of X-ray spectra were simulations, which resolve individual lines and also combine accretion shock models with parameterisations of a stellar corona, which operates in addition to the accretion process. This work was done as part of this thesis and is presented in detail in Chapter 4. One potential problem is that the accretion shock might occur deep inside the stellar photosphere, where the densities are so high, that the X-ray radiation cannot escape (Drake 2005). This seems unlikely observationally, because lines of very different absorption cross sections (the recombination and the forbidden line in the He-like triplets) appear both as predicted in the optically thin model and new simulations of the time-dependent hydrodynamical equations by Sacco et al. (2008) in the stellar rest frame show the reverse shock, which moves outward into the accretion column, to be the one responsible for the generation of the X-rays, thus only little absorption is expected.

2.1.3 Properties and driving of jets and outflows

Observationally it is well established that CTTS drive outflows, possibly of multiple origin. Their radiation field is not strong enough to power line-driven winds as O-type stars do, but several other launching mechanisms seem plausible: Theories have been developed for stellar winds (Kwan & Tademaru 1988; Matt & Pudritz 2005), X-winds (Shu et al. 1994; Mohanty & Shu 2008) and disc winds

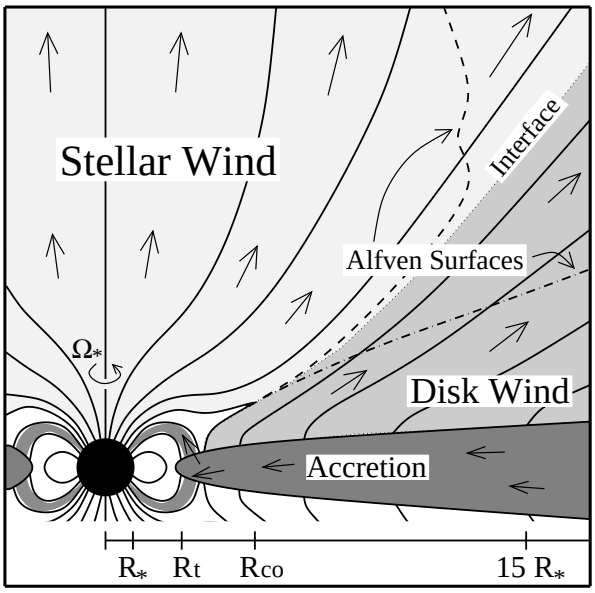

Figure 2.4: Sketch of the geometry in a system, where the outflow is a combination of a stellar and a disk wind, taken from Matt & Pudritz (2005).

(Blandford & Payne 1982; Anderson et al. 2005). In Fig. 2.4 a sketch is shown of a system with a stellar and a disk wind. The stellar wind escapes at higher latitudes and should be observed predominantly in systems, which are seen pole-on and the disk wind dominates in systems seen edge-on.

CTTS rotate far below their break-up velocity, although they actively accrete material with angular momentum from the disk. Next to disk-locking of the magnetic fields winds are a promising process to extract angular momentum from the system. In some systems the winds are collimated to form jets. The innermost component is the fastest and its velocity is just sufficient to heat matter to X-ray emitting temperatures in internal shocks (Chapter 7). Also jets and outflows may explain some of the peculiar line profiles observed in the UV range (Chapter 6).

Ferreira et al. (2006) discuss contributions from three components to the outflow in their models. They find a self-collimated disc wind, which confines a pressure-driven coronal stellar wind. Additionally, mass is ejected from the magnetopause in random intervals, which travels outward as hot "blob". There is no general consensus about the wind driving mechanism. It is easy to construct models for disk winds, but how to launch strong stellar outflows is unsolved. The model of pressure-driven coronal winds is questioned by Matt & Pudritz (2007), who argue that a wind of high temperature and high mass loss rate would produce X-ray emission orders of magnitude stronger than observed, thus pressure-driven winds can only contribute little to the total outflows. So far we only know that the only way to power a strong wind is by the accretion energy and in the conversion from inflows to outflows magnetic fields presumably play a role.

2.2 Herbig Ae/Be stars

HAeBes are no longer "cool" stars, they do not posses an outer convective envelope and thus are not expected to drive stellar activity as known from the sun. Still, studies of HAeBes indicate that a large fraction of this class actively emits X-rays (Skinner et al. 2004; Hamaguchi et al. 2005; Stelzer et al. 2006). In many cases this may be due to unresolved emission from an optically fainter companion in the same evolutionary state, that is a CTTS, but the detection rate of 70% (Zinnecker & Preibisch 1994) is not only much larger than the 10-15% found for field A-type stars (Schröder & Schmitt 2007), but X-ray emission is also detected in some systems, where even with *Chandra* and *HST* imaging no companion has been found.

The high luminosity of the central star makes HAeBes interesting targets for studies of the disk. It can be directly imaged with coronographic observations, e. g. using the *HST*. Observations separated by several years show differences in the appearance of the disk. In some of the observations morphological structures can be seen. This could be due to time variability in the inner disk rim (Wisniewski et al. 2008), which shadows some parts of the disk, thus they are not observed in scattered stellar light. Studies of this kind bear the potential to discover the planets or proto-planets through their gravitational influence on the surrounding disk. The existence of planets

around MS stars is now fully established, however, there is still some uncertainty to the formation scenario and the youngest system that can possibly harbour a planet. Observations of the disk structure and the grain size distribution also help in planet formation theories.

Some HAeBes drive powerful outflows with apparently time variable outflow velocities. In the HAeBe HD 163296 nine knots are known, two on the one side and seven on the other. This asymmetry is intrinsic and not only due to asymmetries in the sourrounding interstellar medium (Wassell et al. 2006).

HAeBes resemble CTTS in many respects: They both posses evolved proto-planetary disks, both actively accrete matter from a disk, both drive outflows and both are detected in X-rays. HAeBes appear as the more massive brothers of the CTTS. Looking in detail a few differences turn up, for example is the magnetic field of the HAeBes not strong enough to support magnetically funnelled accretion, instead the matter is expected to rain mostly radially down onto the photosphere. Consequently there is no strong accretion shock.

So far three HAeBes have been observed with X-ray grating spectroscopy: AB Aur (Telleschi et al. 2007), HD 104237 (Testa et al. 2008) and HD 163296, which is presented in Chapter 8. HD 104237 has a known, but unresolved companion, but the other two stars seem to be single to the best of our knowledge. The X-ray generation in HAeBes should be quite different to CTTS, due to the absence of a solar-like dynamo. Still, a corona could be powered by decaying primordial fields. Chapter 8 of this thesis analyses a deep exposure taken with *XMM-Newton*. The signal is better than in the observation of AB Aur and –in contrast to HD 104237– there are no indications of a close companion. The aim of this observation is to clarify the origin of intrinsic X-rays from HAeBes. This requires a good signal-to-noise ratio. This observation supports some of the conclusions drawn for the other two HAeBes, but improves critically upon the He-like triplet of O VII, which allows to rule out a number of otherwise promising scenarios.

2.3 Open questions

This section summarises some of the open questions and problems in the field of high-energy processes in star formation. In the following chapters these questions are addressed through a combination of observational and theoretical work. There is now a general agreement on some of the solutions, other lines of reasoning are still actively persued. The contribution of the specific work presented in this thesis is finally summarised in Sect. 9.

2.3.1 What are the X-ray properties of CTTS?

A large number of CCD-spectra of CTTS with medium energy resolution were obtained by surveys of star forming regions, but only few CTTS have been observed with X-ray grating spectroscopy. With a small sample size there is always a probability to concentrate on peculiar objects. This seems to be the case here, because TW Hya, the best-studied CTTS, is also the one of the softest sources and exhibits the lowest f/i-ratio in the He-like triplets. It is thus important to increase the sample size and publish further observations. This was done as part of this thesis in Chapter 3, concentrating on the emission measure distribution, the elemental abundances and the line ratios in the He-like triplets.

2.3.2 Do the accretion shocks significantly contribute to the observed X-ray emission from CTTS?

The magnetically funnelled infall model for CTTS predicts accretion spots on the stellar surface, but the lightcurves of CTTS show flares similar to other active stars, thus accretion cannot be the only X-ray emission mechanism. In Chapter 4 a numerical model for the accretion shock is presented, which predicts spectral properties of the post-shock cooling gas and thus allows to fit a combination of accretion shock and coronal models to observed spectra. When this work was started, it was still questioned, if the accretion con-

tributes to the observed X-ray emission at all (Feigelson et al. 2002; Drake 2005). The analysis is done for TW Hya, because well-exposed spectra from *Chandra* and *XMM-Newton* are available in the archives. Chapter 5 applies the same method to V4046 Sgr.
CTTS show an excess of soft X-ray emission (Robrade & Schmitt 2007; Güdel & Telleschi 2007), which leads to a low ratio of the O VIII/O VII emission line ratio compared to MS stars. The O VII/O VI for CTTS is now higher than in MS stars, together these results are used to pin down the excess temperature in CTTS (Chapter 6).

2.3.3 Do accretion shocks significantly contribute to the observed UV emission from CTTS?

The spectra of CTTS in the UV range contain several emission lines of hot ions like C III, C IV and O VI. They are often several hundred km/s wide, much broader than expected from rotational and thermal broadening and show often asymmetric line profiles (Ardila et al. 2002; Herczeg et al. 2002). Their red wings could be due to emission from the accretion funnel in the pre- or post-shock region. Chapter 6 investigates this possibility in detail.

2.3.4 What is the nature of the CTTS winds and outflows?

Some CTTS show blue-shifted UV lines. This hints at an origin in an outflow. From line profiles the velocity of the outflows can be estimated and from the ionisation stage the temperature of the gas can be deduced, if the line is collisionally excited. Chapter 6 analyses these characteristics and discusses possible emission origins. As a second line of evidence the gas column density (from the X-ray absorption) and the dust content (from optical reddening) are compared.
The determination of the outflow properties can constrain the possible launching regions. This is important to decide between different theoretical models, which predict different mass and angular momentum loss rates.

2.3.5 What powers the X-ray emission of jets from CTTS?

In DG Tau X-ray emission is resolved not only a few arcseconds out in the jet, but also within hundred AU from the central source. The X-ray luminosity ultimately has to be driven from the kinetic energy of the jet, which is likely converted to heat by shocks. Chapter 7 discusses several scenarios, which can give rise to shocks, and their implications for the temporal evolution of the emission. Potentially, jets could also contribute to the X-ray emission from other CTTS in addition to the coronal and accretion component discussed above. In that respect the case of DG Tau is important to study these aspects in a system, where they can by spatially separated.

2.3.6 How do HAeBes differ from CTTS?

HAeBe stars share many properties with CTTS, but differ in others. In Chapter 8 observations of the HAeBe HD 163296 are presented and the full list of issues discussed for the CTTS is applied to the HAeBe stars: The emission measure distribution and the abundances of the emitting plasma; the contribution to the X-ray emission coming from a corona, an accretion shock and from jets; the role of the circumstellar environment and the soft excess. When I proposed this observations at the beginning of my doctoral work, no HAeBe X-ray grating spectrum was published yet, so it was unclear what to expect from the observations.

2.4 Observational methods of X-ray astronomy

Two chapters of this thesis present new observations from *Chandra* (Chapter 3) and *XMM-Newton* (Chapter 8) and none of the other chapters is purely theoretical, they all apply models to previously published data. Therefore, this section gives a short introduction into some observational aspects of X-ray astronomy. The wavelengths considered in this thesis are not observable from the ground, be-

cause the photons do not penetrate the atmosphere; instead space-based telescopes have to be used. These are operated by space agencies, often in multi-national collaborations. *Chandra* is a NASA mission with contributions from the ESA, whereas *XMM-Newton* is an ESA mission, where in turn the NASA contributed. Both observatories are open to proposals from astronomers all around the world and they are heavily oversubscribed, meaning that only one in seven or eight proposals can be observed. This limits the possibility to freely chose interesting targets. Additionally, the time scale to plan observations is long: HD 163296 was proposed in October 2006, accepted in December 2006 and observed in end of September 2007. The data analysis became possible, when the new calibration files were available in December 2007.

The current generation of X-ray telescopes, i. e. *XMM-Newton* and *Chandra* for the first time fly a combination of CCD detectors with intrinsic energy resolution and grating spectrometers. This has revolutionised our ability to interpret X-ray spectra, because only now the identification of individual spectral lines is possible and this technology also allows to obtain medium-resolution spectra from targets observed in imaging mode.

X-ray grating observations of CTTS, e. g. V4046 Sgr or stars in the Taurus molecular cloud, typically take 100-150 ks and still contain only a dozen counts in some crucial lines (Chapter 3). The analysis is usually limited by the low number of counts. Compared to optical or IR telescopes the collecting area of X-ray telescopes is small; the effective area of the gratings is less than 100 cm^2. (The effective area of the mirrors is an order of magnitude larger, but only one tenth of the photons is dispersed by the gratings.) The reason for the relatively small collecting areas is, that X-rays are difficult to focus. Lenses and mirrors, which work well in the optical cannot be used to focus X-rays. Instead, mirrors must be placed nearly parallel to the line-of-sight to focus the X-rays via grazing incidence reflections. This makes the area covered by a single mirror very small, and several of them must be nested. *Chandra* has four mirrors in total, *XMM-Newton* 58 mirrors per mirror module, but the *Chandra* mirrors are polished to higher precision and stacked more accurately. So *XMM-Newton* provides a larger collecting area, but *Chandra* a smaller point-spread function and therefore a better spatial resolution. The CCD detectors employed count single photons and provide an intrinsic energy resolution. This is used for DG Tau in Chapter 7. The spectral resolution of the grating spectra e. g. for the *Chandra*/HEG depends on the wavelength, a typical value is $R \approx 1000$. In *Chandra* and *XMM-Newton* the zeroth order and the dispersed spectra are recorded simultaneously. The direct beam (dispersion order zero) is stronger than the dispersed spectra, it can be used to construct lightcurves with a temporal resolution which would not be possible from the dispersed spectra alone.

Bibliography

Anderson, J. M., Li, Z.-Y., Krasnopolsky, R., & Blandford, R. D. 2005, ApJ, 630, 945

Ardila, D. R., Basri, G., Walter, F. M., Valenti, J. A., & Johns-Krull, C. M. 2002, ApJ, 567, 1013

Argiroffi, C., Maggio, A., & Peres, G. 2007, A&A, 465, L5

Bacciotti, F., Mundt, R., Ray, T. P., et al. 2000, ApJ, 537, L49

Banerjee, R., Klessen, R. S., & Fendt, C. 2007, ApJ, 668, 1028

Bary, J. S., Matt, S. P., Skrutskie, M. F., et al. 2008, ApJ, 687, 376

Beck, T. L., McGregor, P. J., Takami, M., & Pyo, T.-S. 2008, ApJ, 676, 472

Blandford, R. D. & Payne, D. G. 1982, MNRAS, 199, 883

Calvet, N. & Gullbring, E. 1998, ApJ, 509, 802

Collins, II, G. W., Claspy, W. P., & Martin, J. C. 1999, PASP, 111, 871

Donati, J.-F., Jardine, M. M., Gregory, S. G., et al. 2007, MNRAS, 380, 1297

Drake, J. J. 2005, in 13th Cambidge Workshop on Cool Stars, Stellar Systems and the Sun, 519–523

Dupree, A. K., Brickhouse, N. S., Smith, G. H., & Strader, J. 2005, ApJ, 625, L131

Edwards, S., Fischer, W., Hillenbrand, L., & Kwan, J. 2006, ApJ, 646, 319

Edwards, S., Fischer, W., Kwan, J., Hillenbrand, L., & Dupree, A. K. 2003, ApJ, 599, L41

Eisner, J. A., Chiang, E. I., & Hillenbrand, L. A. 2006, ApJ, 637, L133

Feigelson, E. D., Broos, P., Gaffney, III, J. A., et al. 2002, ApJ, 574, 258

Feigelson, E. D. & Decampli, W. M. 1981, ApJ, 243, L89

Feigelson, E. D. & Kriss, G. A. 1989, ApJ, 338, 262

Feigelson, E. D. & Montmerle, T. 1999, ARA&A, 37, 363

Ferreira, J., Dougados, C., & Cabrit, S. 2006, A&A, 453, 785

Gomez de Castro, A. I. & Lamzin, S. A. 1999, MNRAS, 304, L41

Gregory, S. G., Jardine, M., Simpson, I., & Donati, J.-F. 2006, MNRAS, 371, 999

Gregory, S. G., Wood, K., & Jardine, M. 2007, MNRAS, 379, L35

Güdel, M., Briggs, K. R., Arzner, K., et al. 2007a, A&A, 468, 353

Güdel, M., Skinner, S. L., Audard, M., Briggs, K. R., & Cabrit, S. 2008, A&A, 478, 797

Güdel, M., Skinner, S. L., Briggs, K. R., et al. 2005, ApJ, 626, L53

Güdel, M., Skinner, S. L., Mel'Nikov, S. Y., et al. 2007b, A&A, 468, 529

Güdel, M. & Telleschi, A. 2007, A&A, 474, L25

Hamaguchi, K., Yamauchi, S., & Koyama, K. 2005, ApJ, 618, 360

Hartmann, L. 1998, Accretion Processes in Star Formation (Accretion processes in star formation / Lee Hartmann. Cambridge, UK ; New York : Cambridge University Press, 1998. (Cambridge astrophysics series ; 32) ISBN 0521435072.)

Herczeg, G. J., Linsky, J. L., Valenti, J. A., Johns-Krull, C. M., & Wood, B. E. 2002, ApJ, 572, 310

Herczeg, G. J., Wood, B. E., Linsky, J. L., Valenti, J. A., & Johns-Krull, C. M. 2004, ApJ, 607, 369

Huélamo, N., Figueira, P., Bonfils, X., et al. 2008, A&A, 489, L9

Jardine, M. M., Gregory, S. G., & Donati, J. . 2008, ArXiv e-prints, 802

Johns-Krull, C. M. & Herczeg, G. J. 2007, ApJ, 655, 345

Johns-Krull, C. M., Valenti, J. A., & Koresko, C. 1999, ApJ, 516, 900

Kastner, J. H., Huenemoerder, D. P., Schulz, N. S., Canizares, C. R., & Weintraub, D. A. 2002, ApJ, 567, 434

Koenigl, A. 1991, ApJ, 370, L39

Kwan, J. & Tademaru, E. 1988, ApJ, 332, L41

Lamzin, S. A. 1998, Astronomy Reports, 42, 322

Lamzin, S. A. 2003a, Astronomy Reports, 47, 498

Lamzin, S. A. 2003b, Astronomy Reports, 47, 540

Lamzin, S. A., Kravtsova, A. S., Romanova, M. M., & Batalha, C. 2004, Astronomy Letters, 30, 413

Lawson, W. A., Lyo, A.-R., & Muzerolle, J. 2004, MNRAS, 351, L39

Long, M., Romanova, M. M., & Lovelace, R. V. E. 2007, MNRAS, 374, 436

Matt, S. & Pudritz, R. E. 2005, ApJ, 632, L135

Matt, S. & Pudritz, R. E. 2007, in IAU Symposium, Vol. 243, IAU Symposium, ed. J. Bouvier & I. Appenzeller, 299–306

McGroarty, F. & Ray, T. P. 2004, A&A, 420, 975

Mohanty, S. & Shu, F. H. 2008, ApJ, 687, 1323

Muzerolle, J., Calvet, N., & Hartmann, L. 1998a, ApJ, 492, 743

Muzerolle, J., Hartmann, L., & Calvet, N. 1998b, AJ, 116, 2965

Neuhäuser, R., Sterzik, M. F., Schmitt, J. H. M. M., Wichmann, R., & Krautter, J. 1995, A&A, 297, 391

Preibisch, T., Kim, Y.-C., Favata, F., et al. 2005, ApJS, 160, 401

Robrade, J. & Schmitt, J. H. M. M. 2007, A&A, 473, 229

Rodmann, J., Henning, T., Chandler, C. J., Mundy, L. G., & Wilner, D. J. 2006, A&A, 446, 211

Romanova, M. M., Ustyugova, G. V., Koldoba, A. V., & Lovelace, R. V. E. 2004, ApJ, 610, 920

Rucinski, S. M., Matthews, J. M., Kuschnig, R., et al. 2008, ArXiv e-prints

Sacco, G. G., Argiroffi, C., Orlando, S., et al. 2008, A&A, 491, L17

Schegerer, A., Wolf, S., Voshchinnikov, N. V., Przygodda, F., & Kessler-Silacci, J. E. 2006, A&A, 456, 535

Schmitt, J. H. M. M., Robrade, J., Ness, J.-U., Favata, F., & Stelzer, B. 2005, A&A, 432, L35

Schneider, P. C. & Schmitt, J. H. M. M. 2008, A&A, 488, L13

Schröder, C. & Schmitt, J. H. M. M. 2007, A&A, 475, 677

Setiawan, J., Henning, T., Launhardt, R., et al. 2008, Nature, 451, 38

Shu, F., Najita, J., Ostriker, E., et al. 1994, ApJ, 429, 781

Skinner, S. L., Güdel, M., Audard, M., & Smith, K. 2004, ApJ, 614, 221

Stelzer, B., Micela, G., Hamaguchi, K., & Schmitt, J. H. M. M. 2006, A&A, 457, 223

Stelzer, B. & Schmitt, J. H. M. M. 2004, A&A, 418, 687

Takami, M., Chrysostomou, A., Ray, T. P., et al. 2004, A&A, 416, 213

Telleschi, A., Güdel, M., Briggs, K. R., et al. 2007, A&A, 468, 541

Testa, P., Huenemoerder, D. P., Schulz, N. S., & Ishibashi, K. 2008, ApJ, 687, 579

Testi, L., Natta, A., Shepherd, D. S., & Wilner, D. J. 2003, A&A, 403, 323

Uchida, Y. 1983, in ASSL Vol. 102: IAU Colloq. 71: Activity in Red-Dwarf Stars, 625–+

Valenti, J. A. & Johns-Krull, C. M. 2004, Ap&SS, 292, 619

Wassell, E. J., Grady, C. A., Woodgate, B., Kimble, R. A., & Bruhweiler, F. C. 2006, ApJ, 650, 985

Wisniewski, J. P., Clampin, M., Grady, C. A., et al. 2008, ApJ, 682, 548

Yang, H., Johns-Krull, C. M., & Valenti, J. A. 2005, ApJ, 635, 466

Zinnecker, H. & Preibisch, T. 1994, A&A, 292, 152

Chapter 3

X-ray accretion signatures in the close CTTS binary V4046 Sagittarii

H. M. Günther, C. Liefke, J. H. M. M. Schmitt, J. Robrade and J.-U. Ness
Astronomy & Astrophysics, 459, L29 (2006)
The original publication is available at www.aanda.org

A&A 459, L29–L32 (2006)
DOI: 10.1051/0004-6361:20066306

Astronomy & Astrophysics

LETTER TO THE EDITOR

X-ray accretion signatures in the close CTTS binary V4046 Sagittarii

H. M. Günther[1], C. Liefke[1], J. H. M. M. Schmitt[1], J. Robrade[1], and J.-U. Ness[2]

[1] Hamburger Sternwarte, Gojenbergsweg 112, 21029 Hamburg, Germany
e-mail: moritz.guenther@hs.uni-hamburg.de
[2] Arizona State University, School of Earth and Space Exploration, Tempe, AZ, 85287-1404, USA

Received 28 August 2006 / Accepted 26 September 2006

ABSTRACT

We present *Chandra* HETGS observations of the classical T Tauri star (CTTS) V4046 Sgr. The He-like triplets of O VII, Ne IX, and Si XIII are clearly detected. Similar to the CTTS TW Hya and BP Tau, the forbidden lines of O VII and Ne IX are weak compared to the intercombination line, indicating high plasma densities in the X-ray emitting regions. The Si XIII triplet, however, is within the low-density limit, in agreement with the predictions of the accretion funnel infall model with an additional stellar corona. V4046 Sgr is the first close binary exhibiting these features. Together with previous high-resolution X-ray data on TW Hya and BP Tau, and in contrast to T Tau, now three out of four CTTS show evidence of accretion funnels.

Key words. X-rays: stars – stars: individual: V4046 Sagittarii – stars: pre-main sequence – stars: coronae – stars: activity

1. Introduction

T Tauri stars are young (age < 10 Myr), low-mass ($M_* < 3\ M_\odot$) stars evolving down to the main sequence in the Hertzsprung-Russell diagram; a detailed review of pre-main sequence stellar evolution is given by Feigelson & Montmerle (1999). The CTTS subclass shows signs of active accretion from a circumstellar disk as proven by strong infrared excess and a large Hα equivalent width (>10 Å). Current models of CTTS assume a dipolar stellar magnetic field, disrupting the disk near the corotation radius, where ionised material is loaded onto magnetic field lines and is accelerated to essentially free-fall velocity along a magnetic funnel (Shu et al. 1994). A shock is formed close to the stellar surface and the material passing through the shock is heated up to temperatures in the MK range. The accretion geometries for binaries are understood less well theoretically, but see Artymowicz & Lubow (1996).

The X-ray emission from TTS was first detected with the *Einstein* Observatory, and extensive X-ray studies of a variety of star forming regions were undertaken with *ROSAT*. However, to what extent the observed X-ray emission can actually be attributed to accretion processes remained unclear and is the subject of some debate, since a central result of stellar X-ray astronomy states that all "cool stars", i.e., stars with outer convective envelopes, are surrounded by hot coronae (Schmitt & Liefke 2004). The usual interpretation of this finding is that turbulence in the outer convective zone leads to the production of magnetic fields and the ensuing activity, making it natural to attribute the observed X-ray emission from CTTS to the phenomena of magnetic activity rather than of accretion.

Imaging studies with low/medium spectral resolution allow large samples of TTS to be studied simultaneously as was recently performed for the Orion nebula by the COUP project (Feigelson 2005). In such studies, stars with and without accretion disks are difficult to distinguish; however, statistical studies seem to indicate some differences between CTTS and those TTS without accreting disks (Stelzer et al. 2000; Stelzer & Neuhäuser 2001; Flaccomio et al. 2003).

Only with the high spectral resolution of grating spectra, as available for a few individual CTTS observed with *Chandra* and *XMM-Newton*, is it possible to identify spectroscopic signatures taht distinguish accretion and coronal emission and to reliably derive the physical properties of the emission region through temperature, density, and abundance diagnostics. Specifically, a high spectral resolution survey of 48 stellar coronae by Ness et al. (2004) showed that most of the coronal densities are compatible with the low-density limit within the error ranges.

Only two clear exceptions among cool stars are known to date, the CTTS TW Hya and BP Tau. In the *Chandra* HETGS spectrum of TW Hya, Kastner et al. (2002) found unusually high densities and interpreted them as the signature of an accretion funnel; this was then confirmed by an *XMM-Newton* observation described by Stelzer & Schmitt (2004). The same low f/i-ratios for the O VII and Ne IX triplets were observed in *XMM-Newton* RGS spectra of the CTTS BP Tau (Schmitt et al. 2005), while the *XMM-Newton* EPIC spectra also clearly show the presence of rather hot plasma. The authors interpret the BP Tau data in terms of accretion with an additional active corona; similar conclusions were drawn by Robrade & Schmitt (2006) in a comparative study of the high and medium resolution X-ray data of four CTTS. The interpretation of the f/i-ratios in terms of density is not unambiguous. Ness & Schmitt (2005) presented a careful examination of density-sensitive iron lines in TW Hya and also showed that neither the UV flux nor line scattering affects the He-like triplets.

In this letter we present *Chandra* HETG spectra of the CTTS V4046 Sgr, which we show to closely resemble the X-ray spectra of TW Hya and BP Tau and to be the third star with very low

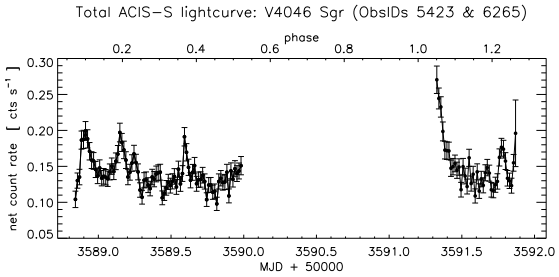

Fig. 1. X-ray lightcurve of V4046 Sgr, extracted from the 0th order data and dispersed spectra. The upper axis shows the orbital phase using the ephemerides from Stempels & Gahm (2004).

He-like f/i-ratios. We therefore suggest that accretion-related X-ray emission may in fact be quite common in CTTS.

2. V4046 Sgr: observations and data reduction

V4046 Sgr is a nearby CTTS at a distance between 42 pc (Hutchinson et al. 1990) and 83 pc (Quast et al. 2000). The star is isolated from any dark or molecular cloud and has negligible extinction. The CTTS nature of V4046 Sgr has been established through its variable Hα equivalent width (30–120 Å, Byrne 1986) and a strong infrared excess, IRAS-detected (de La Reza et al. 1986), while other IR observations are also consistent with a disk surrounding V4046 Sgr (Hutchinson et al. 1990). V4046 Sgr itself is a spectroscopic binary with a well-determined orbital period of 2.4213459 days (Stempels & Gahm 2004), consisting of a K7 V and a K5 V star with masses M_1 = 0.86 $M_\odot$ and M_2 = 0.69 $M_\odot$ at an orbital separation of less than 10 $R_\odot$ (Quast et al. 2000). The observed spectral energy IR distribution is consistent with an inner disk radius of 1.8 AU (Jensen & Mathieu 1997), the disk surrounding V4046 Sgr is thus circumbinary (Quast et al. 2000). The viewing angle of the system is i = 35–45°, and the symmetry axis of both the disk and the binary are supposed to coincide. The high-resolution optical spectroscopy of higher Balmer lines indicates gas clouds associated with the stars well within the inner radius of the circumbinary disk (Stempels & Gahm 2004).

V4046 Sgr was observed with the *Chandra* HETGS in two blocks, starting on 6 Aug. 2006 for 100 ks (ObsID 5423) and on 9 Aug. 2006 for 50 ks (ObsID 6265). First-order grating spectra were extracted by applying standard CIAO 3.3 tools, and then positive and negative orders were summed up. Individual emission lines in the HEG and MEG spectra were analysed with the CORA line-fitting tool (Ness & Wichmann 2002), assuming modified Lorentzian line profiles with β = 2.5.

3. Results

The X-ray lightcurve of V4046 Sgr is shown in Fig. 1. Several phases of enhanced flux levels are apparent, where the hardness of the X-ray radiation increases marginally; the second observation starts with what looks like the decay phase of a large flare. Variations in the shape of the higher Balmer line profiles are known to correlate with the orbital phase (Stempels & Gahm 2004), but we do not find any obvious correlation between X-ray flux and phase. We analysed single and combined spectra and found no significant differences between the two observations; therefore, we use the merged spectra in all of our analysis.

Table 1. Measured line fluxes for V4046 Sgr.

Line ID	λ (Å)	MEG (counts)	HEG (counts)	Photon flux[a]
Si XIV Lyα	6.18	32 ± 6	15 ± 4	2.5 ± 0.7
Si XIII r	6.64	46 ± 8	15 ± 4	2.7 ± 0.5
Si XIII i	6.69	10[b]	9 ± 3	1.5 ± 0.5
Si XIII f	6.74	36 ± 7	20 ± 5	2.9 ± 0.7
Mg XII Lyα	8.42	29 ± 6	n.a.	1.6 ± 0.4
Mg XI r	9.17	35 ± 7	n.a.	2.7 ± 0.5
Ne X Lyβ	10.23	57 ± 8	n.a.	5.2 ± 0.7
Ne X Lyα	12.14	280 ± 17	102 ± 10	48.7 ± 3.0
Ne IX r	13.46	245 ± 16	64 ± 8	74.2 ± 4.8
Ne IX i	13.56	107 ± 11	26 ± 5	32.0 ± 3.3
Ne IX f	13.70	105 ± 11	23 ± 5	33.2 ± 3.3
O VIII Lyβ	16.02	23 ± 5	n.a.	11.0 ± 2.0
O VIII Lyα	18.97	98 ± 10	n.a.	115.7 ± 11.8
O VII r	21.6	21 ± 5	n.a.	49.3 ± 11.7
O VII i	21.8	10.4 ± 3.5	n.a.	26.8 ± 9.0
O VII f	22.1	3.0 ± 2.2	n.a.	9.0 ± 7.0
N VII Lyα	24.78	28 ± 6	n.a.	75.0 ± 16.1
Fe XVII	15.01	38 ± 7	n.a.	17.0 ± 3.2
Fe XVII	15.26	21 ± 5	n.a.	8.1 ± 1.9
Fe XVII	17.05	21 ± 5	n.a.	14.0 ± 0.3
Fe XVII	17.10	22 ± 5	n.a.	14.6 ± 0.3

[a] In units of 10^{-6} photons cm^{-2} s^{-1} calculated from the MEG data except for the Si XIII triplet, where only an upper limit is available for the Si XIII i line; [b] 2σ upper limit.

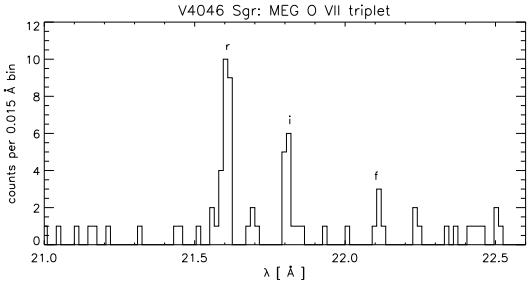

Fig. 2. The V4046 Sgr MEG count spectrum around the O VII triplet region.

The MEG and HEG grating spectra show a typical emission-line spectrum. Specifically, the Lyα lines of silicon, magnesium, neon, oxygen, and nitrogen and the Lyβ lines of neon and oxygen are detected (cf. Fig. 5). Weak iron lines are found from Fe XVII and Fe XVIII; He-like resonance lines are detected from oxygen, neon, and silicon, while the He-like Mg lines are very weak. The forbidden and intercombination lines of oxygen, neon, and silicon are clearly detected and resolved. The strongest detected lines, together with the derived best-fit line counts and their errors (as determined with CORA), are listed in Table 1.

In Fig. 2 we plot the observed MEG count spectrum in the O VII triplet region around 22 Å. Obviously, the signal is low, and yet the r and i lines are clearly detected with extremely high significance (cf. Table 1). However, only 3.0 ± 2.2 counts are recorded from the f line, clearly indicating deviations from the low-density limit. We specifically find f/i = 0.33 ± 0.28 for O VII, which must be compared to the low-density limit of 3.9 (Smith et al. 2001). Figure 3 shows the observed MEG count spectrum in the Ne IX triplet region around 13.5 Å. All triplet lines are clearly detected and, as shown by an inspection of the MEG spectrum, contamination by Fe XIX (cf. Ness et al. 2003) is of the

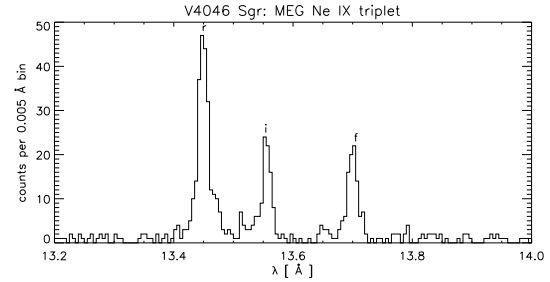

Fig. 3. The V4046 Sgr MEG count spectrum around the Ne IX triplet region.

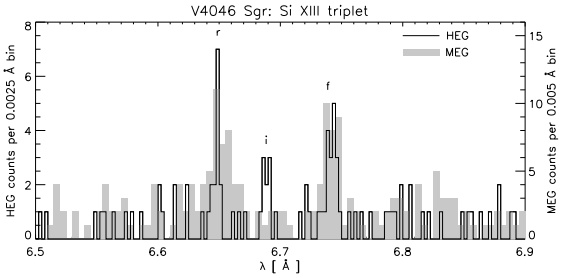

Fig. 4. Si XIII triplet region of V4046 Sgr in the HEG (black line) and MEG (shaded). The intercombination line is clearly stronger in the HEG than in the MEG, but the fits in Table 1 show that both measurements are statistically consistent.

order of a few percent at its worst for V4046 Sgr similar to the case of TW Hya (Stelzer & Schmitt 2004). The Ne IX f/i-ratio is 1.04 ± 0.15, derived under the assumption of negligible iron contamination, with the Ne IX low-density limit being 3.1. Finally, in Fig. 4 we plot the observed HEG and MEG count spectrum in the Si XIII triplet region around 6.7 Å.

All triplet lines are clearly detected in the HEG spectrum, the f line being approximately at the same strength as the r line. While only an upper limit for the i line can be obtained from the MEG spectrum, a Si XIII f/i-ratio of 1.9 ± 0.6 can be derived from the HEG spectrum, which compares well with the Si XIII f/i-ratios of the larger sample of active stars studied by Testa et al. (2004). Since the Si XIII f line is located exactly on the Si K edge of the detector, we investigated whether the observed Si XIII f/i-ratio (in recorded counts) is consistent with the Si XIII f/i-count ratio for a larger sample of stars. Assuming then that all active stars are in the low-density limit for Si XIII with $\log n_e < 13.5$, we conclude that the same applies for V4046 Sgr (as far as Si XIII is concerned). This conclusion is supported by the ratio of Fe XVII 17.10 Å / 17.05 Å of about unity, which Ness & Schmitt (2005) argue to be the low-density limit ($\log n_e < 13.6$); however, uncertain atomic physics require some caution.

4. Discussion

The X-ray data on the CTTS TW Hya and BP Tau have been interpreted in terms of an accretion funnel scenario, where the X-ray emission is emitted in a shock ("hot spot") produced by the infall of material along the magnetic field essentially at free-fall velocity onto the stellar surface. The main reason for this interpretation was the anomalously low O VII f/i-ratio observed for TW Hya and BP Tau, since the extensive spectral survey by Ness et al. (2004) found no star that would even come close to

Table 2. Comparison of properties of the three CTTS TW Hya, BP Tau, and V4046 Sgr.

	TW Hya	BP Tau	V4046 Sgr	
		f/i ratios		$\log n_e$
Si XIII	n.a	n.a.	1.9 ± 0.6	<13.5
Ne IX	0.33 ± 0.24	0.40 ± 0.26	1.05 ± 0.15	12.0
O VII	0.05 ± 0.05	0.37 ± 0.16	0.33 ± 0.28	11.5
		Ly α/r ratios		$\log T$ (K)
Si	1.83 ± 0.61	n.a.	1.13 ± 0.27	7.10 ± 0.05
Mg	0.60 ± 0.30	n.a.	1.03 ± 0.30	6.91 ± 0.05
Ne	0.63 ± 0.07	2.51 ± 0.85	0.70 ± 0.09	6.61 ± 0.01
O	2.02 ± 0.41	1.59 ± 0.35	2.36 ± 0.60	6.51 ± 0.05
		abundance ratios		solar
A_{Si}/A_{Mg}	1.63 ± 0.68	n.a.	1.58 ± 0.36	0.93
A_{Mg}/A_{Ne}	0.05 ± 0.02	n.a.	0.08 ± 0.02	0.32
A_{Ne}/A_{O}	0.86 ± 0.11	0.66 ± 0.20	1.04 ± 0.14	0.18

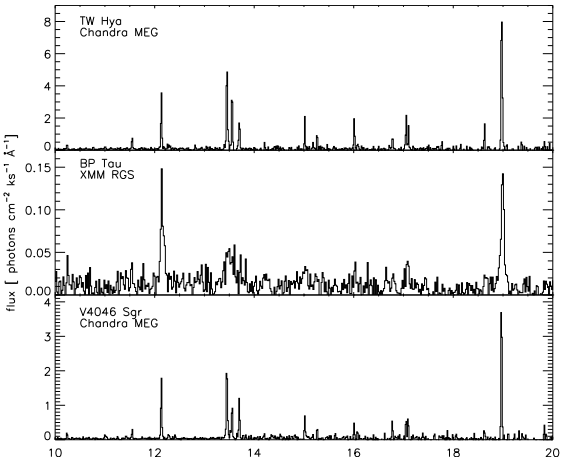

Fig. 5. Comparison of the X-ray flux spectra of TW Hya, BP Tau, and V4046 Sgr.

the low O VII f/i-ratio observed for those two stars. The question is therefore, wether the very same scenario also applies to the CTTS V4046 Sgr and possibly to CTTS as a class?

In Fig. 5 we compare the X-ray spectra in the range 10 Å to 20 Å for the three TW Hya (MEG), BP Tau (*XMM* RGS), and CTTS V4046 Sgr (MEG). Clearly, the energy resolution of the RGS instrument and the SNR of the BP Tau data set is lower than that of the MEG spectra. Nevertheless, some common trends, as well as differences, appear: In all three cases, the O VIII Ly α line is the strongest line, and neon lines are stronger than iron lines, which are weak if not absent. In BP Tau the Ne X Ly α line is much stronger than the Ne IX He-like r line, the opposite applies to TW Hya and V4046 Sgr. The different Ly α to He-like resonance line ratios for our three CTTS are summarised in Table 2. Interpreting these ratios in terms of an effective temperature, we note that the emission measure in V4046 Sgr cannot be described by a single temperature emission model. We also investigated the Ly α / Ly β ratios for Ne X and O VIII and compared the temperatures obtained in this way to estimates from the ratio of Ly α to He-like resonance line. The temperatures found in this way are both about 0.1 dex below the peak formation temperatures of their respective ionisation stages. We find that the ratios are fully consistent with optically thin emission, even if the absorption to

V4046 Sgr is as large as $N_{\rm H} = 10^{21}$ cm^{-2}. A second tracer of resonant scattering is the ratio Fe XVII 15.26 Å/15.01 Å, which matches optically thin predictions as well.

With regard to the He-like f/i-ratios for TW Hya, BP Tau, and V4046 Sgr (cf. Table 2), we find the observed O VII f/i-ratio of V4046 Sgr to compare well with what is observed for BP Tau and to be fully consistent with the lower value of TW Hya. When interpreted as a pure density diagnostics (i.e., assuming no contaminating UV flux), we find $\log n_{\rm e} \approx 11.5$ (Smith et al. 2001). Thus TW Hya, BP Tau, and V4046 Sgr are in marked contrast to the CTTS T Tau, where Güdel et al. (2006) measured an f/i ratio of ∼4 and inferred an upper limit to the electron density of 1.4×10^{10} cm^{-3} (68% confidence). Ne IX is formed at higher temperatures, and the Ne IX f/i-ratio of V4046 Sgr is somewhat higher than those measured for TW Hya and BP Tau, but still smaller than all the 48 Ne IX f/i-ratios determined by Ness et al. (2004) for their sample of active stars. The formal Ne IX density derived for V4046 Sgr is $\log n_{\rm e} \approx 12.0$. We stress that the f/i ratios for both Ne IX and O VII (peak formation temperatures $\log T \approx 6.6$ and $\log T \approx 6.3$, respectively) clearly deviate from the low-density limit; hence, the X-ray flux is unlikely to be produced in a stellar corona. On the contrary, the f/i-ratio measured for the Si XIII triplet agrees with the Si XIII f/i-ratios found in the survey by Testa et al. (2004); the Si XIII peak formation temperature of $\log T \approx 7.0$ cannot be reached in an accretion shock, so this triplet probably has a coronal origin.

Turning now to elemental abundances we use ratios of linear combinations of the measured fluxes of the H-like Lyα and He-like resonance lines to derive abundance ratios that are, as a first approximation, independent of the underlying temperature structure of the emitting plasma (Liefke & Schmitt 2006). In Table 2 we list the values of $A_{\rm Si}/A_{\rm Mg}$, $A_{\rm Mg}/A_{\rm Ne}$, and $A_{\rm Ne}/A_{\rm O}$ obtained for the three CTTS, as well as the solar value (Grevesse & Sauval 1998) for comparison. Drake et al. (2005) found the Ne/O abundance in BP Tau consistent with their sample of post-T Tauri stars, while Stelzer & Schmitt (2004) and Schmitt et al. (2005) interpret the – compared to solar – enhanced Ne/O abundances as due to grain depletion. Also, V4046 Sgr shows the same enhanced Ne/O abundances as found for TW Hya and BP Tau. As a consequence, the Mg/Ne abundance is low, both for V4046 Sgr and for TW Hya; however, the relative Si/Mg abundances are comparable to solar values.

5. Conclusions

For single CTTS, the model of an accreting hot spot, where material impacts onto the stellar surface at free-fall velocity, closely matches the observational data of both TW Hya (Kastner et al. 2002; Stelzer & Schmitt 2004) and BP Tau (Schmitt et al. 2005). Detailed simulations (Calvet & Gullbring 1998; Lamzin 1998; Günther et al. 2006) predict the emissivity, the line ratios, the UV field, and the veiling continuum. V4046 Sgr fits fully in this picture. Optically thin emission from an accretion hot spot explains the unusually low f/i-ratios observed in O VII and Ne IX. A "normal" corona accounts for the more energetic X-rays and, in particular, for the low-density Si XIII triplet, as well as for the variability of V4046 Sgr. This is somewhat surprising since the accretion geometry of V4046 Sgr is far more complicated because of its binary nature. Gas clouds close to the stars can be traced by line profile analysis of higher Balmer lines and seem to exist in the vicinity of the stars, yet no circumstellar disk should exist due to the small binary separation. The variability of the X-ray lightcurve suggests energetic events as observed for the case of BP Tau, as well as in the coronae of other stars; and we caution that densities of up to a few 10^{11} cm^{-3} (Güdel et al. 2002) seem to be occasionally reached in flares. As to abundances, V4046 Sgr shows the very high Ne/O abundance, reminiscent of TW Hya, and grain depletion is a suggestive scenario to explain the apparently high Ne abundance.

In summary, three of four CTTS with available high-resolution and high SNR X-ray grating spectra show far lower f/i ratios in the O VII and Ne IX triplets than any other star. In V4046 Sgr we are likely to see the emission from a corona in the high-temperature Si lines, and the binary nature of V4046 Sgr seems to have little influence on its X-ray spectrum. We thus conclude that the presence, not the absence, of low f/i ratios appears to be more typical of CTTS. Also, the emission mechanism obviously works in single and close binary stars, presenting a challenge for future magnetohydrodynamic simulations of the accretion funnel.

Acknowledgements. H.M.G., C.L., and J.R. acknowledge support from the DLR under grant 50OR0105. J.-U.N. gratefully acknowledges support provided by NASA through Chandra Postdoctoral Fellowship grant PF5-60039 awarded by the Chandra X-ray Center, which is operated by the Smithsonian Astrophysical Observatory for NASA under contract NAS8-03060.

References

Artymowicz, P., & Lubow, S. H. 1996, ApJ, 467, L77
Byrne, P. B. 1986, Ir. Astron. J., 17, 294
Calvet, N., & Gullbring, E. 1998, ApJ, 509, 802
de La Reza, R., Quast, G., Torres, C. A. O., et al. 1986, in New Insights in Astrophysics, Eight Years of UV Astronomy with IUE, ed. E. J. Rolfe, ESA SP-263, 107
Drake, J. J., Testa, P., & Hartmann, L. 2005, ApJ, 627, L149
Feigelson, E. 2005, in Star Formation in the Era of Three Great Observatories
Feigelson, E. D., & Montmerle, T. 1999, ARA&A, 37, 363
Flaccomio, E., Micela, G., & Sciortino, S. 2003, A&A, 402, 277
Grevesse, N., & Sauval, A. J. 1998, Space Sci. Rev., 85, 161
Güdel, M., Audard, M., Skinner, S. L., & Horvath, M. I. 2002, ApJ, 580, L73
Güdel, M., Skinner, S. L., Mel'nikov, S.-Y., et al. 2006, A&A, submitted
Günther, H. M., Schmitt, J. H. M. M., Robrade, J., & Liefke, C. 2006, A&A, submitted
Hutchinson, M. G., Evans, A., Winkler, H., & Spencer Jones, J. 1990, A&A, 234, 230
Jensen, E. L. N., & Mathieu, R. D. 1997, AJ, 114, 301
Kastner, J. H., Huenemoerder, D. P., Schulz, N. S., Canizares, C. R., & Weintraub, D. A. 2002, ApJ, 567, 434
Lamzin, S. A. 1998, Astron. Rep., 42, 322
Liefke, C., & Schmitt, J. H. M. M. 2006, A&A, accepted
Ness, J.-U., Brickhouse, N. S., Drake, J. J., & Huenemoerder, D. P. 2003, ApJ, 598, 1277
Ness, J.-U., Güdel, M., Schmitt, J. H. M. M., Audard, M., & Telleschi, A. 2004, A&A, 427, 667
Ness, J.-U., & Schmitt, J. H. M. M. 2005, A&A, 444, L41
Ness, J.-U., & Wichmann, R. 2002, Astron. Nachr., 323, 129
Quast, G. R., Torres, C. A. O., de La Reza, R., da Silva, L., & Mayor, M. 2000, in IAU Symp., 28P
Robrade, J., & Schmitt, J. H. M. M. 2006, A&A, 449, 737
Schmitt, J. H. M. M., & Liefke, C. 2004, A&A, 417, 651
Schmitt, J. H. M. M., Robrade, J., Ness, J.-U., Favata, F., & Stelzer, B. 2005, A&A, 432, L35
Shu, F., Najita, J., Ostriker, E., et al. 1994, ApJ, 429, 781
Smith, R. K., Brickhouse, N. S., Liedahl, D. A., & Raymond, J. C. 2001, ApJ, 556, L91
Stelzer, B., & Neuhäuser, R. 2001, A&A, 377, 538
Stelzer, B., Neuhäuser, R., & Hambaryan, V. 2000, A&A, 356, 949
Stelzer, B., & Schmitt, J. H. M. M. 2004, A&A, 418, 687
Stempels, H. C., & Gahm, G. F. 2004, A&A, 421, 1159
Testa, P., Drake, J. J., & Peres, G. 2004, ApJ, 617, 508

Chapter 4

X-ray emission from classical T Tauri stars: Accretion shocks and coronae?

H.M. Günther, J.H.M.M. Schmitt, J. Robrade and C. Liefke
Astronomy & Astrophysics, 466, 1111 (2007)
The original publication is available at www.aanda.org

A&A 466, 1111–1121 (2007)
DOI: 10.1051/0004-6361:20065669

Astronomy & Astrophysics

X-ray emission from classical T Tauri stars: accretion shocks and coronae?⋆

H. M. Günther, J. H. M. M. Schmitt, J. Robrade, and C. Liefke

Hamburger Sternwarte, Universität Hamburg, Gojenbergsweg 112, 21029 Hamburg, Germany
e-mail: moritz.guenther@hs.uni-hamburg.de

Received 23 May 2006 / Accepted 21 February 2007

ABSTRACT

Context. Classical T Tauri stars (CTTS) are surrounded by actively accreting disks. According to current models material falls along the magnetic field lines from the disk with more or less free-fall velocity onto the star, where the plasma heats up and generates X-rays.
Aims. We want to quantitatively explain the observed high energy emission and measure the infall parameters from the data. Absolute flux measurements allow to calculate the filling factor and the mass accretion rate.
Methods. We use a numerical model of the hot accretion spot and solve the conservation equations.
Results. A comparison to data from XMM-Newton and *Chandra* shows that our model reproduces the main features very well. It yields for TW Hya a filling factor of 0.3% and a mass accretion rate $2 \times 10^{-10}\ M_\odot\ \mathrm{yr}^{-1}$.

Key words. accretion, accretion disks – methods: numerical – stars: pre-main sequence – stars: late-type – stars: individual: TW Hya – X-rays: stars

1. Introduction

T Tauri stars are young (<10 Myr), low mass ($M_* < 3\ M_\odot$), pre-main sequence stars exhibiting strong Hα emission. The class of "Classical T Tauri stars" (CTTS) are surrounded by an accretion disk and are actively accreting material from the disk. The disks do not reach all the way to the stellar surface, rather they are truncated in the vicinity of the corotation radius. Infrared (IR) observations typically yield inner radii of 0.07–0.54 AU (Muzerolle et al. 2003), consistent with the corotation radius. Disk material is ionised by energetic stellar radiation and – somehow – loaded onto the stellar magnetic field lines, traditionally assumed to be dipole-like (but see Valenti & Johns-Krull 2004; Gregory et al. 2006). Along the magnetic field accretion funnels or curtains develop and matter impacts onto the star at nearly free-fall velocity (Uchida & Shibata 1984; Koenigl 1991). This process can remove angular momentum from the star (Shu et al. 1994). Observationally the accretion can be traced in the optical in the Hα line profile (Muzerolle et al. 2000), in the IR (Beristain et al. 2001) and in the UV (Herczeg et al. 2005). Further support for this scenario comes from the measurement of magnetic fields in some CTTS using the technique of spectropolarimetry and Zeeman-broadening (Johns-Krull et al. 1999, 2003; Symington et al. 2005). The kinetic energy of the accretion stream is released in one or several hot spots close to the stellar surface, producing the observed veiling continuum, and also line emission in the UV and X-rays. The emitted UV continuum radiation was previously calculated by Calvet & Gullbring (1998) and detailed models of the accretion geometry prove that stable states with two or more accretion spots on the surface can exist (Romanova et al. 2004). The UV emission has been also used to estimate mass accretion rates in CTTS with typical values of $10^{-8}\ M_\odot\ \mathrm{year}^{-1}$ (Gomez de Castro & Lamzin 1999; Johns-Krull et al. 2000).

T Tauri stars are copious emitters of X-ray emission. Specifically, X-ray emission from quite a few CTTS was detected with the *Einstein* (Feigelson & Decampli 1981; Feigelson & Kriss 1989) and *ROSAT* satellites (Feigelson et al. 1993; Neuhäuser et al. 1995; Gregorio-Hetem et al. 1998). The origin of the detected X-ray emission is usually interpreted as a scaled-up version of coronal activity as observed for our Sun, and the data and their interpretation prior to the satellites XMM-Newton and *Chandra* are summarised in a review by Feigelson & Montmerle (1999). However, recent observations of the CTTS TW Hya (Kastner et al. 2002; Stelzer & Schmitt 2004), BP Tau (Schmitt et al. 2005) and V4046 Sgr (Günther et al. 2006) with the grating spectrometers onboard XMM-Newton and *Chandra* indicate very high plasma densities in the X-ray emitting regions much higher than those observed in typical coronal sources. This finding suggests a different origin of at least the soft part of the X-ray spectrum in CTTS. Simple estimates show that X-rays can indeed be produced in the accretion spot of a typical CTTS (Lamzin 1998). We present here a more detailed accretion shock model, which predicts individual emission lines and can thus be directly confronted with observations to determine model parameters such as the maximum plasma temperature and mass accretion rate.

Unfortunately, only a few CTTS have so far been studied in detail using high-resolution X-ray spectroscopy with sufficient signal-to-noise ratio. It is therefore unknown at present whether the observed low forbidden to intercombination line ratios in He-like ions as measured for the CTTS TW Hya, BP Tau and V4046 Sgr are typical for CTTS as a class. Lower resolution studies of CTTS show significant differences between individual stars, possibly caused by considerable individual coronal activity, and in general it is difficult to disentangle coronal and

⋆ Based on observations obtained with XMM-Newton, an ESA science mission with instruments and contributions directly funded by ESA Member States and NASA.

accretion contributions (Robrade & Schmitt 2006) in the X-ray spectra of CTTS. Other suggested sources of X-rays include dense clumps in the stellar or disk wind of CTTS, heated up by shock waves. Simulations by Matt et al. (2002) show sufficiently dense regions in the stellar magnetosphere.

The goal of this paper is to consider the maximally possible accretion shock contribution, to determine the physical shock parameters, compute the emitted X-ray spectrum and assess to what extent other emission components are necessary to account for the observed X-ray spectra. The detailed plan of our paper is as follows: in Sect. 2 the observations used in this study are described briefly, in Sect. 3 we present our model and give the main assumption and limitations, in Sect. 4 the results of the simulation are shown and applied to observational data, followed by a short discussion of the main points in Sect. 5.

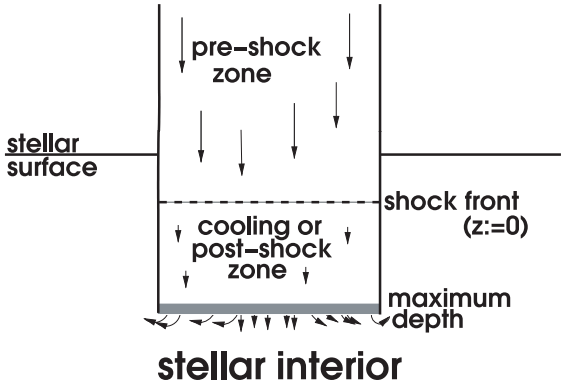

Fig. 1. Sketch illustrating the structure on the accretion column. In the stellar atmosphere a thin standing shock front forms followed by a radiative cooling zone.

2. Observations

2.1. Stellar parameters

With a distance of only 57 pc (Wichmann et al. 1998) TW Hya is the closest known CTTS; it is not submerged in a dark, molecular cloud like many other CTTS. Photometric observations show variability between magnitude 10.9 and 11.3 in the *V*-band (Rucinski & Krautter 1983). Broad Hα profiles (*FWHM* $\sim$ 200 km s^{-1}) were observed by Muzerolle et al. (2000), and TW Hya apparently belongs to a group of objects with similar age, the so-called TW Hydrae association (TWA; Webb et al. 1999). TW Hydrae's mass and radius are usually quoted as $M_* = 0.7\ M_\odot$, $R_* = 1.0\ R_\odot$, and its age as 10 Myr from Webb et al. (1999). Alternative values are given by Batalha et al. (2002), who place TW Hya on the HR diagram by Baraffe et al. (1998) and determine stellar parameters from the optical spectrum, which fits an older (30 Myr) and smaller star ($R_* = 0.8\ R_\odot$). The spectral type of TW Hya is K7 V-M1 V (Webb et al. 1999; Batalha et al. 2002) and the system is seen nearly pole-on (Kastner et al. 1997; Wilner et al. 2000; Alencar & Batalha 2002). Moreover, TW Hya displays variations in line profiles and veiling, which have been interpreted as signatures of accretion spot rotation (Alencar & Batalha 2002; Batalha et al. 2002). TW Hya has been observed in the UV with *IUE*, *FUSE* and *HST/STIS* (Herczeg et al. 2002), revealing a wealth of H_2 emission lines, consistent with the origin in the surface of a irradiated disk, and in X-rays with *ROSAT* by Costa et al. (2000), *Chandra*/HETGS (Kastner et al. 2002) and XMM-Newton/RGS (Stelzer & Schmitt 2004), where the grating data indictes a significant accretion shock contribution.

2.2. X-ray observations

We use high resolution spectra obtained with *Chandra* and XMM-Newton. TW Hya was observed for 48 ks with the *Chandra* HETGS on July 18, 2000 (Chandra ObsId 5). Kastner et al. (2002) report atypically high densities measured from the O VII and Ne IX triplets, and a very high neon abundance as observed for many active coronal sources in combination with a low iron abundance; the anomalously high neon abundance of TW Hya was investigated in more detail by Drake et al. (2005). A different approach to assess the plasma density of the emitting material by means of iron line ratios was performed by Ness & Schmitt (2005). First-order grating spectra were extracted applying standard CIAO 3.2 tools, positive and negative orders were added up. Individual emission lines in the HEG and MEG spectra were analysed with the CORA line fitting tool (Ness & Wichmann 2002), assuming modified Lorentzian line profiles with $\beta = 2.5$. A flare occurring in the second half of the observation was already mentioned by Kastner et al. (2002); for our global fitting approach we excluded the flaring period to avoid contamination due to the probable coronal origin of the flare.

Another X-ray spectrum was taken with XMM-Newton on July 9, 2001 with an exposure time of 30 ks (Obs-ID 0112880201) using the RGS as prime instrument. An analysis of this observation was presented in Stelzer & Schmitt (2004). We newly reduced also this dataset with the XMM-Newton Science Analysis System (SAS) software, version 6.0 and applied the standard selection criteria. The X-ray spectral analysis was carried out using XSPEC V11.3 (Arnaud 1996), and CORA for line-fitting. Because the line widths are dominated by instrumental broadening we keep them fixed at $\Delta\lambda = 0.06$ Å. The RGS spectra cover a larger wavelength range than HETGS spectra and include, in addition to the He-like triplets of Ne and O, also the N triplet. Both observations show the observed helium-like triplets to be incompatible with the low-density limit and an emission measure analysis indicates the presence of plasma with a few million degrees emitting in the soft X-ray region (Kastner et al. 2002; Stelzer & Schmitt 2004).

3. The model

In the currently accepted accretion paradigm the material follows the magnetic field lines from the disk down to the surface of the star. Here we only model the base of the accretion column, where the infalling material hits the stellar surface, is heated up in a shock and cools down radiatively. A sketch of the envisaged accretion scenario is shown in Fig. 1. Calculations of the excess continuum produced in this region were carried out by Calvet & Gullbring (1998). Lamzin (1998) already computed the emerging soft X-ray emission from such shocks, but due to bin sizes of 50 Å his results do not resolve individual lines, thus concealing much of the valuable diagnostic information. Nevertheless his models show that the hot spot produced by accretion can possibly produce not only the veiling, but also the soft X-ray emission. In our modelling we resolve all individual emission lines, allowing us to use line ratios as sensitive tracers of the density and temperature in the emitting region, and determine the elemental abundances of the emitting regions. Additionally we explicitly consider non-equilibrium ionisation states and distinguish ion and electron temperatures.

We assume a one-dimensional, plane parallel geometry for the accretion column. This is reasonable because the filling factor f, expressing the ratio between total spot size $A_{\rm spot}$ and stellar surface $A_* = 4\pi R_*^2$, is quite small as will be demonstrated a posteriori. The magnetic field is assumed to be perpendicular to the stellar surface and the material flows along the magnetic field lines. All turbulent fluxes are neglected and our model further assumes a stationary state. We use a two-fluid approximation attributing different temperatures to the atom/ion $T_{\rm ion}$ and to the electron components $T_{\rm e}$ of the plasma. However, both components move with the same bulk velocity v because they are strongly coupled by the microscopic electric fields. We ignore energy transport by heat conduction which is justified again a posteriori (see Sect. 3.4) and any radiative transport (see Sect. 3.5).

3.1. Calculation of shock front

Once the infalling material impacts onto the stellar surface, a shock forms, defining the origin of the depth coordinate z (see Fig. 1). The shock front itself is very thin, only of the order of a few mean free paths (Zel'Dovich & Raizer 1967), thus contributing only very marginally to the total emission. Therefore it is not necessary to numerically resolve its internal structure, rather it can be treated as a mathematical discontinuity and the total change in the hydrodynamic variables over this discontinuity is given by the Rankine-Hugoniot conditions (Zel'Dovich & Raizer 1967, Chap. 7, Sect. 15), which transform supersonic motion into subsonic motion in one single step. To simplify the numerical treatment we assume the direction of flow to be exactly parallel the magnetic field lines, so the Lorentz force does not influence the dynamics; we also expect the magnetic field to suppress heat conduction. Following the treatment by Calvet & Gullbring (1998) and Lamzin (1998) we assume the gas to expand into a vacuum behind the shock front. Because of larger viscous forces the strong shock formation occurs only in the ionic component, while the electron component is first only adiabatically compressed and subsequently heated through electron-ion collisions. In order to calculate the state of the ionic plasma behind the shock front in terms of the pre-shock conditions only the fluxes of the conserved quantities mass, momentum and energy are required. Marking the state in front of the shock front by the index 0, that behind the shock by index 1, the Rankine-Hugoniot conditions become

$$\rho_0 v_0 = \rho_1 v_1 \tag{1}$$

$$P_0 + \rho_0 v_0^2 = P_1 + \rho_1 v_1^2 \tag{2}$$

$$\frac{5P_0}{2\rho_0} + \frac{v_0^2}{2} = \frac{5P_1}{2\rho_1} + \frac{v_1^2}{2}, \tag{3}$$

where ρ denotes the total mass density of the gas and P its pressure.

Requiring that the electric coupling between ions and electrons leads an adiabatic compression of the electron component, implies a temperature rise for the electronic plasma component of

$$T_{e_1} = T_{e_0}\left(\frac{\rho_1}{\rho_0}\right)^{(\gamma-1)} \tag{4}$$

with $\gamma = 5/3$ denoting the adiabatic index. Because the time scale for heat transfer from ions to electrons is much larger than that of the ions passing through the shock front, ions and electrons leave the shock with vastly different temperatures. Numerical evaluation of the above equations behind the accretion shock front results in electron temperatures orders of magnitude lower than the ion temperature. Furthermore, the ions pass the shock front so fast that other degrees of freedom than kinetic are not excited and therefore kinetic and ionisation temperatures of the ions substantially differ.

3.2. Structure of the post-shock region

In the following section we compute how the originally different kinetic temperatures of ions and electrons as well as the ionisation temperature equilibrate and calculate the emitted X-ray spectrum.

3.2.1. Momentum balance

In the post-shock region heat is transferred from the ionic to the electronic component, at the same time the gas radiates and cools down, so the energy of the gas is no longer conserved. However, the particle number flux j of ions (and atoms)

$$j = nv \tag{5}$$

is conserved, where n is the ion/atom number density; the electron number density is denoted by $n_{\rm e}$. The total momentum flux j_p is conserved, since we ignore the momentum loss by radiation; it consists of the ion and the electron momentum as follows:

$$\begin{aligned} j_p &= \mu m_{\rm H} n v^2 + P_{\rm ion} + m_{\rm e} n_{\rm e} v^2 + P_{\rm e} \\ &= \mu m_{\rm H} n v^2 + nkT_{\rm ion} + m_{\rm e} n_{\rm e} v^2 + n_{\rm e} kT_{\rm e} \\ &\approx \mu m_{\rm H} n v^2 + nkT_{\rm ion} + n_{\rm e} kT_{\rm e} \; (m_{\rm e} \ll m_{\rm H}) \end{aligned} \tag{6}$$

with $P_{\rm ion}$ and $P_{\rm e}$ denoting the thermodynamic pressure of the ion and the electron gas respectively, $T_{\rm ion}$ and $T_{\rm e}$ their temperatures; $m_{\rm H}$ denotes the mass of a hydrogen atom, $m_{\rm e}$ the electron mass and μ is the dimensionless atomic weight.

3.2.2. Energy balance

Let us next consider the energy balance in the post-shock region. Both for the ions and the electrons the evolution of the energy per particle is described by an ordinary differential equation (ODE). Starting from the thermodynamic relation

$$T\mathrm{d}\Sigma - P\mathrm{d}V = \mathrm{d}U \tag{7}$$

where Σ denotes the entropy and U the internal energy of the plasma per heavy particle we will derive this ODE for the ionic component. In Eq. (7) the quantity $T\mathrm{d}\Sigma = \mathrm{d}Q$ denotes the heat flux through the boundaries of the system. The system "ions" looses heat by collisions with the colder electrons. Heat transfer is most efficient for the lighter ions and especially protons have a much larger collision cross sections than neutral hydrogen and they are by far the most abundant species in the plasma. To describe the heat transfer between ions and electrons we follow Zel'Dovich & Raizer (1967, Chap. VII, Sect. 10), who give the heat flow $\omega_{\rm ei}$ per unit volume per unit time as (in cgs-units)

$$\omega_{\rm ei} = \frac{3}{2} k n_{\rm H\,II} n_{\rm e} \frac{T_{\rm ion} - T_{\rm e}}{T_{\rm e}^{3/2}} \frac{\Lambda}{252} \; (T \text{ in K})$$

where k is Boltzmann's constant and Λ is the Coulomb-logarithm

$$\Lambda \approx 9.4 + 1.5 \ln T_{\rm e} - 0.5 \ln n_{\rm e}. \tag{8}$$

The number density of hydrogen ions is the number density of all heavy particles n multiplied by the abundance $\xi_{\rm H}$ of hydrogen and the hydrogen ionisation fraction $x^1_{\rm H}$:

$$\omega_{\rm ei} = \frac{3}{2} k \xi_{\rm H} x^1_{\rm H} n_{\rm e} \frac{T_{\rm ion} - T_{\rm e}}{T_{\rm e}^{3/2}} \frac{\Lambda}{252} \; (T \text{ in K}). \tag{9}$$

Transforming Eq. (7) written per heavy particle and taking the time derivative results in

$$\frac{{\rm d}U}{{\rm d}t} + P\frac{{\rm d}V}{{\rm d}t} = T\frac{{\rm d}\Sigma}{{\rm d}t} = \frac{{\rm d}Q}{{\rm d}t} = -\omega_{\rm ei}.$$

Using the stationarity condition $\frac{\rm d}{{\rm d}t} = \frac{\partial}{\partial t} + \frac{\partial z}{\partial t}\frac{\partial}{\partial z} = v\frac{\partial}{\partial z}$ transforms this into an ODE with the dependent variable z, measured from the shock front inwards (see Fig. 1); differentiation with respect to z will be indicated by $'$. Thus

$$vU' + PvV' = -\omega_{\rm ei}.$$

The internal energy U is in this case the thermal energy $U = \frac{3}{2}kT$, the pressure P can be rewritten using the equation of state for a perfect gas. The specific volume V is the inverse of the number density $V = \frac{1}{n}$. We thus obtain

$$v\left(\frac{3}{2}kT_{\rm ion}\right)' + vnkT_{\rm ion}\left(\frac{1}{n}\right)' = -\omega_{\rm ei}. \tag{10}$$

The derivation of a corresponding equation for the electron component is similar. Since the heat loss of the ion gas is a gain for the electrons this term enters with opposite sign, and an additional loss term $Q_{\rm col}$ appears representing energy losses by collisions which excite or ionise a heavy particle that in turn radiates.

It is convenient to write the electron number density as $n_{\rm e} = x_{\rm e} n$, with $x_{\rm e}$ denoting the number of electrons per heavy particle.

$$v\left(\frac{3}{2}x_{\rm e}kT_{\rm e}\right)' + vx_{\rm e}nkT_{\rm e}\left(\frac{1}{n}\right)' = \omega_{\rm ei} - Q_{\rm col}x_{\rm e}n, \tag{11}$$

because $\omega_{\rm ei}$ already includes the factor $x_{\rm e}n$ by definition in Eq. (9). Thus we are left with four independent variables (n, v, $T_{\rm ion}$ and $T_{\rm e}$); therefore, given $x_{\rm e}$, the system of the four hydrodynamic Eqs. (5), (6), (10) and (11) is closed and can be solved by numerical integration.

According to Spitzer (1965, Chap. 5.3) particle velocities reach a Maxwellian distribution after a few mean free path lengths. Evaluating the conditions behind the shock front we find that after a few hundred meters such distributions are established separately for both the ions and the electrons. We therefore assume that both ions and electrons each have their own individual Maxwellian velocity distributions throughout our simulation. This allows us to define an effective kinetic temperature for electron-atom/ion collisions. Usually collisions are treated using the ion rest frame as reference frame, and we fold the kinetic velocities of ion and electron and write the resulting Maxwellian distribution with the effective temperature $T_{\rm eff} = T_{\rm e} + T_{\rm ion}\frac{m_{\rm e}}{\mu m_{\rm H}}$. This effective collision temperature is then used to calculate the radiative loss term $Q_{\rm col}$ with the CHIANTI 4.2 code (Dere et al. 1997; Young et al. 2003). Because the gas may be in a non-equilibrium ionisation state the tables produced by the built-in CHIANTI rad_loss procedure, which assumes kinetic and ionisation temperatures equilibrated, are not valid in this case, instead a spectrum with the current state of ionisation and effective collision temperature is calculated and integrated over all contributing wavelengths to determine the instantaneous radiative losses. For fitting purposes it is further necessary to perform the simulations with different abundances because lower metallicity significantly lowers the cooling rate and therefore the extent of the post-shock cooling zone. In this approach it has to be assumed that $Q_{\rm col}$ is constant over each time step.

3.2.3. Microscopic physics

The calculation of the ionisation state is completely decoupled from the hydrodynamic equations given above. In each time step the density and the temperatures of both plasma components are fed from the hydrodynamic into the microscopic equations below. We assume changes in ionisation to occur only through collisions with electrons. Ions are ionised by electron collisions (bound-free) and recombine by electron capture (free-bound). So the number density of ionisations $r_{i\to i+1}$ per unit time from state i to $i+1$ is proportional to the number density of ions n_i in ionisation state i and the number density of electrons $n_{\rm e}$; for convenience we leave out a superscript identifying the element in question here:

$$r_{i\to i+1} = R_{i\to i+1} n_{\rm e} n_i. \tag{12}$$

Recombination is the reverse process:

$$r_{i\to i-1} = R_{i\to i-1} n_{\rm e} n_i. \tag{13}$$

The quantity $R_{i\to j}$ is the rate coefficient describing ionisation for $j = i+1$ and recombination for $j = i-1$. For element z $R_{1\to 0} = R_{z+1\to z+2} \equiv 0$ because 1 represents the neutral atom, which cannot recombine any further, and $z+1$ the completely ionised ion which cannot lose any more electrons. The cross section σ for each process depends not only on the ion, but also on the relative velocity of ion and electron. On the one hand, the number of ions in state i decreases by ionisation to state $i+1$ or recombination to state $i-1$, on the other hand, it increases by ionisations from $i-1$ to i and by recombination from $i+1$. For an element with atomic number Z there is thus a set of $Z+1$ equations

$$\frac{{\rm d}n_i}{{\rm d}t} = n_{\rm e}(R_{i-1\to i}\, n_{i-1} - (R_{i\to i+1} + R_{i\to i-1})\, n_i + R_{i+1\to i}\, n_{i+1}). \tag{14}$$

Through the electron number density $n_{\rm e}$ the equations for all elements are coupled and together with the condition of number conservation they provide a complete system of differential equations. This system can be simplified considerably under the assumption that $n_{\rm e}$ is constant during each time step Δt. Because hydrogen and helium, the main donors of electrons, are completely ionised $n_{\rm e}$ is mainly given by the hydrodynamics. This assumption leads to one independent set of equations per element. Dividing by the number density of the element in question and using that the number density n^A_Z of ions in ionisation stage Z for element A is $n^A_Z = n\xi^A x^A_Z$ with abundance ξ^A of element A and the ionisation fraction x^A_Z, finally leads to

$$\frac{{\rm d}x_i}{{\rm d}t} = n_{\rm e}(R_{i-1\to i}\, x_{i-1} - (R_{i\to i+1} + R_{i\to i-1})\, x_i + R_{i+1\to i}\, x_{i+1}). \tag{15}$$

The rate coefficients $R_{i\to j}$ are taken from Mazzotta et al. (1998) for dielectronic recombination, for the radiative recombination and the ionisation (collisional and auto-ionisation) rate we use a code from D.A. Verner, which is available in electronic form on the web[1]. We calculate only the elements with $Z = 1$–28, considering all ionisation states for each of them. The model is implemented in IDL (Interactive data language) and the ODEs are independently integrated using "lsode", an adaptive stepsize algorithm, which is provided in the IDL distribution.

[1] http://www.pa.uky.edu/~verner/fortran.html

3.3. Verification

In order to check our computational procedures we considered several special cases with known analytical solutions. This includes a pure hydrogen gas with different electron and ion temperatures to test the heat transfer treatment and the ionisation of hydrogen at constant temperature. We compare our calculations for the collisional ionisation equilibrium to Mazzotta et al. (1998), who use the same data sources as we do without the corrections from Verner & Iakovlev (1990). Cl is the element where the largest differences occur, for all important elements all differences are marginal at best. In addition to these physical tests we examined which spatial resolution is possible. We use an adaptive step size sampling regions with steep gradients sufficiently densely so that none of our physical variables changes by more than 5%. In order to keep the computation time at a reasonable level, we also enforced a minimum step size of 1 m.

3.4. Heat conduction

Thermal conduction tends to smooth out temperature gradients. It is not included in our simulation and we use the models' temperature gradients to estimate its importance. According to Spitzer (1965, Chap. 5.5) the thermal heat flux $F_{\rm cond}$ is

$$F_{\rm cond} = \kappa_0 T^{5/2} \frac{{\rm d}T}{{\rm d}z}. \tag{16}$$

Here $\kappa_0 = 2 \times 10^{-5} \Lambda^{-1}$ erg K$^{7/2}$ s^{-1} cm^{-1} is the coefficient of thermal conductivity. Comparing the thermal heat flux according to this equation to the energy flux carried by the bulk motion, it never exceeds more than a few percent of the bulk motion energy transport in the main part of the cooling zone except for the lowest density cases. Small scale chaotic magnetic fields in the plasma are possible; they would be frozen in and expected to further suppress thermal conduction.

3.5. Optical depth effects

Our simulation assumes all lines to be optical thin. The continuum opacity in the soft X-ray region is small, however, we need to check line opacities. The optical depth $\tau(\lambda)$ for a given line can be expressed as

$$\tau(\lambda) = \int \kappa(\lambda) {\rm d}l, \tag{17}$$

where l measures distance along the photon path and $\kappa(\lambda)$ is the local absorption coefficient, which can be computed from the oscillator strength f of the line in question, the number density $n_{\rm low}$ of ions in the lower state and the line profile function $\Phi(\lambda)$:

$$\kappa(\lambda, z) = \frac{\pi e^2}{m_{\rm e} c} f n_{\rm low}(z) \Phi(\lambda, z), \tag{18}$$

with e being the electron charge and c the speed of light. We approximate the line profile to follow a Gaussian distribution law with the normalisation $\int_0^\infty \Phi(\lambda, z) {\rm d}\lambda = 1$ at all z, centred at λ_0 with the width $\Delta\lambda_{\rm b}(z)$:

$$\Phi(\lambda, z) = \frac{1}{\sqrt{\pi}} \frac{\lambda_0(z)^2}{c \Delta\lambda_{\rm b}(z)} \exp\left(- \left(\frac{\lambda - \lambda_0(z)}{\Delta\lambda_{\rm b}(z)} \right)^2 \right); \tag{19}$$

$\lambda_0(z)$ is the wavelength at line centre. Because the shocked gas is moving into the star, but decelerating, it is Doppler-shifted with the bulk velocity $v(z)$ at depth z according to $\lambda_0(z) = \lambda_{\rm rest}\,(1 + v(z)/c)$, where $\lambda_{\rm rest}$ is the rest wavelength. The broadening $\Delta\lambda_{\rm b}(z)$ is in the case of purely thermal broadening

$$\Delta\lambda_{\rm b}(z) = \frac{\lambda_0(z)}{c} \sqrt{\frac{2kT(z)}{m_{\rm ion}}}, \tag{20}$$

but turbulent broadening $\Delta\lambda_{\rm t}(z)$ may additionally contribute. This cannot be calculated from the 1D-hydrodynamics in our approach, it can only be included in an ad hoc fashion. On the one hand, at the boundaries of the accretion shock region typical turbulent flows might reach velocities comparable to the bulk motion and thus significantly broaden the observed lines, on the other hand, the magnetic fields presumed to be present should tend to suppress flows perpendicular to the field lines. For the calculation of the optical depth we chose $\Delta\lambda_{\rm t}(z) = 10$ km s^{-1}. If the turbulent broadening is larger, the line profiles get wider and the optical depth decreases. All lines considered in this study are excited from the ground state. Since in collisionally-dominated plasmas almost all excited ion states decay relatively fast, we assume that all ions are in their ground state. $n_{\rm low}$ is then the product of the ionisation fraction for the line producing ion, the abundance of that element and the total ion number density. It is important to consider that the line centre depends on depth because of the Doppler shift due to the bulk velocity. Photons emitted at line centre in deeper regions end up in the wings of the profile in higher layers. Since our simulation does not include radiative transfer all lines have to be checked for optical depth effects. The exact geometry and position of the accretion shock is still unkown, but of substantial importance for estimates the line optical depth. The radiation could either escape through the boundaries of the post-shock funnel perpendicular to the direction of flow or through the shock and the pre-shock region. If the spatial extent of any single accretion funnel is small and it is located high up in the stellar atmosphere, the optical depth in the first scenario is small and the accretion contribution to the total stellar emission is large. We select this scenario in the further discussion. If, however, the shock is buried deep in the stellar atmosphere, the radiation can only escape through the shock and the thin pre-shock gas. In this case, denpending in the infall conditions, the optical depth of resonance lines can be large compared to unity.

3.6. Limitations by 1D

Since our model is 1D, all emitted photons can travel only up or down, they cannot leave the accretion region sideways. To a first approximation half of the photons is emitted in either direction. The downward emitted photons will eventually be absorbed by the surrounding stellar atmosphere which will be heated by this radiation. The influence of the surrounding atmosphere on the shock region is expected to be small, since the temperature and hence the energy flux from the surrounding atmosphere into the shock region is much lower. We expect the shock structure to be well represented in 1D, but the size of the hot spots could be underpredicted because, depending on the geometrical extend of each spot, less than half of the emission escapes.

3.7. Boundary conditions and limitations of the model

All our simulations start with a pre-shock temperature of 20 000 K and and the corresponding (stationary) equilibrium ionisation state (Arnaud & Rothenflug 1985). This choice of temperature is motivated by studies of the photoionisation in the accretion stream by the post-shock emission

(Calvet & Gullbring 1998) and analytical considerations about the electron heat flux (Zel'Dovich & Raizer 1967). While we ignore heat conduction in the post-shock region, across the shock front the temperature gradient is of course large. The electrons have then mean free path lengths much larger than the shock front extent will therefore heat up the inflowing gas. We tested the influence of different initial conditions and found that the post-shock zone depends only marginally on the chosen initial ionisation state. We terminate our simulations when the temperature drops below 12 000 K. Here the opacity begins to play an important role and the energy flux from the central core of the star is no longer negligible compared to the accretion flux. Here and just behind the shock front the accuracy is affected because the step size reaches its lower limit and rapid ionisation or recombination processes are not resolved. So the model is expected to be more accurate for ions which exist at high temperatures e.g. in the formation region of O VII or O VIII, which are precisely those observed at X-ray wavelengths.

3.8. Model grids

The free fall velocity onto a star with mass M_* and radius R_* is

$$v_{\rm free} = \sqrt{\frac{2GM_*}{R_*}} = 617 \sqrt{\frac{M_*}{M_\odot}} \sqrt{\frac{R_\odot}{R_*}} \frac{\rm km}{\rm s}. \quad (21)$$

Typically CTTS have masses comparable to the Sun and radii between $R_* = 1.5\ R_\odot$ and $R_* = 4\ R_\odot$ (Muzerolle et al. 2003), because they have not yet finished their main sequence contraction. Most CTTS have inner disk radii of 10–90 solar radii (Muzerolle et al. 2003), for the specific case of TW Hya Eisner et al. (2006) find an inner disk radius of $\approx 12\ R_\odot$, thus the actual infall speed can almost reach the free-fall speed. Previous analyses indicate particle number densities of the infalling gas of about 10^{12} cm^{-3}. We therefore calculated a grid of models with infall velocities v_0 varying between 200 km s^{-1} and 600 km s^{-1} in steps of 25 km s^{-1}, and infall densities n_0 varying between 10^{10} cm^{-3} and 10^{14} cm^{-3} with 13 points equally spaced on a logarithmic density scale. For each model in the grid we then calculate the emissivity for selected lines in the X-ray region using the version 5.1 of CHIANTI (Dere et al. 1997; Landi et al. 2006). We start out with abundances from Grevesse & Sauval (1998) and iterate the model fits until convergence (see Sect. 4.3.3).

4. Results

4.1. Structure of the post-shock region

Figure 2 shows typical model temperature and density profiles. In the (infinitesimally thin) shock, defined at depth 0 km, the ion temperature suddenly rises and cools down directly behind the shock front because the ion gas transfers energy to the electrons. After a few kilometers both ions and electrons have almost identical temperatures and henceforth there is essentially only radiative heat loss. This region we refer to as the post-shock cooling zone, where most of the X-ray emission originates (see Fig. 1). During radiative cooling the density rises and because of momentum conservation the gas slows down at the same time (Eq. (6)). As more and more energy is lost from the system, the density and the energy loss rate increase and the plasma cools down very rapidly in the end. In the example shown in Fig. 2, the shock reaches a depth of about 950 km, which is much smaller than a stellar radius, thus justifying our simplifying assumption of a planar geometry a posteriori.

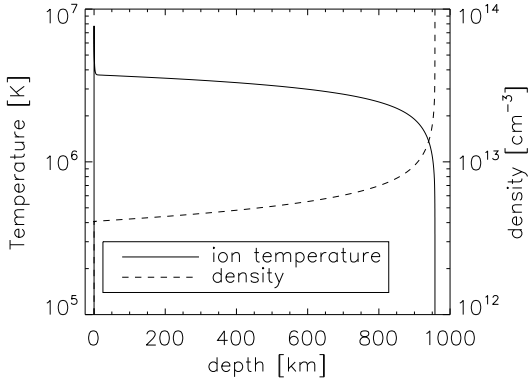

Fig. 2. Temperature and density profiles for a shock calculated with $n_0 = 10^{12}$ cm^{-3} and $v_0 = 525$ km s^{-1}, chemical abundances as found in TW Hya (Sect. 4.3.3).

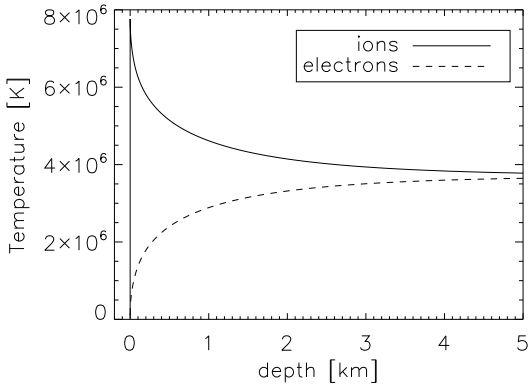

Fig. 3. Ion and electron temperatures in the upper post-shock region for a shock calculated with the same starting conditions as in Fig. 2.

The region where the electron and ion temperature substantially differ from each other is much smaller than this maximum depth, thus a two-fluid treatment is not strictly necessary for most parts of the shock. In Fig. 3 both temperatures are plotted in comparison. At the shock front the electrons stay relatively cool because they are only compressed adiabatically. Behind the shock front the energy flows from the ions to the electrons, and already at a depth of 5 km ions and electrons have almost identical temperatures. In Fig. 4 we show the depth dependence of the ionisation state of neon, which produces strong lines observed by *Chandra* and XMM-Newton. On passing through the shock front neon is nearly instantaneously ionised up to Ne IX, in the following ≈50 km the mean ionisation rises until the equilibrium is reached. The plasma then contains a few percent Ne XI nuclei, about 40% of the is in the form of Ne X, the rest comes as Ne IX. Further away from the shock the ions recombine because of the general cooling of the plasma, following the local equilibrium closely, so the fraction of Ne VII rises. At the maximum depth the ions quickly recombine to lower ionisation states.

The maximal temperatures are proportional to v_0^2 as can be seen analytically from the equation of state for a perfect gas:

$$T_1 \sim \frac{P_1}{n_1} \sim \frac{n_0 v_0^2}{n_1} \sim v_1 u_0 \sim v_0^2. \quad (22)$$

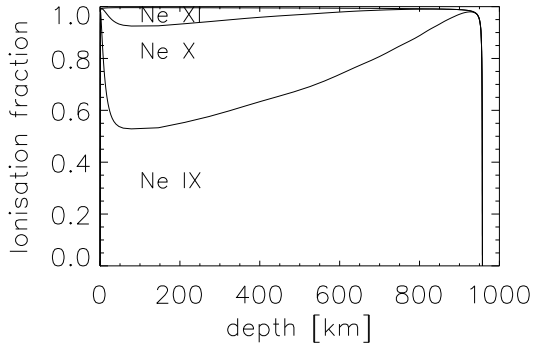

Fig. 4. Ionisation state of neon for a shock calculated with the same starting conditions as in Fig. 2. See text for a detailed description.

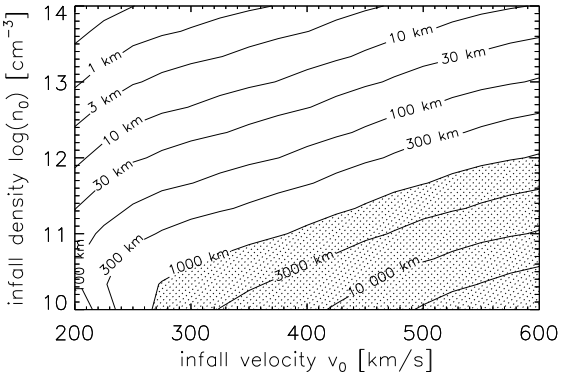

Fig. 5. The length of the cooling zone dependent on the logarithm of the infall density $\log n_0$ and the infall velocity v_0 (abundances from Grevesse & Sauval 1998): the length of the cooling region is labelled. The dotted area marks regions where the deeper parts of the simulated shock are below the cut-off.

These estimates are obtained using Eqs. (1)–(3) and neglecting the initial pressure.

A higher infall velocity leads to a deeper post-shock cooling zone since the material reaches higher temperatures and consequently needs longer to cool down, so it flows for longer times and penetrates into deeper regions. Secondly, lower infall densities result in shocks with a larger spatial extent. Since the energy losses roughly scale with the square of the density, a lower density will increase the cooling time of the gas to cool down to photospheric temperatures. Figure 5 shows that cooling zone lengths between 1 km and 10 000 km can be reached depending on the chosen model parameters. Our model assumes a free plasma flow during cooling without any direct influence from the surrounding stellar atmosphere. As long as the infalling gas has a sufficiently large ram pressure, the model assumption should be applicable, since the surrounding atmosphere is pushed away and mixes with the accreted material only after cooling. For thin gases the ram pressure is lower and the gas needs more time for cooling down. Therefore in the deeper and denser layers the approximation of a freely flowing gas is no longer valid and the whole set of model assumptions breaks down. The depth, where this happens, depends on the stellar parameters. The shock front forms where its ram pressure

$$p_{\rm ram} = \rho v_0^2, \qquad (23)$$

roughly equals the gas pressure of the stellar atmosphere. The pressure of the stellar atmosphere rises exponentially with depth, so, independent of the starting point, only shocks with small cooling length can be described by the hydrodynamic modelling used here. We place a cut-off at $z = 1000$ km, where the pressure of the surrounding atmosphere will be larger by about an order of magnitude already.

4.2. Optical depth

We find that in all reasonable cases the total column density over the whole simulated region is small, in the best-fit solution it turns out to $N_{\rm H} = 10^{21}$ cm^{-2}, so the continuum opacity is small as assumed. Because emission originates at all depths the mean absorption column is even less. The line opacity along the direction of flow reaches values considerably above unity, so if the radiation passes through the whole post-shock region and does not escape through the boundaries the emssion in the resonance lines is considerably reduced (e.g. in Fig. 9). However, as we show in the following, the observed line ratios can be consistently explained in the accretion shock model, so the assumption of a geometry allowing most photons to escape, seems to be realistic.

4.3. Application to TW Hya

In order to model the actual X-ray data available for TW Hya we applied a two-step process: First we used only the line fluxes of selected strong lines detected in the X-ray spectra and determined the best-fit shock model in an attempt to assess the maximally possible shock contribution. Then, in a second step, we performed a global, simultaneous fit to all available – lower resolution – data allowing for possible additional coronal contributions.

4.3.1. Fit to line fluxes

Ratios between emission lines of the same element allow a determination of the best model parameters independent of the elemental abundances. Specifically, the XMM-Newton data contain the helium-like triplets of N,O and Ne, which strongly emit at plasma temperatures of a few MK (see Table 1). For these three elements the corresponding Lyα lines are also measured, while we do not use any of the Lyβ lines because they provide relatively little additional temperature sensitivity and are substantially weaker than the Lyα lines. For each model we therefore compute three line ratios for each of the elements N, O and Ne, i.e., the so-called R- and G-ratios defined from the He-like triplets (Gabriel & Jordan 1969; Porquet et al. 2001) through $R = f/i$ and $G = (f + i)/r$ respectively as well as the ratio of the Lyα to the He-like r-lines. These nine line ratios are compared to the data via the χ^2- statistics; the resulting contour plot of χ^2 as a function of the model parameters n_0 and v_0 is shown in Fig. 7. Correcting for the absorption does not alter the results since $N_{\rm H}$ is small ($N_{\rm H} = 3.5 \times 10^{20}$ cm^{-2}; Robrade & Schmitt 2006). The best model is found for the parameters $v_0 = 525$ km s^{-1} and $n_0 = 10^{12}$ cm^{-3} with an unreduced $\chi^2 = 31.9$ (7 degrees of freedom). One has to be careful here in interpreting the absolute value of the χ^2 because it is derived from very few highly significant numbers with non-Gaussian errors.

The strong neon lines confine the fit most effectively because their values have the smallest statistical uncertainties. The density is mainly restricted by R-ratios, the velocity by the

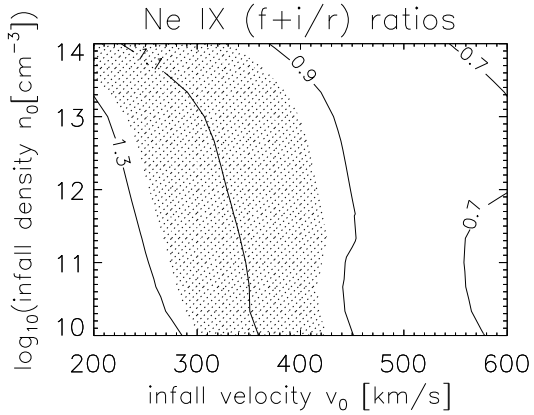

Fig. 6. Contour are labelled with calculates Ne G-ratios. The observed value for TW Hya is shaded in grey (1σ-error).

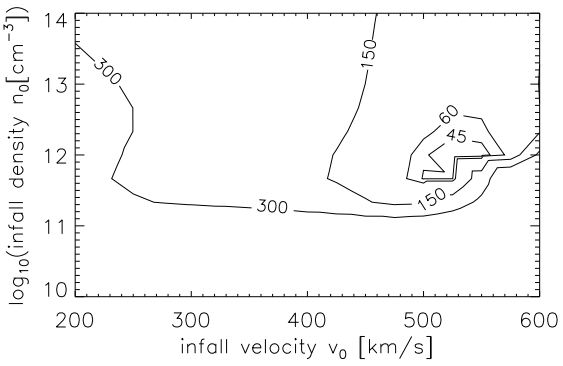

Fig. 7. Contours are labelled with unreduced χ^2 values for TW Hya (7 d.o.f.), data from XMM-Newton.

Lyα/r-ratios, which are temperature-sensitive. The Ne G-ratio deviates from the best fit parameters significantly (see Fig. 6). Its observed value is 1.1 ± 0.13, which points to infall velocities between 300 km s^{-1} and 400 km s^{-1}; fitting only the remaining eight ratios we obtain the same best fit model as before. The fit does not depend on the chosen background radiation temperature in the range 6000 K to 10 000 K.

The available *Chandra* data include a somewhat different wavelength interval. Only the triplets from O and Ne are covered, but the *Chandra* MEG has better spectral resolution, allowing to reliably measure several iron lines. We use the three lines of Fe XVII at 16.78 Å, 17.05 Å and 17.09 Å, and calculate the ratio of the two doublet members and the total doublet to the third line (see Table 1). The best fit model for this data set has v_0 = 575 km s^{-1}, slightly higher than found for the XMM-Newton data, and $n_0 = 10^{12}$ cm^{-3}, with an unreduced value χ^2 of 8.3 for 6 degrees of freedom. Again there is no difference between 6000 K and 10 000 K taken as temperature for a black-body radiation background. The neon G-ratio points again to lower infall velocities. Both fits have a tight lower bound on the density $n_0 = 10^{12}$ cm^{-3} of the infalling gas. We estimate the error as one grid point, i.e., ±25 km s^{-1} for v_0 and ±0.33 for log (n_0). The free-fall velocity for TW Hya is between 500 km s^{-1} to 550 km s^{-1}, setting a tight upper bound and we adopt v_0 = 525 km s^{-1} as the best value. We thus conclude that the same shock model is capable of explaining the line ratios observed in both the XMM-Newton RGS and *Chandra* HETGS grating spectra of TW Hya.

4.3.2. Global fit

In our second step we implement the shock emission as XSPEC table model and proceed with a normal XSPEC analysis of the medium and high resolution XMM-Newton spectra. The analysis of both the *Chandra* and XMM-Newton data (Kastner et al. 2002; Stelzer & Schmitt 2004) suggested the presence of higher temperature plasma possibly from an active corona; the flare observed in the *Chandra* observation may be a signature of activity.

To account for these additional contributions we add up to three thermal VAPEC models and include interstellar extinction. These additional thermal components are calculated in the low density limit and are meant to represent a coronal contribution. The elemental abundances for all components are coupled. It would be interesting to check if the accreting plasma is grain depleted compared to the corona, but the data quality is not sufficient to leave more abundances as free fit parameters. Because of the parameter degeneracy between the emission measure of the cool component and the interstellar absorption column $N_{\rm H}$, we kept the latter fixed at $N_{\rm H} = 3.5{\times}10^{20}$ cm^{-2}, a value suggested by Robrade & Schmitt (2006, where a detailed discussion is given). The fit uses the data from one of the *XMM* EPIC MOS detectors, RGS1 and RGS2 and *Chandra's* HEG and MEG simultaneously in the energy range from 0.2 keV to 10 keV. The normalisation between the instruments is left independent to allow for calibration uncertainties and possible brightness variations between the observations. Because of the much larger count rates the lower resolution MOS detectors tend to dominate the χ^2 statistic. To balance this we include all available grating information, but only one (MOS1) low resolution spectrum in the global fit.

The fit results for our different models are presented in Table 2. Model A represents the best fitting pure accretion shock, while models B-C include additional temperature components; the main improvement is obviously brought about by the introduction of a high temperature ($kT \approx 1.30$ keV) component, representing the emission from a hot corona. "Normal" coronae usually have emission measure distributions that can be described by a two-temperature model (Briggs & Pye 2003) and this motivates us to add cool low-density plasma component in model C. Although the reduced χ^2 is only marginally smaller, we regard this as a better model, because it can be naturally interpreted in terms of a stellar corona. A third low-density component does clearly not improve the fit any further (model D). In Fig. 8 we show the recorded EPIC MOS1 low resolution spectrum, our best-fit model and separately the accretion and coronal contributions. An inspection of Fig. 8 shows that at energies below ≈1.2 keV the overall emission is dominated by the shock emission, while at higher energies the coronal contribution dominates because of the thermal cut-off of the shock emission. A distinction between high and low density plasma is possible only by examining the line ratios in the He-like triples or in iron lines. In broad band spectra cool coronal and shock plasma exhibit the same signatures. The ratio of their emission measures was therefore taken from the RGS modelling alone (model C and D). Our global fit reproduces the triplet ratios quite satisfactorily as shown in Fig. 9 for neon and in Fig. 10 for the oxygen triplet.

The resulting infall velocity for model C is 530^{+8}_{-4} km s^{-1} and the density $n_0 = (1 \times 10^{12} \pm 3 \times 10^{11})$ cm^{-3} (errors are statistical only). In this scenario the total flux is dominated by the accretion shock (3.7×10^{-12} ergs cm^{-2} s^{-1}) which is about four

Table 1. The line ratios used in the fitting process for both observations are shown with their errors. The two rightmost columns show results for the best-fit scenario from the simulation with $n_0 = 10^{12}$ cm^{-3} for both models.

Line ratio	XMM/RGS	Chandra/HETGS	v_0 = 525 km s^{-1}	v_0 = 575 km s^{-1}
N R-ratio	0.33 ± 0.24	n. a.	0.00	0.00
N G-ratio	0.88 ± 0.31	n. a.	0.77	0.75
N Lyα/N VI r	4.04 ± 1.00	n. a.	2.40	2.82
O R-ratio	0.06 ± 0.05	0.04 ± 0.06	0.02	0.02
O G-ratio	0.51 ± 0.07	0.82 ± 0.22	0.73	0.71
O Lyα/O VII r	2.01 ± 0.18	2.19 ± 0.43	1.49	1.97
Ne R-ratio	0.50 ± 0.07	0.54 ± 0.08	0.32	0.31
Ne G-ratio	1.10 ± 0.10	0.94 ± 0.09	0.80	0.75
Ne Lyα/Ne IX r	0.27 ± 0.04	0.62 ± 0.06	0.26	0.49
Fe XVII (17.09Å+17.05Å)/16.78Å	n. a.	3.32 ± 0.88	2.25	2.22
Fe XVII 17.09Å/17.05Å	n. a.	0.58 ± 0.16	0.81	0.79
red. χ^2	4.6	1.4		

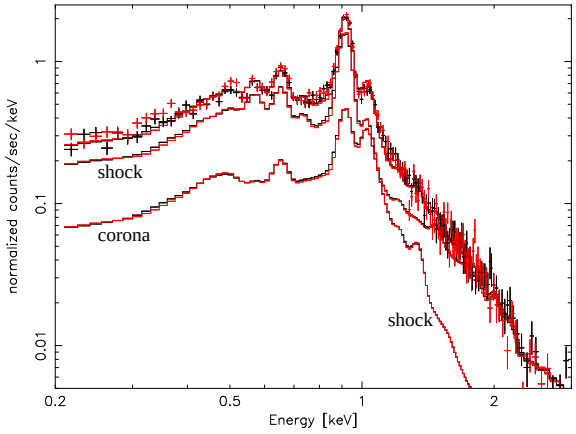

Fig. 8. Data for the MOS1 (black symbols) and the MOS2 (red/grey symbols) together with our best fit model C and its components.

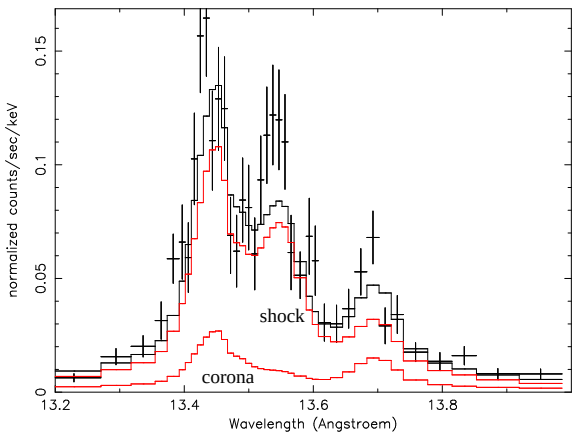

Fig. 9. Ne triplet: Data from RGS2 with model C (black) and accretion (red/grey upper line) and coronal component (red/grey lower line).

times stronger than the cool corona (1.0×10^{-12} erg cm^{-2} s^{-1}) and five times stronger than the hot corona (0.8×10^{-12} erg cm^{-2} s^{-1}) in the 0.3–2.5 keV band.

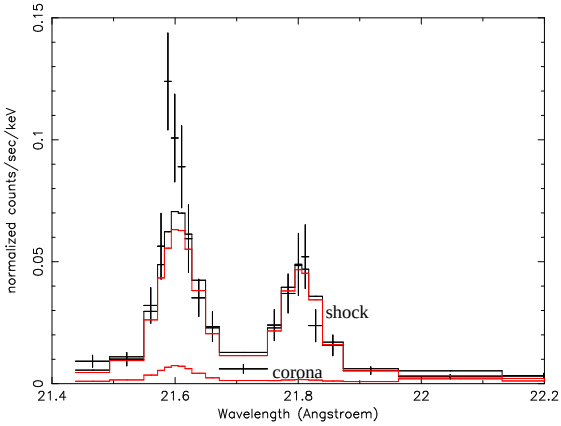

Fig. 10. O triplet: Data from RGS1 with model C (black) and accretion (red/grey upper line) and coronal component (red/grey lower line).

Table 2. Reduced χ^2 values for models with zero to three VAPEC components with temperature kT_1 to kT_3 in [keV] and one shock component. The absorption column is given in units of $[10^{20}\frac{1}{\mathrm{cm}^2}]$. The shock model converges to $v_0 \approx 530$ km s^{-1} and $n_0 \approx 10^{12}$ cm^{-3} in all cases except A (v_0 pegs at the free-fall velocity of ≈575 km s^{-1}).

Model	kT_1	kT_2	kT_3	N_H	red. χ^2 (d.o.f.)
A	–	–	–	=3.5	2.8 (584)
B	–	–	1.33	=3.5	1.63 (580)
C	0.27	–	1.35	=3.5	1.57 (577)
D	0.27	0.72	1.26	=3.5	1.56 (573)

4.3.3. Elemental abundances

The abundance fitting has to be performed recursively until the abundances converges, because different abundances lead to different cooling functions and thus change the whole shock structure. Specifically, we start from the set of elemental abundances determined by Robrade & Schmitt (2006) and iterate. Our global fit procedure yields abundance values (Table 3) relative to solar abundances from Grevesse & Sauval (1998), the errors given are purely statistical (1σ range), while we believe the systematic error to be about 15%. As a cross-check we compare the intensities of lines from different elements in our pure shock model from Sect. 4.3.1 and find that the abundance ratios estimated in this way roughly agree. The final abundance estimates (Table 3)

Table 3. Abundance of elements relative to Grevesse & Sauval (1998) and first ionisation potentials (FIP). The errors are statistical only, we estimate the systematic error to 15%.

Element	abundance	FIP [eV]
C	$0.20^{+0.03}_{-0.03}$	11.3
N	$0.51^{+0.05}_{-0.04}$	14.6
O	$0.25^{+0.01}_{-0.01}$	13.6
Ne	$2.46^{+0.06}_{-0.04}$	21.6
Mg	$0.37^{+0.10}_{-0.06}$	7.6
Si	$0.17^{+0.07}_{-0.07}$	8.1
S	0.02^{a}	10.4
Fe	$0.19^{+0.01}_{-0.01}$	7.9

[a] Formal 2σ limit.

show a metal depleted plasma with the exception of neon, which is enhanced by about a factor of ten compared to the other elements and nitrogen, which is enhanced by a factor of two. Metal depletion has also been observed in the wind of TW Hya by Lamzin et al. (2004) and was noted by Argiroffi et al. (2005) using X-ray observations of the non-accreting quadruple system TWA 5 in the vicinity of TW Hya. Stelzer & Schmitt (2004) interpret the abundances as a sign of grain depletion, where the grain forming elements condensate and mainly those elements are accreted, which stay in the gas phase like the noble gas neon. This is discussed in more detail by Drake et al. (2005), who collect evidence that metal depletion can be also seen in the infrared and the UV, where the spectral distribution indicates well advanced coagulation into larger orbiting bodies, which may resist the inward motion of the accreted gas. On the other hand, stars with active corona often show an enhancement of elements with a high first ionisation potential (IFIP), which also leads to an enhanced neon abundance (Brinkman et al. 2001).

4.3.4. Filling factor and mass accretion rate

A comparison of the observed energy flux $f_{\rm obs}$ (at the distance d to the star) and the simulated flux $f_{\rm sim}$ per unit area allows to calculate the accretion spot size $A_{\rm spot}$ through

$$A_{\rm spot} = \frac{f_{\rm obs}(d)}{f_{\rm sim}(R_*)} 4\pi d^2. \tag{24}$$

The filling factor f is the fraction of the stellar surface covered by the spot:

$$f = \frac{A_{\rm spot}}{4\pi R_*^2} = \frac{f_{\rm obs}(d)}{f_{\rm sim}(R_*)} \frac{d^2}{R_*^2} \tag{25}$$

and the mass accretion rate is the product of the spot size and the mass flux per unit area, which in turn is the product of the gas density $\rho_0 = \mu m_{\rm H} n_0$ and the infall velocity v_0:

$$\frac{{\rm d}M}{{\rm d}t} = A_{\rm spot}\rho v_0 = A_{\rm spot}\mu m_{\rm H} n_0 v_0 \ . \tag{26}$$

We assume that half of the emission is directed outward and can be observed, the other half is directed inwards, where it is absorbed. For model C the spot size is 1×10^{20} cm^2, yielding filling factors of 0.15% and 0.3% for $R_* = 1\ R_\odot$ and $R_* = 0.8\ R_\odot$ respectively and accretion rates of about $2 \times 10^{-10}\ M_\odot$ yr^{-1}.

4.4. Shock position in the stellar atmosphere

We now compare the ram pressure of the infalling gas to the stellar atmospheric pressures as calculated from `PHOENIX`; we specifically use a density profile from AMES-cond-v2.6 with effective temperature $T_{\rm eff} = 4000$ K, surface gravity $\log g = 4.0$ and solar metalicity (Brott & Hauschildt 2005 based on Allard et al. 2001). The chosen stellar parameters resemble those of typical CTTS. The shock front is expected to form, where the ram pressure approximately equals the stellar atmospheric pressure, which increases exponentially inwards. In a strict 1D-geometry photons emitted upwards out of the cooling zone will be absorbed by an infinite accretion column, but in a more realistic geometry they can pass either through the stellar atmosphere or the pre-shock gas as can be seen in Fig. 1. We estimate a lower limit for the hydrogen column density of $N_{\rm H} = 10^{20}$ cm^{-2}, the actually measured column density is 3.5×10^{20} cm^{-2} (Robrade & Schmitt 2006) by adding the column density between shock front and emitting ion to the the column density of the pre-shock gas, which the photons penetrate before escaping from the accretion funnel outside the stellar atmosphere. The optical depth of the stellar atmosphere is far higher than our lower limit for the pre-shock gas. This estimate proves that shocks, as described by our model, are actually visible; for a contrary view on this subject matter see Drake (2005).

5. Discussion

The best fit parameters of our shock model to match the X-ray observations of TW Hya are obtained by using a shock with the parameters $v_0 \approx 525$ km s^{-1} and $\log n_0 \approx 12$. Previously infall velocities closer to ∼300 km s^{-1} were reported by a number of authors (Lamzin 1998; Calvet & Gullbring 1998). Other observational evidence also suggests lower values; in the UV emission is found in highly ionised emission lines (C IV, N V and O VI) extending up to ≈400 km s^{-1} and in cool ions in absorption (Fe II) against a hot continuum likely emerging from an accretion spot (Lamzin et al. 2004). Since the gas strongly accelerates close to the stellar surface, the density will be lower in the high velocity region because of particle number conservation, so, depending on the geometry of the accretion funnel, the emission measure in this region may well be very small. In this case the observed lines will have weak wings extending to larger velocities, which are difficult to identify observationally. We therefore regard these observations only as a lower bound; an upper bound is provided by the free-fall velocity of ∼500–550 km s^{-1}.

Measurements of TW Hya in different wavelength regions lead to conspicuously distinct mass accretion rates. Generally, the published estimates far exceed the results of our simulation, which gives an accretion rate of $\approx(2 \pm 0.5) \times 10^{-10}\ M_\odot$ yr^{-1} and filling factors of 0.2%–0.4%. Alencar & Batalha (2002) and Batalha et al. (2002) use optical spectroscopy and photometry and state a mass accretion rate between 10^{-9} and $10^{-8}\ M_\odot$ yr^{-1} and a filling factor of a few percent. In the UV the picture is inconsistent. On the one hand, two empirical relations for line intensities as accretion tracers (Johns-Krull et al. 2000) indicate mass accretion rates above $3 \times 10^{-8}\ M_\odot$ yr^{-1} (data from Valenti et al. 2000, evaluated by Kastner et al. 2002), on the other hand fitting blackbodies on the UV-veiling by Muzerolle et al. (2000) suggests a significantly lower value: $4 \times 10^{-10}\ M_\odot$ yr^{-1}. A similar procedure has been earlier applied by Costa et al. (2000) with a much larger filling factor. The previous X-ray analyses by Kastner et al. (2002, $\dot{M} = 10^{-8}\ M_\odot$ yr^{-1}) and Stelzer & Schmitt (2004, $\dot{M} = 10^{-11}\ M_\odot$ yr^{-1}) suffer from the problem that they use filling factors extracted from UV-measurements (from Costa et al. 2000 and Muzerolle et al. 2000 respectively) and a post-shock density calculated from X-ray observations which does not necessarily represent the same region. Our simulation now

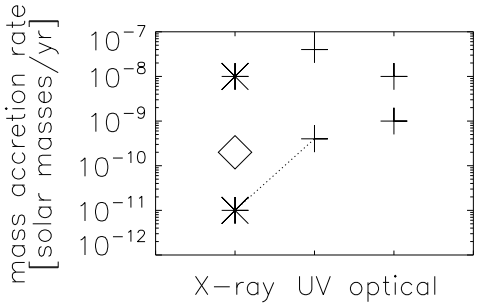

Fig. 11. Estimated mass accretion rates sorted by the energy of the observation. +: optical and UV measurements; *: X-ray, for the data from Stelzer & Schmitt (2004) the dotted line connects to the UV measurement, which delivers the filling factor, ⋄: this simulation; data sources: see text.

is the first attempt to rely solely on the X-ray measurements. The different values for mass accretion rates are summarised in Fig. 11.

A physical explanation for these differences goes as follows: At longer wavelengths one observes plasma at cooler temperatures and in general the filling factor and mass accretion rates are higher, because the spot is inhomogeneous with different infall velocities. Fast particles would be responsible for a shock region with high temperatures which is observed in X-rays, whereas in other spectral bands cooler areas can be detected, and therefore the total area and the observed total mass flux is larger. Accretion spots with these properties are predicted by the magneto-hydrodynamic simulations recently performed by Romanova et al. (2004) and Gregory et al. (2006). Very probably some of the difference can be attributed to intrinsically changing accretion rates. Simulations of the inner flow region often show highly unstable configurations (von Rekowski & Brandenburg 2006).

We showed that basic properties of the X-ray spectra from CTTS can be naturally explained by accretion on a hot spot, but this is not the only X-ray emission mechanism. To understand especially the high energy tail we had to introduce two thermal components which fit a corona as it is expected in late-type stars and suggested by observations of activity; in the case of TW Hya the shock can dominate the overall X-ray emission. Forthcoming high-resolution observations will hopefully allow to extend the sample of CTTS, where a similar analysis is feasible.

Acknowledgements. CHIANTI is a collaborative project involving the NRL (USA), RAL (UK), MSSL (UK), the Universities of Florence (Italy) and Cambridge (UK), and George Mason University (USA).
H.M.G., J.R and C.L. acknowledge support from DLR under 50OR0105.

References

Alencar, S. H. P., & Batalha, C. 2002, ApJ, 571, 378
Allard, F., Hauschildt, P. H., Alexander, D. R., Tamanai, A., & Schweitzer, A. 2001, ApJ, 556, 357
Argiroffi, C., Maggio, A., Peres, G., Stelzer, B., & Neuhäuser, R. 2005, A&A, 439, 1149
Arnaud, K. A. 1996, in Astronomical Data Analysis Software and Systems V, ASP Conf. Ser., 101, 17
Arnaud, M., & Rothenflug, R. 1985, A&AS, 60, 425
Baraffe, I., Chabrier, G., Allard, F., & Hauschildt, P. H. 1998, A&A, 337, 403
Batalha, C., Batalha, N. M., Alencar, S. H. P., Lopes, D. F., & Duarte, E. S. 2002, ApJ, 580, 343
Beristain, G., Edwards, S., & Kwan, J. 2001, ApJ, 551, 1037
Briggs, K. R., & Pye, J. P. 2003, MNRAS, 345, 714
Brinkman, A. C., Behar, E., Güdel, M., et al. 2001, A&A, 365, L324
Brott, I., & Hauschildt, P. H. 2005, in ESA SP-576: The Three-Dimensional Universe with Gaia, 565
Calvet, N., & Gullbring, E. 1998, ApJ, 509, 802
Costa, V. M., Lago, M. T. V. T., Norci, L., & Meurs, E. J. A. 2000, A&A, 354, 621
Dere, K. P., Landi, E., Mason, H. E., Monsignori Fossi, B. C., & Young, P. R. 1997, A&AS, 125, 149
Drake, J. J. 2005, in 13th Cambidge Workshop on Cool Stars, Stellar Systems and the Sun, 519
Drake, J. J., Testa, P., & Hartmann, L. 2005, ApJ, 627, L149
Eisner, J. A., Chiang, E. I., & Hillenbrand, L. A. 2006, ApJ, 637, L133
Feigelson, E. D., & Decampli, W. M. 1981, ApJ, 243, L89
Feigelson, E. D., & Kriss, G. A. 1989, ApJ, 338, 262
Feigelson, E. D., & Montmerle, T. 1999, ARA&A, 37, 363
Feigelson, E. D., Casanova, S., Montmerle, T., & Guibert, J. 1993, ApJ, 416, 623
Gabriel, A. H., & Jordan, C. 1969, MNRAS, 145, 241
Gomez de Castro, A. I., & Lamzin, S. A. 1999, MNRAS, 304, L41
Gregorio-Hetem, J., Montmerle, T., Casanova, S., & Feigelson, E. D. 1998, A&A, 331, 193
Gregory, S. G., Jardine, M., Simpson, I., & Donati, J.-F. 2006, MNRAS, 371, 999
Grevesse, N., & Sauval, A. J. 1998, Space Sci. Rev., 85, 161
Günther, H. M., Liefke, C., Schmitt, J. H. M. M., Robrade, J., & Ness, J.-U. 2006, A&A, 459, L29
Herczeg, G. J., Linsky, J. L., Valenti, J. A., Johns-Krull, C. M., & Wood, B. E. 2002, ApJ, 572, 310
Herczeg, G. J., Walter, F. M., Linsky, J. L., et al. 2005, AJ, 129, 2777
Johns-Krull, C. M., Valenti, J. A., & Koresko, C. 1999, ApJ, 516, 900
Johns-Krull, C. M., Valenti, J. A., & Linsky, J. L. 2000, ApJ, 539, 815
Johns-Krull, C. M., Valenti, J. A., & Gafford, A. D. 2003, in Rev. Mex. Astron. Astrofis. Conf. Ser., 38
Kastner, J. H., Zuckerman, B., Weintraub, D. A., & Forveille, T. 1997, Science, 277, 67
Kastner, J. H., Huenemoerder, D. P., Schulz, N. S., Canizares, C. R., & Weintraub, D. A. 2002, ApJ, 567, 434
Koenigl, A. 1991, ApJ, 370, L39
Lamzin, S. A. 1998, Astron. Rep., 42, 322
Lamzin, S. A., Kravtsova, A. S., Romanova, M. M., & Batalha, C. 2004, Astron. Lett., 30, 413
Landi, E., Del Zanna, G., Young, P. R., et al. 2006, ApJS, 162, 261
Matt, S., Goodson, A. P., Winglee, R. M., & Böhm, K.-H. 2002, ApJ, 574, 232
Mazzotta, P., Mazzitelli, G., Colafrancesco, S., & Vittorio, N. 1998, A&AS, 133, 403
Muzerolle, J., Calvet, N., Briceño, C., Hartmann, L., & Hillenbrand, L. 2000, ApJ, 535, L47
Muzerolle, J., Calvet, N., Hartmann, L., & D'Alessio, P. 2003, ApJ, 597, L149
Ness, J.-U., & Schmitt, J. H. M. M. 2005, A&A, 444, L41
Ness, J.-U., & Wichmann, R. 2002, Astron. Nachr., 323, 129
Neuhäuser, R., Sterzik, M. F., Schmitt, J. H. M. M., Wichmann, R., & Krautter, J. 1995, A&A, 297, 391
Porquet, D., Mewe, R., Dubau, J., Raassen, A. J. J., & Kaastra, J. S. 2001, A&A, 376, 1113
Robrade, J., & Schmitt, J. H. M. M. 2006, A&A, 449, 737
Romanova, M. M., Ustyugova, G. V., Koldoba, A. V., & Lovelace, R. V. E. 2004, ApJ, 610, 920
Rucinski, S. M., & Krautter, J. 1983, A&A, 121, 217
Schmitt, J. H. M. M., Robrade, J., Ness, J.-U., Favata, F., & Stelzer, B. 2005, A&A, 432, L35
Shu, F., Najita, J., Ostriker, E., et al. 1994, ApJ, 429, 781
Spitzer, L. 1965, Physics of fully ionized gases, Interscience Tracts on Physics and Astronomy (New York: Interscience Publication), 2nd Rev. Ed.
Stelzer, B., & Schmitt, J. H. M. M. 2004, A&A, 418, 687
Symington, N. H., Harries, T. J., Kurosawa, R., & Naylor, T. 2005, MNRAS, 358, 977
Uchida, Y., & Shibata, K. 1984, PASJ, 36, 105
Valenti, J. A., & Johns-Krull, C. M. 2004, Ap&SS, 292, 619
Valenti, J. A., Johns-Krull, C. M., & Linsky, J. L. 2000, ApJS, 129, 399
Verner, D. A., & Iakovlev, D. G. 1990, Ap&SS, 165, 27
von Rekowski, B., & Brandenburg, A. 2006, Astron. Nach., 327, 53
Webb, R. A., Zuckerman, B., Platais, I., et al. 1999, ApJ, 512, L63
Wichmann, R., Bastian, U., Krautter, J., Jankovics, I., & Rucinski, S. M. 1998, MNRAS, 301, L39
Wilner, D. J., Ho, P. T. P., Kastner, J. H., & Rodríguez, L. F. 2000, ApJ, 534, L101
Young, P. R., Del Zanna, G., Landi, E., et al. 2003, ApJS, 144, 135
Zel'Dovich, Y. B., & Raizer, Y. P. 1967, Physics of shock waves and high-temperature hydrodynamic phenomena, ed. W. D. Hayes, R. F. Probstein (New York: Academic Press)

Chapter 5

Modelling the X-rays of classical T Tauri stars: The binary CTTS V4046 Sgr

H. M. Günther and J. H. M. M. Schmitt
Memorie della Societa Astronomica Italiana, 78, 359 (2007)

Mem. S.A.It. Vol. , 1

Memorie della

Modelling the X-rays of classical T Tauri stars

The binary CTTS V4046 Sgr

H. M. Günther and J. H. M. M. Schmitt

Hamburg Sternwarte, Gojenbergsweg 112, 21029 Hamburg
e-mail: moritz.guenther@hs.uni-hamburg.de

Abstract. Three classical T Tauri stars (CTTS) have so far been observed with high S/N and high resolution X-ray spectroscopy yet: TW Hya, BP Tau and V4046 Sgr. Their spectra indicate high densities and it is still a matter of some debate if they are exceptional objects or representatives of their class. V4046 Sgr is a close binary consisting of two K stars with typical signatures of CTTS. It has been observed with Chandra/HETGS for 150 ks. The helium-like triplets of Si, Ne and O are clearly detected. Using a 1-dim, stationary, non-equilibrium model of the post-shock accretion zone, the emission observed can be decomposed in accretion and coronal components. The accretion with its comparatively high densities explains unusual f/i ratios in the triplets, the coronal component explains the high energy emission at temperatures, which cannot be reached in an accretion shock.

Key words. Accretion – Methods: numerical – Stars: pre-main sequence – Stars: individual: TW Hya, V4046 Sgr – Stars: late-type – X-rays: Stars

1. Introduction

Classical T Tauri stars (CTTS) are low-mass pre-main sequence objects still actively accreting from a surrounding disk. It has been known for a long time that they are X-ray emitters (see review by Feigelson & Montmerle 1999), but only observations with high resolution gratings revealed through He-like triplet diagnostics that the emitting plasma shows unusually high densities, which cannot be interpreted as a scaled-up version of the solar corona (Kastner et al. 2002; Stelzer & Schmitt 2004; Schmitt et al. 2005; Günther et al. 2006). We follow the idea of Koenigl (1991), that the accretion proceeds along magnetically funnelled streams and the X-ray emission is produced in an accretion shock at the footpoints of the funnel, where the material impacts on the stellar surface with free-fall velocity.
In this paper we model the accretion component, add a low-density coronal component and fit the *Chandra* observations in order to obtain accretion flow parameters.

2. The model

The model is described in detail in Günther et al. (submitted to A&A), following the ideas of Shu et al. (1994). A shock develops, where the ram pressure equals the thermodynamic pressure of the surrounding stellar atmosphere (see Fig. 1). The shock is treated as a mathematical discontinuity, where the ion gas is heated according to the Rankine-Hugoniot conditions, it sets the origin

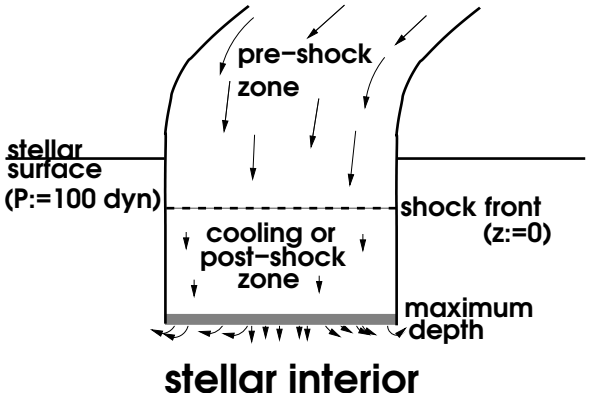

Fig. 1. A sketch of the accretion shock geometry.

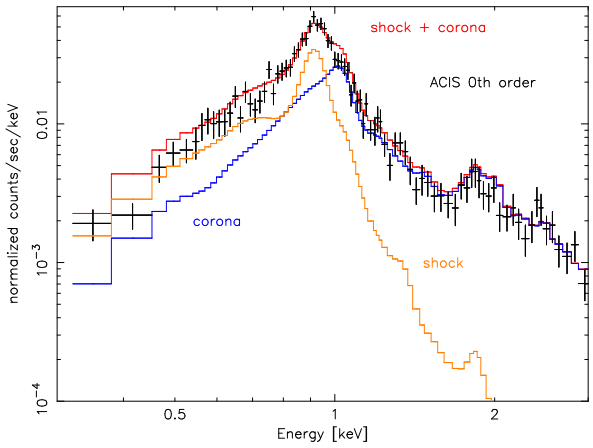

Fig. 2. CCD spectrum of V4046 Sgr with best-fit model (red/grey). The model components are the shock (orange/light grey) and the the low-density corona (blue/black).

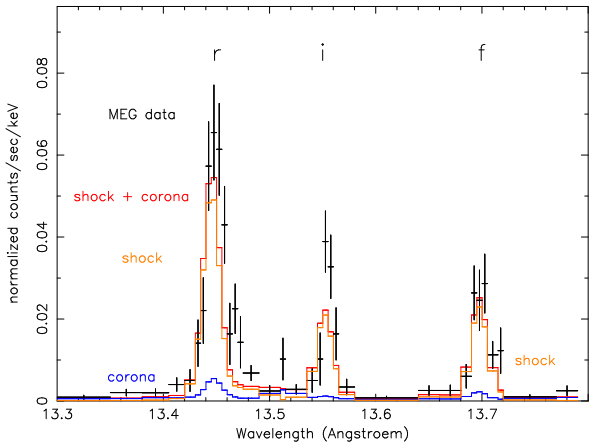

Fig. 3. Ne IX triplet in V4046 Sgr, see Fig. 2. Only the high density accretion shock component contributes to the intercombination line.

of the z coordinate. In the post shock cooling zone we stepwise integrate the hydrodynamic and the ionisation equations in a two fluid approximation of electrons and ions under the following assumptions: No heat conduction through the boundaries or inside the cooling flow, no viscosity, both components have their own Maxwell distribution, stationarity of the problem, all gas is optically thin and the magnetic field $\boldsymbol{B}||\boldsymbol{v}$, so it does not influence the flow. We futher assume that hydrodynamics and atomic physics can be treated separately during each step. This leads to an ordinary differential equation for the ion temperature $T_{\rm ion}$ in depth z:

$$v\frac{\mathrm{d}}{\mathrm{d}z}\left(\frac{3}{2}kT_{\rm ion}\right) + vnkT_{\rm ion}\frac{\mathrm{d}}{\mathrm{d}z}\left(\frac{1}{n}\right) = -\omega_{ei} \qquad (1)$$

for the ions with number density n and bulk velocity v, where k is the Boltzmann constant. ω_{ei} describes the heat flow from the ions to the colder electrons according to Coulomb interactions. A similar relation is obtained for the electrons, containing additional terms for radiative losses. We vary the model parameters infall velocity v_0, infall density n_0 and the abundances of C, N, O, Ne, Mg, Si, S and Fe. We then use XSPEC to fit out shock and two low-density APEC components, representing the corona, with coupled abundances simultaneously to the data.

3. Results

The observation and data reduction is described in detail in Günther et al. (2006). Our best-fit results are shown in Fig. 2. The accretion shock dominates in the soft part of the spectrum and its flux rapidly falls off above 1 keV, because the infall velocity sets an upper limit on the energy per particle. The more energetic part is dominated by the corona. Fig. 3 shows the He-like Ne IX triplet. In purely coronal sources the forbidden line is stronger than the intercombination line. Here the high density plasma in the accretion shock emits in the i line, resulting in a f/i ratio close to 1. This density-sensitive ratio constrains the infall density, the temperature the infall velocity. From the normalisation of the shock emission the total emitting area and therefore the

Table 1. Best fit parameters for the CTTS TW Hya and V4046 Sgr

Parameter	TW Hya	V4046 Sgr
v_0 [km s^{-1}]	525	535
n_0 [cm^{-3}]	10^{12}	2×10^{11}
filing factor	2×10^{-3}	1×10^{-3}
$\dot{M}$ [M$_\odot$/yr]	2×10^{-10}	3×10^{-11}
χ^2 (dof)	1.57 (577)	1.23 (1113)[a]
obs. flux (energy band 0.3-2.5 keV) in erg/cm^2/s		
shock	3.7×10^{-12}	1.2×10^{-12}
corona	2.0×10^{-12}	1.2×10^{-12}

[a]: Churazov weighting necessary because of the small number of counts per bin

filling factor, defined as the ratio of spot area to stellar surface, can be estimated. We assume a distance of 83 pc (Quast et al. 2000). The resulting numbers are given in table 1 and compared to results for TW Hya from Günther et al. (submitted to A&A). V4046 Sgr is a system of two CTTS, a K7 and a K5 dwarf. As it is not resolved in our observation and the parameters of both stars are similar, we treat it in the same way as a single star. The resulting mass accretion rate is possibly split between both objects.

In general the mass accretion rates obtained by our method are surprisingly low. This is likely due to geometrical effects. In our simple 1D approach half of emission is generated upwards, but in reality photons crossing from the comparatively thin plasma in the accretion funnel into the stellar atmosphere get absorbed. This lowers the total intensity observed (see Fig. 1) and leads to an underestimation of filling factor and mass accretion rate. Because the local geometry of the accretion funnel and the size of individual spots are uncertain, it is very difficult to estimate the importance of this effect. Furthermore, recent simulations indicate that the accretion spots may be inhomogeneous with a distribution of infall velocities (Romanova et al. 2004; Gregory et al. 2006). In X-ray observations only the highest velocity regions can be probed, where the temperature is reaches a few MK. All accretion ragions with infall velocities below about 450 km s^{-1} are X-ray dark. We stress that the shock takes place inside the optically thick stellar atmosphere, but still the photons can escape through the thinner cooling flow and pre-shock zone. This picture is fully consistent with the meassured column densities.

4. Conclusions

Accretion shocks are an important contributor to the X-ray emission from V4046 Sgr. An detailed model of the accretion shock well explains the density sensitive line ratios. It allows to estimate the infall parameters and infer a mass accretion rate based on X-ray observations alone. In addition V4046 Sgr is found to posses a ”normal“ stellar corona.

Acknowledgements. H.M.G acknowledges support from the DLR under grant 50OR0105.

References

Feigelson, E. D. & Montmerle, T. 1999, ARA&A, 37, 363

Gregory, S. G., Jardine, M., Simpson, I., & Donati, J.-F. 2006, MNRAS, 371, 999

Günther, H. M., Liefke, C., Schmitt, J. H. M. M., Robrade, J., & Ness, J.-U. 2006, A&A, 459, L29

Günther, H. M., Schmitt, J. H. M. M., Robrade, J., & Liefke, C. submitted to A&A

Kastner, J. H., Huenemoerder, D. P., Schulz, N. S., Canizares, C. R., & Weintraub, D. A. 2002, ApJ, 567, 434

Koenigl, A. 1991, ApJ, 370, L39

Quast, G. R., Torres, C. A. O., de La Reza, R., da Silva, L., & Mayor, M. 2000, in IAU Symposium, 28P–+

Romanova, M. M., Ustyugova, G. V., Koldoba, A. V., & Lovelace, R. V. E. 2004, ApJ, 610, 920

Schmitt, J. H. M. M., Robrade, J., Ness, J.-U., Favata, F., & Stelzer, B. 2005, A&A, 432, L35

Shu, F., Najita, J., Ostriker, E., et al. 1994, ApJ, 429, 781

Stelzer, B. & Schmitt, J. H. M. M. 2004, A&A, 418, 687

Chapter 6

Where are the hot ion lines in classical T Tauri stars formed ?

H.M. Günther and J.H.M.M. Schmitt
Astronomy & Astrophysics, 481, 735 (2008)

A&A 481, 735–745 (2008)
DOI: 10.1051/0004-6361:20078674

Astronomy & Astrophysics

Where are the hot ion lines in classical T Tauri stars formed?

H. M. Günther and J. H. M. M. Schmitt

Hamburger Sternwarte, Universität Hamburg, Gojenbergsweg 112, 21029 Hamburg, Germany
e-mail: moritz.guenther@hs.uni-hamburg.de

Received 14 September 2007 / Accepted 14 January 2008

ABSTRACT

Context. Classical T Tauri stars (hereafter CTTS) show a plethora of in- and outflow signatures in a variety of wavelength bands.
Aims. In order to constrain gas velocities and temperatures, we analyse the emission in the hot ion lines.
Methods. We use all available archival *FUSE* spectra of CTTS to measure the widths, fluxes and shifts of the detected hot ion lines and complement these data with *HST/GHRS* and *HST/STIS* data. We present theoretical estimates of the temperatures reached in possible emission models such as jets, winds, disks and accretion funnels and look for correlations with X-ray lines and absorption properties.
Results. We find line shifts in the range from -170 km s^{-1} to $+100$ km s^{-1}. Most linewidths exceed the stellar rotational broadening. Those CTTS with blue-shifted lines also show excess absorption in X-rays. CTTS can be distinguished from main sequence (hereafter MS) stars by their large ratio of the O VII to O VI luminosities.
Conclusions. No single emission mechanism can be found for all objects. The properties of those stars with blue-shifted lines are compatible with an origin in a shock-heated dust-depleted outflow.

Key words. stars: formation – stars: winds, outflows – ultraviolet: stars

1. Introduction

T Tauri stars (TTS) are young (<10 Myr), low mass ($M_* < 3\ M_\odot$), pre-main sequence stars exhibiting strong Hα emission. The subclass of Classical TTS (CTTS) are accreting material from a surrounding disk. This disk is truncated close to the corotation radius by interaction with the magnetic field. At the inner rim, the material is ionised by the stellar radiation and loaded onto the field lines (Uchida & Shibata 1984; Koenigl 1991) and accelerated to nearly free-fall velocity along an accretion funnel before hitting the stellar surface where an accretion shock forms. Angular momentum may be transferred from the star to the disk by magnetic torque (Shu et al. 1994), at the same time this process is expected to drive outflows possibly in the form of a disk wind or bipolar jets. Romanova et al. (2004) performed full magneto-hydrodynamic (MHD) calculations of the accretion geometry, while the accretion shock and its post-shock cooling zone were simulated by different authors (Calvet & Gullbring 1998; Lamzin 1998; Günther et al. 2007).

Observational support for the scenario described above is found in data from different wavelength bands. The shocked material is heated up to temperatures in the MK range and should produce copious amounts of X-ray emission. Density-sensitive X-ray line ratios strongly suggest a post-shock origin (Günther et al. 2007) of the cool parts of the plasma observed at X-ray wavelengths, and the cooling matter veils absorption lines in the optical and infrared (Calvet & Gullbring 1998). The geometry of the pre-shock accretion funnel can be traced by Hα line profile analysis (Muzerolle et al. 2000). Undoubtedly CTTS also show outflows (a review is given by Bally et al. 2007), however, the precise origin and the physical driving mechanism(s) are uncertain. Theoretical models propose a variety of collimated stellar outflows and disk winds to remove angular momentum from the system (Shu et al. 1994; Matt et al. 2002; Gómez de Castro & Ferro-Fontán 2005; Pudritz et al. 2007). The outflows can take the form of winds observed from radio to the UV (e.g. Alencar & Basri 2000; Beristain et al. 2001; Lamzin et al. 2004; Dupree et al. 2005a; Edwards et al. 2006), or collimated, often bipolar jets, again observed at different wavelength bands (Rodriguez 1995; Coffey et al. 2004; Güdel et al. 2005). The dynamics of the surrounding gas have been successfully probed by UV spectroscopy with *HST/GHRS*, *HST/STIS* and *FUSE*, especially in the H_2 lines, which show outflows and fluorescence on the hot disk surface (Ardila et al. 2002a,b; Herczeg et al. 2002, 2005, 2006). In the specific case of TW Hya, Dupree et al. (2005a) claim the existence of a warm/hot wind. Their conclusion assumes that the CIII and OVI lines have an intrinsic Gaussian shape, with the centroid matching the stellar rest-frame. The observed asymmetry of the CIII and OVI line-profiles can then be explained by the presence of a continuous and smoothly-accelerated hot wind absorbing the radiation in the blue wing of these particular lines. However, Johns-Krull & Herczeg (2007) argue that this model is incompatible with *HST/STIS* observations, especially for the C IV 1550 Å doublet. The existence of a hot wind in TW Hya, therefore, remains an open issue.

In this paper we analyse the shifts and widths of hot-ion spectral lines, particularly C III 977 Å and the O VI doublet at 1032 Å and 1038 Å, observed with *FUSE*. This complements earlier studies of all pre-main sequence stars observed with *IUE* (Valenti et al. 2000), *GHRS* (Ardila et al. 2002a,b) and of the H_2 emission in CTTS (Herczeg et al. 2006). In Sect. 2 we briefly summarise the properties of the sample stars, and in Sect. 3 we describe the observations and data that we use in our present analysis. In Sect. 4 the line profile analysis is presented, several possible formation regions for the observed properties are discussed in Sect. 5, and in Sect. 6 we summarise our results.

2. Stellar properties

In this section we present the most important properties of our sample stars in Table 1 and provide a short summary of their main characteristics.

2.1. RU Lupi

RU Lupi is a strong accretor, heavily-veiled and strongly variable at different wavelengths (Stempels & Piskunov 2002). Its period is uncertain. A wind can be studied using cool, metallic lines with a low first-ionisation potential, and in H_2 as demonstrated by Herczeg et al. (2005). The line profiles of hot ion lines in the UV exhibit complex structures. Takami et al. (2001) show by spectro-astrometry that the Hα emission is significantly extended and compatible with a bipolar outflow. In X-rays, RU Lupi is observed to be a typical member of the CTTS class (Robrade & Schmitt 2007); specifically, it shows a low f/i-ratio in the O VII triplet as well as a soft X-ray excess.

2.2. T Tau

T Tau is the defining member of the class of TTS. It is a hierarchical triple system, where the northern component T Tau N is optically visible, while the southern component T Tau S, contributing mainly in the infrared, is itself a binary (Koresko 2000). The T Tau system shows a very significant soft X-ray excess without the high densities seen in TW Hya (Güdel et al. 2007). Nevertheless, accretion and winds are detectable using data for other wavelengths (van Langevelde et al. 1994b,a; Dupree et al. 2005a), and Herczeg et al. (2006), for example, attribute observed fluorescent H_2 emission to outflows. The first analysis of this FUSE data, completed by Wilkinson et al. (2002), provided the first discovery of extra-solar, H_2 Werner-band emission.

2.3. DF Tau

DF Tau is a binary system consisting of two M stars, resolved for the first time by Chen et al. (1990). The orbital parameters are still uncertain after several revisions (Schaefer et al. 2006) and the distance of the system is still a matter of debate. The most reasonable estimate is provided by Bertout & Genova (2006), who showed DF Tau to be a member of the Taurus-Aurigae moving group (≈140 pc), in spite of its low *HIPPARCOS* parallax of 39 ± 7 pc. Lamzin et al. (2001) present *HST/STIS* and *IUE* spectra showing accretion and wind signatures and attribute DF Tau's erratic photometric variability to unsteady accretion. DF Tau is one of few Doppler-mapped CTTS (Unruh et al. 1998). Herczeg et al. (2006) demonstrated that fluorescent H_2 emission found in *FUSE* observations is consistent with models of a warm disk surface. X-ray observations for DF Tau are discussed in Sect. 3.3.

2.4. V4046 Sgr

Sallmen et al. (2000) present the *FUSE* spectrum of V4046 Sgr. V4046 Sgr is a close binary system with separation of ≈9 $R_\odot$ (Quast et al. 2000). Both of the components are almost identical CTTS, which are accreting matter from a circumbinary disk. *Chandra* X-ray observations show line ratios indicative of high density plasma, which cannot be explained by coronal activity, but must be attributed to hot accretion shocks (Günther et al. 2006).

2.5. TWA 5

Sallmen et al. (2000) present the *FUSE* spectrum of TWA 5. TWA 5 is a hierarchical multiple system, the main component being a M 1.5 dwarf. On the one hand, TWA 5 has no significant infrared excess indicating the absence of a disk (Metchev et al. 2004; Weinberger et al. 2004; Uchida et al. 2004); also, X-ray observations by Argiroffi et al. (2005) suggest that the emission originates in a low-density region, not in an accretion shock. On the other hand, TWA 5 has an Hα equivalent width of 13.5 Å and signatures of outflows (Mohanty et al. 2003), therefore we regard it as a transition object.

2.6. GM Aur

GM Aur is one of the most popular systems to observe stellar disk constitution and chemistry (e.g. Bergin et al. 2004; Hueso & Guillot 2005; Salyk et al. 2007). Numerous observations in the radio use the disk of GM Aur to analyse the distribution and evolution of dust grains in the disk (e.g. Rodmann et al. 2006; Schegerer et al. 2006). Based on an optically-thin inner disk surrounded by an optically-thick outer region, Najita et al. (2007) classify GM Aur as a transition object. X-ray observations for GM Aur are discussed in Sect. 3.3.

2.7. TW Hya

Because of its proximity and the absence of a surrounding dark molecular cloud, TW Hya is a key system for the study of CTTS. Although relatively old by comparison (≈10 Myr), it is still actively accreting from a surrounding disk. Eisner et al. (2006) interferometrically resolve its disk and Herczeg et al. (2004) constrain the inner disk temperature to about 2500 K using H_2 fluorescence in *HST/STIS* and *FUSE* data. Observations with *STIS* and *FUSE* show, in addition to H_2, atomic emission lines with notably asymmetric shapes. The analytical models expect a cold wind to be driven by magnetic fields from the disk (Shu et al. 1994), and this can be traced observationally from single or double ionised ions (Lamzin et al. 2004). TW Hya has been extensively observed in X-rays, which revealed a comparatively cool and dense emission region interpreted as signature of an accretion hot spot (Kastner et al. 2002; Stelzer & Schmitt 2004). Our own theoretical modelling supports this view (Günther et al. 2007).

3. Observations

3.1. FUSE *data*

In order to perform a systematic study of the FUV properties of CTTS, we retrieved all available *FUSE* observations of TTS from the archive. For a comparison with "normal" stars, we selected two main sequence stars, the rapidly-rotating K star AB Dor and the solar analog α Cen A. Table 2 lists the observation logs; all targets except α Cen A are observed using the LWRS aperture with $30'' \times 30''$ field of view. We reduced the data with CalFUSE v3.2.0 (Dixon et al. 2007), performing extractions of the complete data set and night-only time intervals to check for airglow contamination. With the exception of GM Aur, the spectral regions of interest are not affected by airglow. To coadd the individual exposures, we used the CalFUSE `get_shift` task and applied two different methods: both methods involved cross-correlation, the first using a stellar emission line (O VI 1032 Å on the 1aLiF detector and C III 977 Å on the

Table 1. Stellar sample properties, N_H lists only values derived from X-ray observations.

Star	Spectral type	d [pc]	v_{rad} [km s^{-1}]	$v \sin i$ [km s^{-1}]	i [°]	N_H [10^{21} cm^{-2}]	A_V [mag]
RU Lup	G5V	140	−1.9 ± 0.02 (17)	9.1 ± 0.9 (17)	24 (19)	1.8 (15)	0.07 (9)
T Tau	G5V	140	18 (9)	20 ± 5 (9)	15 (9)	5 (5)	0.3 (9)
DF Tau	M0-2	140	21.6 ± 9.2 (4)	15.8 ± 1.0 (7)	>60 (21)	3-8	0.5 (9)
V4046 Sgr	K5	83	−6.94 (12)	14.9 ± 0.9 (18)	35 (18)	<2 (6)	0.0 (18)
TWA 5	M3V	57	14 (20)	uncertain (20)	n.a.	0.3 (2)	n.a.
GM Aur	K5V	140	24 (10)	13 (3)	56 ± 2 (16)	0.2-0.4	0.31 (11)
TW Hya	K8V	57	12.5 ± 0.5 (1)	5 ± 2 (1)	7 ± 1 (13)	0.35 (14)	0.0 (8)

References: (1) Alencar & Batalha (2002); (2) Argiroffi et al. (2005); (3) Basri & Batalha (1990); (4) Bouvier et al. (1986); (5) Güdel et al. (2007); (6) new fits to the data from Günther et al. (2006); (7) Hartmann & Stauffer (1989); (8) Herczeg et al. (2004); (9) Herczeg et al. (2006); (10) Joy (1949); (11) Muzerolle et al. (1998) (12) Quast et al. (2000); (13) Qi et al. (2004); (14) Robrade & Schmitt (2006); (15) Robrade & Schmitt (2007); (16) Simon et al. (2000); (17) Stempels & Piskunov (2002); (18) Stempels & Gahm (2004); (19) Stempels et al. (2007); (20) Torres et al. (2003); (21) Unruh et al. (1998).

2bSiC detector), and the second method using a strong airglow line (H Lyβ and H Lyγ). Airglow lines completely cover the aperture and cannot therefore be used to judge centering of a target. We studied all stellar spectra with O VI and C III lines sufficiently strong for cross-correlation, and found no significant differences between the line profiles derived using both methods. Using airglow lines does, however, at times enable H_2 emission to be detected in the 1bLiF channel. This is in contrast to the less accurate cross-correlation achieved using low S/N stellar lines.

It seems that in our observations the targets did not drift through the apertures. Therefore we shift all airglow H Lyβ lines to match the laboratory wavelength. As the targets may be positioned differently in aperture we perform the following check: Herczeg et al. (2002) discovered molecular hydrogen at rest compared to the star, so we identify H_2 lines in the 1bLiF channel in TW Hya (the shift between channels a and b on the same chip is smaller than 8 km s^{-1}, Dixon et al. 2007); the shift of our H_2 lines should now match the radial velocity of TW Hya. This fixes our wavelength scale and from here on we use TW Hya as our reference spectrum. To avoid the need for a spectral identification, we search the 1bLiF channel of the other observations for strong features, which correlate with TW Hya. Only lines with the same strengths in full and night-only extractions are considered here. We also check that no airglow feature is expected at that position according to Feldman et al. (2001). The line widths we find are as small as expected (Herczeg et al. 2006), lending further credibility to the coaddition of single exposures using an airglow line. In addition, we cross-correlate larger regions of the spectra without strong airglow features and find that the required shifts are in agreement with the analysis of single lines. For RU Lup, T Tau and DF Tau we correct for the velocity of the H_2 outflow relative to the star from Herczeg et al. (2006). Taking into account the stellar radial velocities, the lines shifts confirm the shifts adopted above from the H Lyβ lines. For V4046 Sgr, we do not have a *HST/STIS* measurement of H_2 lines, and for TWA 5 and GM Aur no suitable features in the 1bLiF channel were found. However, given the success of the wavelength calibration for other stars, we are quite confident that it is reliable also in these cases. We estimate the total wavelength error in the 1a/bLiF channels to be 20 km s^{-1}. We then correlate the 2bSiC channel with the 1aLiF channel using the stellar O VI 1032 Å line. Unfortunately the signal-to-noise ratio (hereafter SNR) in 2bSiC is much lower than in 1aLiF and for T Tau, DF Tau and GM Aur we have to use the H Lyβ airglow line. Because the *FUSE* channels are not perfectly aligned, the position of the target in the various channels might be different; the wavelength calibration below 1000 Å for these three stars is therefore uncertain.

Table 2. *FUSE* observations.

Target	Date	Exposure time [ks]	Data ID
RU Lup	2001-08-28	24	A1090202
T Tau	2001-01-15	21	P1630101
DF Tau	2000-09-13	26	A1090101
V4046 Sgr	2000-05-18	16	P1920202
TWA 5	2000-05-15	15	P1920101
GM Aur	2004-03-03	32	D0810101
GM Aur	2004-10-23	34	D0810102
TW Hya	2000-06-03	2	P1860101
TW Hya	2003-02-20	15	C0670101
TW Hya	2003-02-21	15	C0670102
AB Dor	1999-10-20	22	X0250201
AB Dor	1999-12-14	24	X0250203
AB Dor	2003-12-26	102	D1260101
α Cen A[1]	2001-06-25	15	P1042601
α Cen A[1]	2006-05-05	13	G0810102

Notes: (1) MDRS aperture.

For data of low SNR CalFUSE sometimes overcorrects the background, leading to negative flux intensity values; we therefore always separately fit the background in line-free regions, close to the line of interest.

3.2. HST *data*

Four of our sample stars (RU Lup, T Tau, DF Tau and TW Hya) have been observed with gratings onboard of the *HST*. RU Lup, T Tau and DF Tau were observed with the *GHRS*; these observations are presented by Ardila et al. (2002a) and Lamzin et al. (2001) and we adopt the linewidths and shifts measured by these authors. The *STIS* observations of RU Lup were carefully analysed by Herczeg et al. (2005) and those of TW Hya by Herczeg et al. (2002) and Johns-Krull & Herczeg (2007). We use the *STIS* spectra of T Tau and DF Tau from CoolCAT (Ayres 2005), which is a database of reduced and calibrated UV spectra taken with *STIS* for cool stars. These spectra all belong to the *HST* program 8157 and were taken in the year 2000. The observations of TW Hya are not contained in CoolCAT, because they were taken in a non-standard setup. For a consistency check, we take T Tau, and find that the spectra presented there agree with the previously published results in Herczeg et al. (2005).

Table 3. *ROSAT* observations.

Target	Date	Exposure time [ks]	Obs ID
DF Tau	1993-08-93	10	WG201533P.N1
GM Aur	1992-09-22	1.3	WG201278P.N1
GM Aur	1993-03-04	4	WG201278P-1.N1

3.3. X-ray data

Most of our sample stars have been observed at X-ray wavelengths with *Chandra*, *XMM-Newton* or both, and we obtained these data from the literature. For DF Tau and GM Aur, there are no X-ray spectra available in the literature, however, both DF Tau and GM Aur have been observed with *ROSAT/PSPC* pointings. We therefore retrieved the *ROSAT* X-ray data from the archive in order to enlarge our sample for comparisons of optical and X-ray absorption. In Table 3, we provide information on the data used. The *ROSAT* data were reduced using EXSAS version 03Oct. Source photons were extracted from a circle with a radius of 2.5 arcmin to avoid contamination from nearby sources. The background was taken from a region close to the target without detected sources with a radius three times larger. We measured fluxes of 0.013 ± 0.002 cts s^{-1} for DF Tau and 0.021 ± 0.003 cts s^{-1} for GM Aur. Using MIDAS/EXSAS, we fitted Raymond-Smith and Mewe-Kaastra models assuming cold absorption. The ROSAT data are of low SNR. We therefore tried to use different data binnings and compared our final results. We provide a range of possible absorption column-densities in Table 1, because, as often found, observationally a large amount of cool plasma and small interstellar absorption lead to very similar signatures. To test the reliability of our procedure, we fit the *ROSAT* data for AB Aur, which is located in the same field as GM Aur. We measure an absorption column-denstiy $N_{\rm H}$ of $2–3 \times 10^{20}$ cm^{-2}, which is approximately half of the measurement derived using *XMM-Newton* data presented by Telleschi et al. (2007). We therefore conclude that, taking into account systematic errors, the *ROSAT*-derived absorption columns are consistent with those derived using *XMM-Newton* data.

4. Results

4.1. FUV lines

In Fig. 1, we present the C III line profiles at 977 Å and both components of the O VI doublet at 1032 Å and 1038 Å for our targeted stars. Each spectral line is fitted with a Gaussian profile and shown normalised with respect to the fitted peak value. The best-fit parameters for line flux, shift of the Gaussian-line centre, and its full width at half maximum (*FWHM*), ordered by the observed shift in the O VI 1032 Å line, are given in Table 4, where the shift is corrected for the radial velocity of the star. The statistical errors on the shift and the *FWHM* given in the table are typically comparable to our systematic calibration uncertainties. The systematic errors on the fluxes are of the order 10–20%. The O VI doublet line at 1032 Å is detected in all sample stars and the C III line in all except GM Aur. In all cases, the line shifts measured in the C III and O VI are consistent, arguing for related emission regions; only for T Tau is there a statistically significant difference, probably due to uncertainties in the wavelength calibration of 2SiC detector data, as discussed in Sect. 3.1.

In the case of RU Lupi, an absorption component is clearly visible in all three lines, which is also fitted with a Gaussian

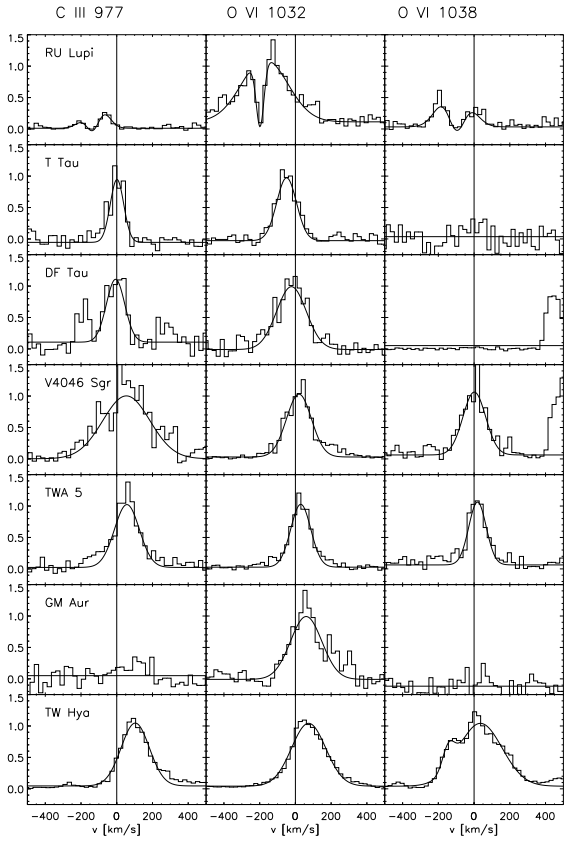

Fig. 1. Hot ion lines observed with *FUSE* in CTTS and best fit Gaussian profiles ordered by the shift in the O VI 1032 Å line. All line profiles are normalised to their the Gaussian profile peak value and rebinned to instrumental resolution.

absorption line. We note that this absorption is not self-absorption. Herczeg et al. (2005) identify the absorption in the O VI 1032 Å as H_2 6–0 P(3) shifted by -23 ± 5 km s^{-1} relative to the H_2 rest wavelength, and the absorption in O VI 1038 Å as C II. Using the package H2oolts (McCandliss 2003), we identify the absorption component in C III to be a superposition of the equally strong H_2 2–0 P(5) and 11–0 R(3) shifted by $\approx -10 \pm 15$ km s^{-1} again relative to the H_2 rest wavelength. Within the O VI 1038 Å line of TW Hya, we fit the C II blend on the blue side with an additional Gaussian component. Unfortunately the data quality does not enable further blends and features to be identified. In the *FUSE* bandpass, numerous fluorescent Lyman and Werner band H_2 lines are present, which are usually relatively sharp (Herczeg et al. 2006). The lines in Fig. 1 are well-described by one-peaked distributions, so the contribution of any individual blending line has to be small compared to the broad ion lines.

Atomic physics predicts that the 1032 Å component of the O VI doublet should be twice as strong as the 1038 Å component. We can confirm this prediction for the data of V4046 Sgr and TWA 5. In Table 4, significant deviations from the expected line ratio can be seen in RU Lup and TW Hya, where additional components complicate the fit. However, in the cases of T Tau, DF Tau and GM Aur the O VI 1038 Å line is almost

Table 4. *FUSE* best fit parameters, fluxes in 10^{-15} erg cm^{-2} s^{-1}, width and shift in km s^{-1}, errors are statistical only.

	C III 977 Å			O VI 1032 Å			O VI 1038 Å			C III 1175 Å
Star	Flux	Shift	*FWHM*	Flux	Shift	*FWHM*	Flux	Shift	*FWHM*	Flux
RU Lup	70 ± 60	−120 ± 10	120 ± 20	24 ± 6	−170 ± 20	300 ± 60	15 ± 8	−100 ± 20	170 ± 30	20 ± 2
– Absorption	−60 ± 40	−130 ± 10	100 ± 20	−4 ± 0	−200 ± 6	50 ± 20	−10 ± 2	−100 ± 10	120 ± 30	...
T Tau	10 ± 4	1 ± 13	90 ± 30	8 ± 2	−50 ± 10	130 ± 30	n.a.	n.a.	n.a.	18 ± 2
DF Tau	17 ± 6	−6 ± 12	120 ± 30	11 ± 3	−22 ± 16	200 ± 40	n.a.	n.a.	n.a.	44 ± 2
V4046 Sgr	60 ± 20	50 ± 20	310 ± 70	37 ± 6	19 ± 8	160 ± 20	16 ± 4	1 ± 12	150 ± 30	50 ± 3
TWA 5	30 ± 10	60 ± 20	160 ± 40	30 ± 5	30 ± 7	130 ± 20	14 ± 3	19 ± 9	110 ± 20	25 ± 2
GM Aur	n.a.	n.a.	n.a.	5 ± 1	60 ± 20	210 ± 60	n.a.	n.a.	n.a.	24 ± 2
TW Hya	200 ± 25	100 ± 6	190 ± 20	220 ± 20	74 ± 5	220 ± 15	100 ± 15	35 ± 15	290 ± 40	310 ± 4
– Blend	...	...	...	...	...	...	9 ± 9	−140 ± 14	80 ± 40	...

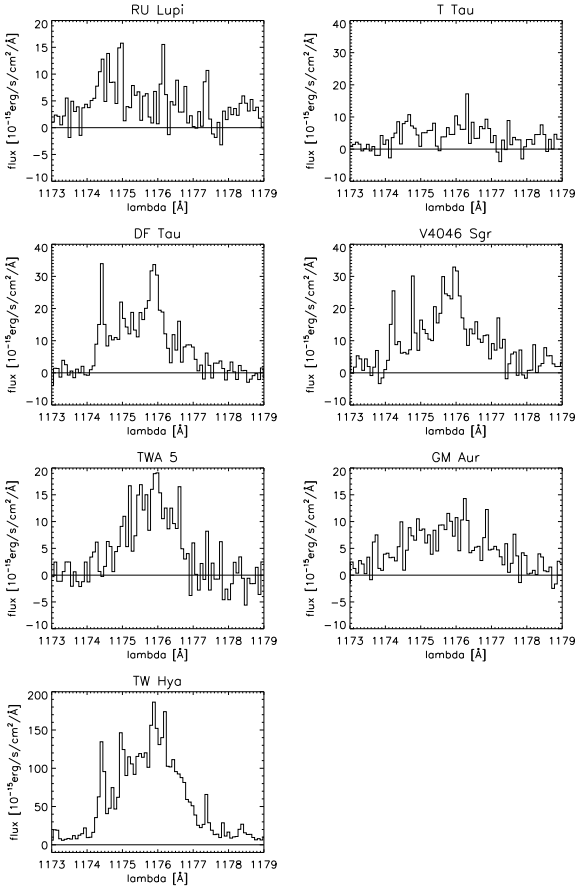

Fig. 2. The C III multiplet around 1175 Å rebinned to instrumental resolution.

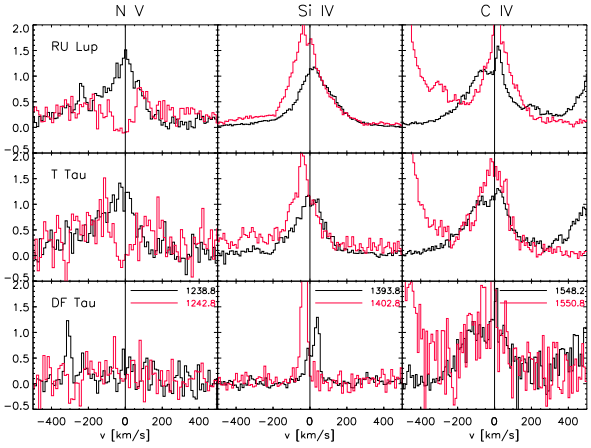

Fig. 3. Hot ion lines in the *STIS* spectra. The relative flux of the red doublet member is multiplied with a factor of 2 (red/grey lines).

completely absent, because of absorption by larger molecular hydrogen columns (see Table 1) in the lines H_2 5–0 R(1) at 1037.1 Å and 5–0 P(1) at 1038.2 Å. RU Lup and T Tau, both CTTS with blueshifted emission, are found to have the largest reddening and absorption column density.

In Fig. 2, we present the FUSE observations of the C III multiplet at wavelength 1175 Å. Unfortunately the SNR of the data is too low to be able to resolve the H2 lines, and to fit the individual line components. This analysis would have enabled density diagnostics to be measured. For RU Lup and T Tau in fact, the multiplet is barely detectable. Therefore a detailed Gaussian function fit yields no useful information, and in Table 4 we present only the total flux and its statistical error. The dereddened ratio of the fluxes in the C III 977 Å line and the 1175 Å multiplet is, in principle, density-sensitive in the range $8 < \log n < 11$ according to the CHIANTI database (Dere et al. 1998; Landi et al. 2006). However, apart from RU Lup the observed values are far below the predicted ratios. Redfield et al. (2002) have analysed this line ratio in *FUSE* observations of late-type dwarf stars, and Dupree et al. (2005b) for luminous cool stars. Both authors conclude that the C III 977 Å line is optically-thick in the transition region and that in addition there is strong interstellar line absorption.

The *STIS* data from CoolCAT is shown close to the hot ionic doublets N V 1240 Å, Si IV 1400 Å and C V 1550 Å in Fig. 3. In each case, the expected intensity ratio is two to one. To facilitate the comparison of the line profiles we show the flux of the red doublet member increased by a factor of two. In the absence of blending and interstellar absorption, both lines should show a perfect match. The red member of the N V doublet at 1242.8 Å is totally absorbed by an interstellar N I line, so we do not attempt to fit the line profile. For the other lines, the results of a fit with a single Gaussian component are shown in Table 5. In DF Tau there is no overlap between the two lines shown in the middle panel of Fig. 3. Therefore they cannot be doublet members, but have to be other lines, likely H_2. These lines also distort the red member of this doublet in the other two stars, leading to a shifted centre in the Gaussian fit. The large errors result from generally non-Gaussian line shapes. The Table also includes the *GHRS* data and the observations of TW Hya, resembling the

Table 5. *HST* best fit parameters, for references see Sect. 3.2.

Star	Instr.	N V 1239 Å		Si IV 1394 Å		Si IV 1403 Å		C IV 1548 Å		C IV 1551 Å	
		Shift	*FWHM*	Shift	*FWHM*	Shift	*FWHM*	Shift	*FWHM*	Shift	*FWHM*
		km s^{-1}	km s^{-1}	km s^{-1}	km s^{-1}	km s^{-1}	km s^{-1}	km s^{-1}	km s^{-1}	km s^{-1}	km s^{-1}
RU Lup	GHRS	...	...	5 ± 5	270 ± 10	−31 ± 6	250 ± 10	−20 ± 20	340 ± 40	−10 ± 10	300 ± 30
RU Lup	STIS	−15 ± 25	190 ± 70	26 ± 20	200 ± 50	−20 ± 20	180 ± 50	−25 ± 25	230 ± 80	15 ± 18	120 ± 50
T Tau	GHRS	...	...	−15 ± 7	220 ± 20	−50 ± 10	220 ± 30	−25 ± 6	250 ± 10	0 ± 6	150 ± 10
T Tau	STIS	−45 ± 30	220 ± 80	−1 ± 20	180 ± 50	−40 ± 20	130 ± 50	−25 ± 20	230 ± 70	−10 ± 20	150 ± 50
DF Tau	GHRS	...	...	...	300	...	300	10 ± 10	350 ± 30	10 ± 10	320 ± 20
DF Tau	STIS	30 ± 40	187 ± 85	...	...	...	...	−40 ± 40	230 ± 100	−50 ± 40	180 ± 120
TW Hya	STIS	redshifted, see text		42 ± 3	170 ± 6	9 ± 3	130 ± 8	redshifted, non-Gaussian, see text			

FUSE data. These profiles are nearly triangular, rising sharply close to the rest wavelength and extending to about 400 km s^{-1} on the red side (see Fig. 7 in Herczeg et al. 2002). Of similar shape, although extending only to 200 km s^{-1} on the red side, is the C IV 1550 Å doublet in DF Tau (Lamzin et al. 2001) in the *GHRS* observation. This data is fitted with multiple Gaussians by Ardila et al. (2002a). We give here the values for the dominant component only.

Despite the uncertainties in the profiles of individual lines, it is obvious from Tables 4 and 5 and Figs. 1 and 3, that FUV lines in CTTS cover a range of wavelength shifts from blue-shifted to red-shifted velocities of the order of −200 km s^{-1} out to 100 km s^{-1}, and could therefore potentially originate in in- or outflows or both. RU Lup clearly shows blue-shifted emission, the same is likely the case for T Tau, because the O VI shift can be more accurately determined than the C III shift. DF Tau and V4046 Sgr are consistent with centred lines and TWA 5, GM Aur and TW Hya with red-shifted lines.

4.2. Excess absorption

In Fig. 4, we show the absorbing column densities as fitted to the X-ray observations and optical A_V values. With a standard gas-to-dust ratio, they should be related through the formula $N_H = A_V \cdot 2 \times 10^{22}$ cm^{-2} (Savage & Mathis 1979; but see Vuong et al. 2003, for a compilation of other conversion factors in the literature, all roughly consistent with this value). The determination of A_V values is difficult for CTTS, where not only the spectral type, but also the veiling needs to be known to compute the intrinsic colours. This renders A_V values in the literature notoriously uncertain, especially if they are based only on photometric and not on spectroscopic information. We have tried to compile the best available estimates in Table 1. For AA Tau and possibly other CTTS, the circumstellar absorption and the veiling are time-dependent. In Fig. 4, we show mean values for AA Tau from Schmitt & Robrade (2007) and Bouvier et al. (1999). The A_V for T Tau is often given one magnitude larger than the value we use, but Walter et al. (2003) convincingly show that this is an overestimate. In the case of DF Tau, most values are between 0.21 (Kenyon & Hartmann 1995) and 0.55 (Strom et al. 1989), with the exception of 1.9 ± 0.6 in Cohen & Kuhi (1979); for RU Lup, all modern measurements agree on the low A_V value (Lamzin et al. 1996; Stempels & Piskunov 2002; Herczeg et al. 2005). In addition to the TTS studied in this paper, we included data for the young stars BP Tau and SU Aur from Robrade & Schmitt (2006) and Errico et al. (2001), for BP Tau, AB Aur and HD 163296 from Telleschi et al. (2007, see references therein) and for MP Mus from Argiroffi et al. (2007) and Mamajek et al. (2002). In the case of AA Tau, reddening and absorbing column are exceptionally large, because this object is seen almost edge-on.

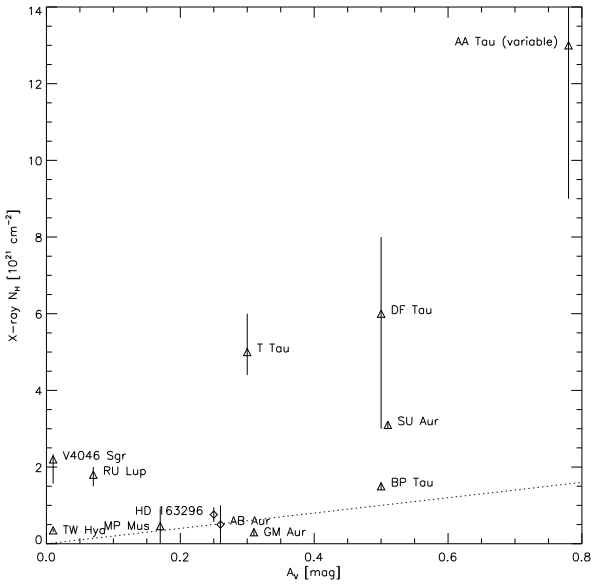

Fig. 4. Optical reddening and absorbing column density from X-rays. Error bars represent 90% confidence intervals on the N_H fit, except for DF Tau and GM Aur where we give the (tighter) ranges discussed in Sect. 3.3. The dotted line indicates the values predicted using $N_H = A_V \cdot 2 \times 10^{22}$ cm^{-2}.

AA Tau, DF Tau, T Tau, RU Lup and V4046 Sgr all show much larger X-ray absorbing columns than expected from the optical extinction, indicating large amounts of gas with a very small dust content compared to the interstellar medium. This effect is significantly larger than the uncertainties in the A_V and N_H values. In V4046 Sgr the relative uncertainties are higher compared to the other stars, because *Chandra* is not as sensitive as *XMM-Newton* at soft X-ray energies. In RU Lup and, possibly, T Tau the hot ion lines exhibit significant blue shifts. Therefore, it may well be that the hot UV-emitting plasma provides the observed X-ray excess absorption.

All N_H values provided are obtained by fitting a cold absorber model, implying that the elements contributing to the X-ray absorption are not fully ionised. The most important elements are O, H, and He; with increasing temperature and ionisation an even larger column density is necessary to provide the observed absorption.

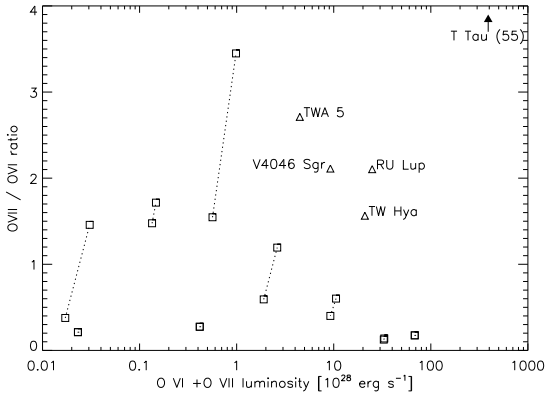

Fig. 5. Ratio of dereddened fluxes in the O VII triplet at 22 Å to the O VI 1032 Å line vs. total luminosity in those lines for CTTS (triangles) and other stars (squares). See text for data sources.

4.3. Ratio of O VII to O VI luminosity

X-ray data are available for all CTTS sample stars, most of which were observed using gratings. The resolution of these X-ray lines is insufficient to determine velocities, and we therefore analyse only the measured line fluxes. In Fig. 5, we compare the fluxes of the O VI and O VII lines, where the X-ray data is taken from the same references as N_H in Table 1. The observed fluxes are dereddened (Cardelli et al. 1989) in the UV with a standard dust grain distribution assuming $R_V = 3.1$, and in the X-rays following the cold absorption model by Balucinska-Church & McCammon (1992). For comparison, some stars with "normal" coronal X-ray emission have been added (Ness et al. 2004), whose O VI emission is known (Redfield et al. 2002; Dupree et al. 2005b). Where Ness et al. (2004) provide measurements from both *XMM-Newton* and *Chandra*, we show two connected symbols to give an idea of the intrinsic variability of the sources. This by far dominates the observational uncertainties, which are approximately 10%. As is clear from Fig. 5, the CTTS separate well out in the upper right corner of the plot, indicating an O VII excess compared to dwarf and giant cool stars. Robrade & Schmitt (2007) and Güdel & Telleschi (2007) show a very similar analysis using the O VIII/O VII ratio again with an O VII excess. These studies clearly show that the observed excess radiation of CTTS is confined to a relatively narrow temperature range about the formation of the He-like O VII triplet at 1–2 MK. We note that the CTTS T Tau has an unusually strong O VII excess, with a ratio close to 55. Estimating the H_2 column density to be roughly a quarter of the total neutral hydrogen absorbing column (Bloemen 1987), no more then about a third of the O VI flux in T Tau could be absorbed and the true blueshift cannot exceed 100 km s^{-1}. Otherwise emission blueward of the absorbing H_2 P(3)(6–0) line at 1031.19 Å would be observed in Fig. 1. Absorption in the O VI lines cannot therefore explain the extreme O VII to O VI ratio. A possible origin for the large emission measure at 1–2 MK might be a small-density accretion shock with a large filling factor.

5. Interpretation

In the following we attempt to constrain the emission regions and set limits and constraints on possible models for the origin of the observed line shapes.

5.1. Blue-shifted emission

The detected emission of hot-ion lines in the *FUSE* data appears blue-shifted in RU Lupi and, probably, in T Tau. Both systems show small values of $v \sin i$ compared to zero-age main-sequence stars and their inclination is close to face-on (Table 1). However, TW Hya is a counter-example with small inclination and red-shifted emission.

5.1.1. Shocks in outflows

We assume that an outflow exists, produced by either a disk or stellar wind. Blue-shifted emission could then be due to either internal shock fronts or to termination shocks of outflows running e.g. into an ISM cloud. For the case of RU Lupi, the measured centroid velocity is found to be $v_{obs} \approx 200$ km s^{-1} away from the star, and the peak formation temperature of O VI is 300 000 K (Mazzotta et al. 1998). If we assume that the O VI gas is heated by a strong shock wave, following Zel'Dovich & Raizer (1967) we can infer that the shock front properties from the Rankine-Hugoniot jump conditions. The emission of a post-shock cooling zone would be observed with velocity v_{obs}, which sets a lower boundary on the shock velocity v_{shock} to

$$4v_{obs} = v_{shock} \geq 800 \text{ km s}^{-1}. \quad (1)$$

By using line shifts we measure only the line of sight velocity, but RU Lupi and T Tau are probably viewed close to pole-on, thus we expect this value to be close to the true velocity. Typical jets reach up to 400 km s^{-1} (Eislöffel & Mundt 1998), but Rodriguez (1995) report velocities of up to 1000 km s^{-1}. The highest bulk velocities observed in the jet of the CTTS DG Tau are about 500 km s^{-1} (Lavalley-Fouquet et al. 2000). Using the strong shock formula the post-shock temperature T_{post} can be obtained by

$$T_{post} = \frac{\gamma - 1}{(\gamma + 1)^2} \frac{2\mu m_H}{k} v_{shock}^2 = \frac{3\mu m_H}{k} v_{obs}^2, \quad (2)$$

where m_H is the mass of an hydrogen atom, μ the dimensionless mean particle mass, k is Boltzmann's constant and γ is the adiabatic index. In the last step, we use $\gamma = 5/3$ for an ideal gas and Eq. (1). The estimated post-shock temperatures of $\approx 2 \times 10^6$ K for RU Lup and $\approx 2 \times 10^5$ K for T Tau are large enough to form O VI and O VII. This seems plausible, because Güdel et al. (2005) present already spatially-resolved X-ray emission from a CTTS jet in DG Tau A. The shifts of the O VI lines observed in RU Lup and T Tau are larger than measured for the C III lines, agreeing with models of post-shock cooling. C III is formed at lower temperatures, when the post-shock flow has lost energy, cooled and slowed down.

The observed volume emission measures (in units of 10^{51} cm^{-3}) for RU Lup, T Tau and DF Tau in the O VI 1032 Å and 1038 Å lines are 1.3, 1.4 and 4.7, assuming the temperature of maximum emissivity and dereddening of fluxes by Cardelli et al. (1989); for C III the corresponding numbers are 3.9, 1.5 and 8.0. Along the jet of the CTTS DG Tau pre-shock densities between 10^3 and 10^5 cm^{-3} are observed, with the higher values closer to the star (Lavalley-Fouquet et al. 2000). We now use the fit-formula from Hartigan et al. (1987) to estimate the cooling distance d and we find $d \approx 3 \times 10^{16}$ cm for RU Lup with $v = 800$ km s^{-1} and $n = 10^4$ cm^{-3}. The diameter of the jet is then of the order 10^{13} cm and the column density of the cooling

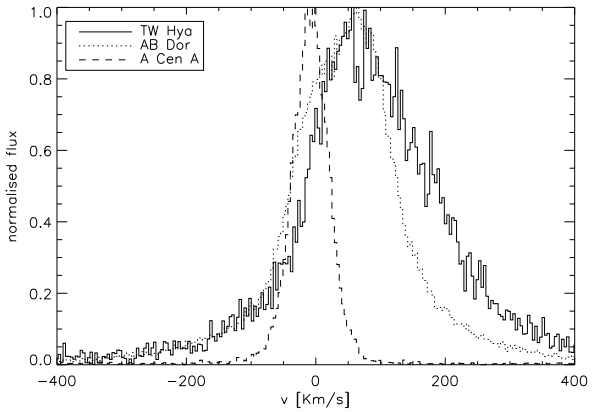

Fig. 6. Comparison of the O VI 1031.91 Å line for three stars.

zone alone $N_H = 3 \times 10^{20}$ cm^{-2}, adding to the absorbing column in the base of the jet, the circumstellar material further out and the interstellar column density. Therefore the large column densities observed for the stars with blue-shifted emission might be partly due to jet material. In T Tau and DF Tau the observed velocities are lower, which results in $d \approx 3 \times 10^{14}$ cm. This is too small to explain the observed emission measures. In the jet emission picture this suggests jets inclined to the line of sight, so the velocities and therefore the cooling distances are underestimated. According to the data in Table 1, the inclination of T Tau is smaller than the inclination of RU Lup, but it is not clear if jets are always orientated perpendicular to the accretion disk. DF Tau has the largest inclination, so we expect to see the jet at a high inclination. This might explain the large emission measure despite the low observed shift, which is even consistent with centred emission.

It could thus well be that the additional absorption of the stellar X-ray emission is due to the hot gas from which the FUV lines originate.

5.2. Anomalous line widths

A comparison of rotational velocities listed in Table 1 with the line widths shown in Tables 4 and 5 shows that the observed lines are superrotationally-broadened despite the measurement uncertainties. This is not uncommon in late-type stars (Wood et al. 1997). To illustrate this issue further, in Fig. 6 we compare the O VI 1032 Å line measured for TW Hya, the much more rapidly rotating K dwarf AB Dor with $v \sin i = 100 \pm 5$ km s^{-1} (Vilhu et al. 1987), and the slow-rotator α Cen with $v \sin i = 2.7 \pm 0.7$ km s^{-1} (Saar & Osten 1997) is in fact comparable to TW Hya. Ake et al. (2000) found significantly superrotationally-broadened coronal lines already in AB Dor and speculate that this might be due to microflare heating. The blue wing of TW Hya matches the data from AB Dor quite well, but the asymmetric profile from TW Hya is significantly different on the red side. At any rate, the O VI 1032 Å is clearly far broader than the line from α Cen. In CTTS, redward line asymmetries are usually attributed to emission in the accretion process. We therefore consider if this interpretation is also valid for TW Hya.

5.3. Magnetospheric infall

5.3.1. The basic model

In the standard accretion scenario for CTTS, the disk is truncated at a few stellar radii and the temperatures on the disk surface are a few thousand K at most (Herczeg et al. 2004). Consequently, excluding additional energy deposition by magnetic star-disk interaction, the accreting material reaches the formation temperature of O VI for the first time shortly before it passes through the accretion shock. At this stage, the material on the opposite side of the star ought to be blocked from view and only the low velocity, low temperature zones of the accretion funnel, close to their origin on the disk, can be seen blue-shifted if they face the observer. Therefore hot ion lines can be observed only red-shifted from the funnel flow.

Using the CHIANTI 5.2 database (Dere et al. 1998; Landi et al. 2006) we have numerically modelled the accretion spot as described in detail by Günther et al. (2007) for TW Hya and for V4046 Sgr (Günther & Schmitt 2007). We measure the infall velocities in the accretion funnel to be 525 km s^{-1}, and the pre-shock densities around 10^{12} cm^{-3} for TW Hya and 2×10^{11} cm^{-3} for V4046 Sgr. This matter passes through a shock on the stellar surface and is heated up to temperatures of $\approx 2 \times 10^6$ K. X-ray emission is produced in the following cooling flow in the post-shock zone. We explicitly calculate the ionisation and recombination rates, to be able to assess the ionisation state at each depth. Fitting this model to high-resolution X-ray data, we measure the abundances of the most important elements and determine mass accretion rates and filling factors between 0.1–0.4%.

Our model explicitly assumes optically thin-radiation loss. Along the direction of infalling flow, most resonance lines are found to be optically-thick up to optical depths above 10. The opacity is measured using a simple opacity calculation, and its precise value depends on both the infall density and elemental abundance. In the He-like triplets of Ne IX and O VII, observed in X-rays, the ratio of resonance line to intercombination plus forbidden line is expected to be close to unity from atomic physics. This is matched by observations, so we can infer that the resonance lines do not suffer much absorption. We note that the detailed accretion region geometry is unknown. In particular, the system geometry is probably not 1D and photons may well escape through the boundaries of the system rather than along the direction of flow. Unfortunately, this leads to considerable uncertainty in the computed flux. In our simulation however, emission is generated in the post-shock region to the same extent as observed for the OVI triplet, but the post-shock contribution to the CIII line is small. We caution that this conclusion is based on the assumption of very small and hot spots. Theoretical simulations of the infall geometry using either dipolar fields (Romanova et al. 2004) or more realistic geometries scaled from other stars (Gregory et al. 2006) suggest inhomogeneous spots with a distribution of infall velocities. In accretion zones with smaller infall velocities, the post-shock temperatures and hence the emitted X-ray fluxes are smaller. Such effects are not included in our models, but could contribute to the observed FUV flux. We are unable to reliably constrain fits of inhomogeneous spots due to insufficient diagnostics.

5.3.2. Predicted UV line shifts

For TW Hya and V4046 Sgr, where we modelled the accretion shock in detail, the largest possible post-shock speed is 125 km s^{-1}, a quarter of the free-fall velocity. All emission

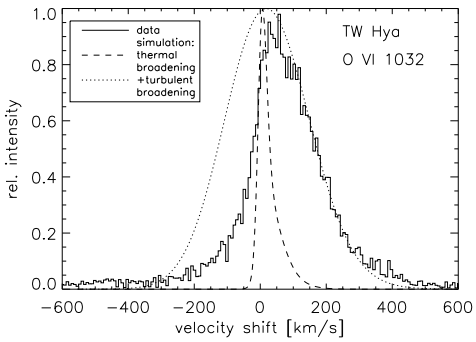

Fig. 7. O VI line at 1032 Å. Solid line: FUSE data, dashed line: simulation with purely thermal broadening, dotted line: simulation with additional turbulent broadening of 150 km s^{-1}

redward of this value must originate in the pre-shock radiative precursor.

During the cooling behind the shock front, the velocity decreases further. The emission from C III and O VI peaks at very low velocities. For pre-shock velocities of 300 km s^{-1}, O VI is formed immediately behind the accretion shock. Its velocity reaches a maximum value of 75 km s^{-1}, and decreases as the cooling proceeds. Depending on the stellar inclination and the spot latitude, the projected velocity may be even smaller. The resulting line profile has its maximum close to $v = 0$ km s^{-1} with a broad wing on the red side. Observationally the O VI line at 1032 Å is best suited for analysis, because the other member of the doublet at 1038 Å is more strongly absorbed by H_2 and possibly by C IV lines. The observed *FWHM* is about 200 km s^{-1} (Fig. 7). Adding turbulent broadening to our 1D simulation results in more symmetric line profiles, the red wing can be fitted with $v_{\rm turb} = 150$ km s^{-1}, but no blue wing is observed. In principle, this could be due to wind absorption, as suggested by Dupree et al. (2005a). In the case of TW Hya however, Johns-Krull & Herczeg (2007) were able to demonstrate that a hot wind is incompatible with, for example, the observed C IV line profiles.

5.3.3. Model extensions

Depending on the accretion geometry, radiation from the post-shock zone may be reprocessed in the pre-shock accretion flow. This will form a photoionised radiative precursor, sufficiently hot to emit in C III and even O VI lines. The emitting region however is located close to the shock, where the material is moving at close to free-fall speed, and emission is redshifted by about 500 km s^{-1}. Lamzin (2003) performed detailed 3-level-atom calculations supporting the above considerations with numerical simulations. He found that the total emission should be observed as two distinct peaks, one close to free-fall velocity about 500 km s^{-1} and the other formed post-shock. Only if the line of sight is perpendicular to the direction of flow these two peaks can coincide, but close to the rest wavelength. For TW Hya, which is seen close to pole-on, this would require accretion in an equatorial layer.

Figure 7 shows that in principle a large turbulent broadening could explain the observed line width, but it requires turbulent velocities larger than the post-shock bulk velocity. Nevertheless other plasma processes such as magnetic waves may supply the required turbulence.

The line widths could be explained if the emission originates in the funnels well before entering the radiative precursor, in a region high above the stellar surface. A single feature corotating with the star would be observed moving through the line profile, as the star rotates, and a combination of many emission regions may result in a very broad line. In this case an efficient and currently unknown heating mechanism in the accretion funnels is needed to form the hot ions. The resolution of the current X-ray telescopes *Chandra* and *XMM-Newton* is insufficient to detect line broadening less than about 1000 km s^{-1} or line shifts less than a few 100 km s^{-1}. We are therefore unable to compare our line-profile measurements with those for hotter ion lines, which are most likely accretion-dominated.

5.4. Turbulence in boundary layers

Turbulence is an obvious way to generate significant line widths. Turbulent flows convert bulk kinetic motion into heat and vorticity and a flow along a boundary layer would be an obvious origin of turbulence. If, alternatively, accretion proceeds in an equatorial boundary layer, the difference in velocity is given by the difference between the stellar rotation $v_{\rm rot}$, and the velocity of material accreting close to the Keplerian velocity at the stellar surface $v_{\rm Kepler} = \sqrt{\frac{GM_*}{R_*}} \approx 440$ km s^{-1}, where G is the gravitational constant, and the stellar parameters radius R_* and mass M_* for the example of TW Hya are taken from Webb et al. (1999). The equatorial velocity can be estimated from $v_{\rm eq} = \frac{v \sin i}{\sin i} \approx 40$ km s^{-1}.

In order to estimate the dissipated energy, we use the turbulent Crocco-Busemann relation, which is valid for turbulent flow along a surface. We follow the treatment by White (1991) and neglect the initial temperature of the infalling flow, since the accretion disk is cool, and the photospheric temperature. We obtain a relation between temperature in the turbulent layer $T_{\rm turb}$ and velocity u of flow:

$$T_{\rm turb}(u) = \frac{u}{2c_{\rm p}}(\Delta v - u)\,, \tag{3}$$

where $\Delta v = v_{\rm Kepler} - v_{\rm eq}$, u is the velocity of the gas relative to the photosphere and $c_{\rm p}$ has the usual thermodynamic meaning as specific heat at constant pressure. For an ideal gas, Eq. (3) simplifies to $T_{\rm turb} = 2.3 \times 10^5\ {\rm K} \frac{\Delta v^2}{(100 {\rm km s^{-1}})^2}(\tilde{u} - \tilde{u}^2)$, with $\tilde{u} = \frac{u}{\Delta v}$, so the maximum temperature is reached where the infalling gas has slowed down by $\frac{\Delta v}{2}$. For $\Delta v \approx 400$ km s^{-1}, the maximum temperature is 9×10^5 K and 2.3×10^5 K for half the Keplerian velocity. In the example of TW Hya, in both scenarios the formation temperature of O VI is reached. Because the line-of-sight is perpendicular to equatorial accretion, the peak of the velocities should appear close to the rest wavelength with a line width comparable to the turbulent velocity. In this scenario, it is clearly difficult to explain the shift of the line centre, but this process may contribute to the emission responsible for a broad component, especially in stars with with only slightly shifted emission such as DF Tau, V4046 Sgr and TWA 5 or in TW Hya during the *GHRS* and *STIS* observations. For TWA 5, the scenario furthermore explains how accretion, as supported by a measured Hα EW of 13.4 Å, could proceed. This is in spite of the fact that the X-ray radiation originates in a low-density region, probably a corona, in contrast to that expected in a scenario of magnetically-funnelled accretion in hot spots.

5.5. Red-shifted emission

All UV observations of TW Hya show consistently red-shifted lines. The only possible explanation are matter flows onto the stellar surface because the far side of the star is blocked from view by the star itself. On the other hand, as argued above, the absence of a double-peaked profile with pre- and post-shock emission implies that accretion spots are unlikely to explain their origin. We therefore now discuss a contribution from the accretion funnels. Three-dimensional MHD simulations of Romanova et al. (2004) give accretion spots with inhomogeneous velocity profiles, where the flow speed is close to free-fall at the spot centre and much slower at the edges. Their simulations use ideal MHD equations and do not take into account the heating by turbulence caused by the difference in velocity within the accretion streams. In general the discussion in Sect. 5.4 applies with velocity differences of the order of half the Keplerian velocity, so significant turbulent heating could arise in the funnels themselves, if turbulence is not suppressed by the strong magnetic fields. Further modelling and clarification of the accretion geometry is required to check the resulting emission measures. Figure 7 shows that the shock, given some turbulent broadening in the post-shock zone, can account for a significant proportion of the observed emission in accordance with our post-shock cooling zone simulations.

Interestingly, in MS stars lines red-shifted by a few km s^{-1} are also observed (Ayres & Linsky 1980; Ayres et al. 1983), so there has to be an emission mechanism unrelated to accretion, usually attributed to downflows in the stellar transition region. This phenomenon may occur in CTTS as well.

5.6. Other emission origins?

Emission in the disk surrounding the star may in principle explain broad M-shaped lines, but the temperature at the disk surface is only a few thousand K (Herczeg et al. 2004). Neither C III nor O VI forms there.

Also, for e.g. TW Hya, where exceptionally broad lines are detected, the projected velocity of the disk at the inner disk edge is only ≈20 km s^{-1}. We observe no variation in the peak shift between the two observations of TW Hya, so it seems unlikely that it is produced by a single feature moving with the rotating disk.

If the lines originate in an extended chromosphere, from the ratio of equatorial velocity and line width we can estimate the height of the emitting structures and find, using the values for O VI 1032 Å from Table 4, that the emission is placed at the stellar surface for T Tau and at about three stellar radii for RU Lup, V4046 Sgr, GM Aur and TW Hya. This can only explain line shifts if we assume upflowing material for RU Lup and downflows for TW Hya stable over all exposures, which seems unlikely.

5.7. Variability

In theoretical simulations accretion, jets and wind generation are highly variable processes (von Rekowski & Brandenburg 2006). Comparing the fluxes of TW Hya in the multiplet C III 1175 Å , in observations acquired using *FUSE* and *HST*, we find that the flux decreases by approximately one quarter over three years. In contrast, a flux difference of over a factor of five is measured for RU Lup observations (Herczeg et al. 2005). For TW Hya, there are also *FUSE* observations separated by several years. Unfortunately, the earlier observations are very short and of low SNR. Comparing the *GHRS* and *STIS* observations, separated by 4–8 years, the observed line width and shifts appear to be roughly consistent. We next considered correlations between these observations and FUSE data. Excluding the C III 1175 Å multiplet, for which a line-profile analysis is impossible, there are no lines that are in common between the two sets of data. It is expected however, that lines of Si IV, C IV and N V will originate in emission-line regions for which C III and O VI emission is detected. In all cases, the line widths fall in the range 100–300 km s^{-1}, and for RU Lup, T Tau and DF Tau the lines are all consistently blueshifted, but in the *HST* observations to a much lesser extent than in the *FUSE* data, conversely, the TW Hya lines are more redshifted in the *FUSE* data. This hints at a strong variability of CTTS, where the dominant UV emission mechanism may change between winds and accretion.

Longer monitoring is required to test if the difference between the objects in our sample is due to different phases of activity and accretion rate or if there are other fundamental differences. This is similar to the situation in X-rays, where several luminosity changes are observed, most likely due to coronal flaring on the time scale of hours (Kastner et al. 2002; Günther et al. 2006), but the evidence is inconclusive and some variability might also be due to time-variable accretion rates.

6. Summary

We have presented the hot ion lines originating from C III and O VI in all available CTTS spectra observed with *FUSE*. The fitted centroids range from about −170 km s^{-1} to +100 km s^{-1} and the shifts of the C III 977 Å line and the O VI 1032 Å and 1038 Å doublet are consistent. Most, if not all, lines are super-rotationally broadened. The blue-shifted lines could originate in a stellar outflow, maybe a jet; the red-shifted lines are incompatible with current models of magnetospheric accretion. The presence of boundary layers, winds and extended chromospheres is inconsistent with the observed line profiles.

Furthermore, the absorbing column densities observed in X-rays are incompatible with the optical reddening measured assuming a standard gas-to-dust ratio and interstellar extinction law. This situation holds for the most heavily-veiled objects AA Tau, DF Tau, T Tau, SU Aur and, although for lower absolute values of reddening, RU Lup. In cases where data are available from both UV and X-ray, the corresponding objects demonstrate blue-shifted emission in the *FUSE* observations. We interpret this as a sign of a dust-free absorber, which may consist of shock-heated jet material. In the ratio between the O VII luminosity and the O VI luminosity, all CTTS display a clear excess of soft X-ray emission in the O VII lines. Together with X-ray results, this illustrates that the signatures of a hot accretion spot are most evident in the temperature range 1–2 MK.

Acknowledgements. We thank G. Herczeg and C. Johns-Krull, the referee, for their competent remarks, especially on the *FUSE* wavelength calibration. The data presented in this paper were obtained from the Multimission Archive at the Space Telescope Science Institute (MAST). STScI is operated by the Association of Universities for Research in Astronomy, Inc., under NASA contract NAS5-26555. Support for MAST for non-HST data is provided by the NASA Office of Space Science via grant NAG5-7584 and by other grants and contracts.
CHIANTI is a collaborative project involving the NRL (USA), RAL (UK), MSSL (UK), the Universities of Florence (Italy) and Cambridge (UK), and George Mason University (USA).
H.M.G. acknowledges support from DLR under 50OR0105.

References

Ake, T. B., Dupree, A. K., Young, P. R., et al. 2000, ApJ, 538, L87

Alencar, S. H. P., & Basri, G. 2000, AJ, 119, 1881
Alencar, S. H. P., & Batalha, C. 2002, ApJ, 571, 378
Ardila, D. R., Basri, G., Walter, F. M., Valenti, J. A., & Johns-Krull, C. M. 2002a, ApJ, 566, 1100
Ardila, D. R., Basri, G., Walter, F. M., Valenti, J. A., & Johns-Krull, C. M. 2002b, ApJ, 567, 1013
Argiroffi, C., Maggio, A., & Peres, G. 2007, A&A, 465, L5
Argiroffi, C., Maggio, A., Peres, G., Stelzer, B., & Neuhäuser, R. 2005, A&A, 439, 1149
Ayres, T. R. 2005, in 13th Cambridge Workshop on Cool Stars, Stellar Systems and the Sun, ed. F. Favata, et al., ESA SP-560, 419
Ayres, T. R., & Linsky, J. L. 1980, ApJ, 241, 279
Ayres, T. R., Stencel, R. E., Linsky, J. L., et al. 1983, ApJ, 274, 801
Bally, J., Reipurth, B., & Davis, C. J. 2007, in Protostars and Planets V, ed. B. Reipurth, D. Jewitt, & K. Keil, 215
Balucinska-Church, M., & McCammon, D. 1992, ApJ, 400, 699
Basri, G., & Batalha, C. 1990, ApJ, 363, 654
Bergin, E., Calvet, N., Sitko, M. L., et al. 2004, ApJ, 614, L133
Beristain, G., Edwards, S., & Kwan, J. 2001, ApJ, 551, 1037
Bertout, C., & Genova, F. 2006, A&A, 460, 499
Bloemen, J. B. G. M. 1987, ApJ, 322, 694
Bouvier, J., Bertout, C., Benz, W., & Mayor, M. 1986, A&A, 165, 110
Bouvier, J., Chelli, A., Allain, S., et al. 1999, A&A, 349, 619
Calvet, N., & Gullbring, E. 1998, ApJ, 509, 802
Cardelli, J. A., Clayton, G. C., & Mathis, J. S. 1989, ApJ, 345, 245
Chen, W. P., Simon, M., Longmore, A. J., Howell, R. R., & Benson, J. A. 1990, ApJ, 357, 224
Coffey, D., Bacciotti, F., Woitas, J., Ray, T. P., & Eislöffel, J. 2004, ApJ, 604, 758
Cohen, M., & Kuhi, L. V. 1979, ApJS, 41, 743
Dere, K. P., Landi, E., Mason, H. E., Fossi, B. C. M., & Young, P. R. 1998, in The Scientific Impact of the Goddard High Resolution Spectrograph, ASP Conf. Ser., 143, 390
Dixon, W. V., Sahnow, D. J., Barrett, P. E., et al. 2007, PASP, 119, 527
Dupree, A. K., Brickhouse, N. S., Smith, G. H., & Strader, J. 2005a, ApJ, 625, L131
Dupree, A. K., Lobel, A., Young, P. R., et al. 2005b, ApJ, 622, 629
Edwards, S., Fischer, W., Hillenbrand, L., & Kwan, J. 2006, ApJ, 646, 319
Eislöffel, J., & Mundt, R. 1998, AJ, 115, 1554
Eisner, J. A., Chiang, E. I., & Hillenbrand, L. A. 2006, ApJ, 637, L133
Errico, L., Lamzin, S. A., & Vittone, A. A. 2001, A&A, 377, 557
Feldman, P. D., Sahnow, D. J., Kruk, J. W., Murphy, E. M., & Moos, H. W. 2001, J. Geophys. Res., 106, 8119
Gómez de Castro, A. I., & Ferro-Fontán, C. 2005, MNRAS, 362, 569
Gregory, S. G., Jardine, M., Simpson, I., & Donati, J.-F. 2006, MNRAS, 371, 999
Güdel, M., & Telleschi, A. 2007, A&A, 474, L25
Güdel, M., Skinner, S. L., Briggs, K. R., et al. 2005, ApJ, 626, L53
Güdel, M., Skinner, S. L., Mel'Nikov, S. Y., et al. 2007, A&A, 468, 529
Günther, H. M., & Schmitt, J. H. M. M. 2007, Mem. Soc. Astron. Ital., 78, 359
Günther, H. M., Schmitt, J. H. M. M., Robrade, J., & Liefke, C. 2007, A&A, 466, 1111
Günther, H. M., Liefke, C., Schmitt, J. H. M. M., Robrade, J., & Ness, J.-U. 2006, A&A, 459, L29
Hartigan, P., Raymond, J., & Hartmann, L. 1987, ApJ, 316, 323
Hartmann, L., & Stauffer, J. R. 1989, AJ, 97, 873
Herczeg, G. J., Linsky, J. L., Valenti, J. A., Johns-Krull, C. M., & Wood, B. E. 2002, ApJ, 572, 310
Herczeg, G. J., Wood, B. E., Linsky, J. L., Valenti, J. A., & Johns-Krull, C. M. 2004, ApJ, 607, 369
Herczeg, G. J., Walter, F. M., Linsky, J. L., et al. 2005, AJ, 129, 2777
Herczeg, G. J., Linsky, J. L., Walter, F. M., Gahm, G. F., & Johns-Krull, C. M. 2006, ApJS, 165, 256
Hueso, R., & Guillot, T. 2005, A&A, 442, 703
Johns-Krull, C. M., & Herczeg, G. J. 2007, ApJ, 655, 345
Joy, A. H. 1949, ApJ, 110, 424
Kastner, J. H., Huenemoerder, D. P., Schulz, N. S., Canizares, C. R., & Weintraub, D. A. 2002, ApJ, 567, 434
Kenyon, S. J., & Hartmann, L. 1995, ApJS, 101, 117
Koenigl, A. 1991, ApJ, 370, L39
Koresko, C. D. 2000, ApJ, 531, L147
Lamzin, S. A. 1998, Astron. Rep., 42, 322
Lamzin, S. A. 2003, Astron. Rep., 47, 498
Lamzin, S. A., Bisnovatyi-Kogan, G. S., Errico, L., et al. 1996, A&A, 306, 877
Lamzin, S. A., Vittone, A. A., & Errico, L. 2001, Astron. Lett., 27, 313
Lamzin, S. A., Kravtsova, A. S., Romanova, M. M., & Batalha, C. 2004, Astron. Lett., 30, 413
Landi, E., Del Zanna, G., Young, P. R., et al. 2006, ApJS, 162, 261
Lavalley-Fouquet, C., Cabrit, S., & Dougados, C. 2000, A&A, 356, L41
Mamajek, E. E., Meyer, M. R., & Liebert, J. 2002, AJ, 124, 1670
Matt, S., Goodson, A. P., Winglee, R. M., & Böhm, K.-H. 2002, ApJ, 574, 232
Mazzotta, P., Mazzitelli, G., Colafrancesco, S., & Vittorio, N. 1998, A&AS, 133, 403
McCandliss, S. R. 2003, PASP, 115, 651
Metchev, S. A., Hillenbrand, L. A., & Meyer, M. R. 2004, ApJ, 600, 435
Mohanty, S., Jayawardhana, R., & Barrado y Navascués, D. 2003, ApJ, 593, L109
Muzerolle, J., Hartmann, L., & Calvet, N. 1998, AJ, 116, 2965
Muzerolle, J., Calvet, N., Briceño, C., Hartmann, L., & Hillenbrand, L. 2000, ApJ, 535, L47
Najita, J. R., Strom, S. E., & Muzerolle, J. 2007, MNRAS, 378, 369
Ness, J.-U., Güdel, M., Schmitt, J. H. M. M., Audard, M., & Telleschi, A. 2004, A&A, 427, 667
Pudritz, R. E., Ouyed, R., Fendt, C., & Brandenburg, A. 2007, in Protostars and Planets V, ed. B. Reipurth, D. Jewitt, & K. Keil, 277
Qi, C., Ho, P. T. P., Wilner, D. J., et al. 2004, ApJ, 616, L11
Quast, G. R., Torres, C. A. O., de La Reza, R., da Silva, L., & Mayor, M. 2000, in IAU Symp., 28P
Redfield, S., Linsky, J. L., Ake, T. B., et al. 2002, ApJ, 581, 626
Robrade, J., & Schmitt, J. H. M. M. 2006, A&A, 449, 737
Robrade, J., & Schmitt, J. H. M. M. 2007, A&A, 473, 229
Rodmann, J., Henning, T., Chandler, C. J., Mundy, L. G., & Wilner, D. J. 2006, A&A, 446, 211
Rodriguez, L. F. 1995, in Rev. Mex.e Astron. Astrofis. Conf. Ser., ed. S. Lizano, & J. M. Torrelles, 1
Romanova, M. M., Ustyugova, G. V., Koldoba, A. V., & Lovelace, R. V. E. 2004, ApJ, 610, 920
Saar, S. H., & Osten, R. A. 1997, MNRAS, 284, 803
Sallmen, S., Johns-Krull, C. M., Welsh, B., & Griffiths, N. 2000, in BAAS, 1482
Salyk, C., Blake, G. A., Boogert, A. C. A., & Brown, J. M. 2007, ApJ, 655, L105
Savage, B. D., & Mathis, J. S. 1979, ARA&A, 17, 73
Schaefer, G. H., Simon, M., Beck, T. L., Nelan, E., & Prato, L. 2006, AJ, 132, 2618
Schegerer, A., Wolf, S., Voshchinnikov, N. V., Przygodda, F., & Kessler-Silacci, J. E. 2006, A&A, 456, 535
Schmitt, J. H. M. M., & Robrade, J. 2007, A&A, 462, L41
Shu, F., Najita, J., Ostriker, E., et al. 1994, ApJ, 429, 781
Simon, M., Dutrey, A., & Guilloteau, S. 2000, ApJ, 545, 1034
Stelzer, B., & Schmitt, J. H. M. M. 2004, A&A, 418, 687
Stempels, H. C., & Gahm, G. F. 2004, A&A, 421, 1159
Stempels, H. C., & Piskunov, N. 2002, A&A, 391, 595
Stempels, H. C., Gahm, G. F., & Petrov, P. P. 2007, A&A, 461, 253
Strom, K. M., Strom, S. E., Edwards, S., Cabrit, S., & Skrutskie, M. F. 1989, AJ, 97, 1451
Takami, M., Bailey, J., Gledhill, T. M., Chrysostomou, A., & Hough, J. H. 2001, MNRAS, 323, 177
Telleschi, A., Güdel, M., Briggs, K. R., et al. 2007, A&A, 468, 541
Torres, G., Guenther, E. W., Marschall, L. A., et al. 2003, AJ, 125, 825
Uchida, K. I., Calvet, N., Hartmann, L., et al. 2004, ApJS, 154, 439
Uchida, Y., & Shibata, K. 1984, PASJ, 36, 105
Unruh, Y. C., Collier Cameron, A., & Guenther, E. 1998, MNRAS, 295, 781
Valenti, J. A., Johns-Krull, C. M., & Linsky, J. L. 2000, ApJS, 129, 399
van Langevelde, H. J., van Dishoeck, E. F., & Blake, G. A. 1994a, ApJ, 425, L45
van Langevelde, H. J., van Dishoeck, E. F., van der Werf, P. P., & Blake, G. A. 1994b, A&A, 287, L25
Vilhu, O., Gustafsson, B., & Edvardsson, B. 1987, ApJ, 320, 850
von Rekowski, B., & Brandenburg, A. 2006, Astron. Nachr., 327, 53
Vuong, M. H., Montmerle, T., Grosso, N., et al. 2003, A&A, 408, 581
Walter, F. M., Herczeg, G., Brown, A., et al. 2003, AJ, 126, 3076
Webb, R. A., Zuckerman, B., Platais, I., et al. 1999, ApJ, 512, L63
Weinberger, A. J., Becklin, E. E., Zuckerman, B., & Song, I. 2004, AJ, 127, 2246
White, F. M. 1991, Viscous fluid flow (New York: McGraw-Hill)
Wilkinson, E., Harper, G. M., Brown, A., & Herczeg, G. J. 2002, AJ, 124, 1077
Wood, B. E., Linsky, J. L., & Ayres, T. R. 1997, ApJ, 478, 745
Zel'Dovich, Y. B., & Raizer, Y. P. 1967, Physics of shock waves and high-temperature hydrodynamic phenomena (New York: Academic Press), ed. W. D. Hayes, & R. F. Probstein

Chapter 7

Revealing the fastest component of the DG Tau outflow through X-rays

H.M. Günther, S. P. Matt and Z.-Y. Li
Astronomy & Astrophysics, accepted

Astronomy & Astrophysics manuscript no. dgtau6
December 16, 2008

Revealing the fastest component of the DG Tau outflow through X-rays

H.M. Günther[1,2], S. P. Matt[2], and Z.-Y. Li[2]

[1] Hamburger Sternwarte, Universität Hamburg, Gojenbergsweg 112, 21029 Hamburg, Germany
e-mail: moritz.guenther@hs.uni-hamburg.de
[2] Department of Astronomy, University of Virginia, P.O. Box 400325, Charlottesville, VA 22904, USA

Received 2 September 2008 / Accepted 4 November 2008

ABSTRACT

Context. Some T Tauri stars show a peculiar X-ray spectrum that can be modelled by two components with different absorbing column densities.
Aims. We seek to explain the soft X-ray component in DG Tau, the best studied of these sources, with an outflow model, taking observations at other wavelengths into consideration.
Methods. We constrain the outflow properties through spectral fitting and employ simple semi-analytical formulae to describe properties of a shock wave that heats up the X-ray emitting region.
Results. The X-ray emission is consistent with its arising from the fastest and innermost component of the optically detected outflow. Only a small fraction of the total mass loss is required for this X-ray emitting component. Our favoured model requires shock velocities between 400 and 500 km s^{-1}. For a density $> 10^5$ cm^{-3} all dimensions of the shock cooling zone are only a few AU, so even in optical observations this cannot be resolved.
Conclusions. This X-ray emission mechanism in outflows may also operate in other, less absorbed T Tauri stars, in addition to corona and accretion spots.

Key words. stars: formation – stars: winds/outflows – stars: individual: DG Tau – stars: mass-loss

1. Introduction

Jets and outflows seem to be a natural consequence of disc accretion, as they are common phenomena in star formation. Jets are an especially active area of study at present. Their innermost region is particularly interesting because it arises from the deepest in the potential well and thus probes the conditions there, which cannot be resolved by direct imaging. This innermost region is crucial for our understanding of jet launching and collimation. We need to constrain the different theoretical models of stellar winds (Kwan & Tademaru 1988; Matt & Pudritz 2005), X-winds (Shu et al. 1994) and disc winds (Blandford & Payne 1982; Anderson et al. 2005) to produce reliable estimates of the associated angular momentum loss from the disc and possibly the star. This spin-down is needed to explain the slow rotation of accreting classical T Tauri stars (CTTS).

CTTS also have long been known as copious emitters of X-rays (Feigelson & Montmerle 1999), and we now recognise that multiple emission mechanisms contribute to the observed radiation. Studies of large statistical samples clearly show a coronal component, which occasionally breaks out in hard X-ray flares (Preibisch et al. 2005; Stelzer et al. 2007). Additionally a hot spot on the stellar surface heated by ongoing accretion contributes (Günther et al. 2007). It shows up in X-ray line ratios originating in high-density regions, much denser than any corona (Kastner et al. 2002; Stelzer & Schmitt 2004; Schmitt et al. 2005; Günther et al. 2006; Argiroffi et al. 2007). There is relatively recent evidence of X-rays from the outflows themselves, starting with HH 2 (Pravdo et al. 2001) and HH 154 (Favata et al. 2002; Bally et al. 2003; Favata et al. 2006). X-rays very likely trace the fastest shocks in the jets. The first spatially extended X-ray emission of a CTTS jet was found using *Chandra* by Güdel et al. (2005, 2008) in DG Tau. This star shows a spatially resolved, soft emission extending out to 5″. It is not compatible with a point source origin, and Güdel et al. (2008, hereafter GS08) model it by a combination of a linear source plus a Gaussian of ≈ 140 AU diameter at the maximum distance to the star. Also, Güdel et al. (2007) find unusual spectral shapes in some CTTS distinguishing these so-called TAX (two absorber X-ray) sources from most other CTTS. Their spectra can be fitted well with a highly absorbed hard component and a much less absorbed soft component. They suggest that the marginally resolved soft excess is emission from the base of the jet (see also Schneider & Schmitt 2008). In this paper we develop this picture further in order to use the X-rays as a probe of the innermost, fastest outflow and to constrain the jet's spatial extent and mass outflow rate. This idea is supported by the finding of Schneider & Schmitt (2008) that there is a small but significant spatial offset between the soft and the hard central components in DG Tau, so even the central component is marginally resolved.

We focus specifically on DG Tau, since the source is studied at many wavelengths, especially the stronger jet to the SW, but much less information is available for the fainter counter-jet to the NE. In the optical the jet has been imaged with *HST/STIS* several times, revealing not only jet rotation (Coffey et al. 2007), but also the presence of components with different velocities in the approaching

jet with up to 600 km s^{-1} (Bacciotti et al. 2000), after correcting for projection effects.

Based on analysis of forbidden lines, it was inferred that the jet density rapidly falls off with increasing distance from the star (Lavalley-Fouquet et al. 2000; Bacciotti et al. 2000). The jet extends to 0.5 pc as HH 702 (McGroarty et al. 2007), where shock-excited knots are clearly seen, but also closer to the star there has to be a heating source to sustain the jet emission. Heating by ambient shocks within the material itself is a good candidate. Takami et al. (2004) found a cool and slow molecular wind with an opening angle near 90 deg, which surrounds the faster and hotter atomic outflow (see also Beck et al. 2008).

Raga et al. (2001) presented a 3D hydrodynamical simulation of the DG Tau jet. They assume a sinusoidal velocity variation and precession. The precession broadens up the working surfaces in an otherwise well-collimated beam and produces several shocks where the faster material catches up with the previously ejected slower matter. In this model the density decreases naturally with the distance to the stellar source.

In this paper we examine the emission measure, column density and temperature of the X-ray emitting region through spectral fitting (Sect. 2) and interpret the soft component as a tracer of the fastest component of the outflow (Sect. 3). We then discuss constraints from other wavelength bands and their implication for the outflow origin in Sect. 4. We present our conclusions in Sect. 5 and give a short summary in Sect. 6.

2. X-ray observations

We rely on the X-ray data presented by GS08, consisting of a 40 ks *XMM-Newton* observation (ObsID 0203540201) and four *Chandra* exposures (ObsIDs 4487, 6409, 7247 and 7246), which sum up to 90 ks observation time. We retrieved this data from the archives, reduced it using standard SAS and CIAO tasks, and analyse it in XSPEC. Because of the low count rate we merge all available *Chandra* data. GS08 show that the error bars on the fitted values overlap between the four exposures for the soft component. The luminosity in the hard component varies by a factor of three, but the other parameters are compatible. Since we are most interested in modelling the soft component, variations in the luminosity and temperature of the hard component are not important here. We simultaneously fit the merged *Chandra* and the *XMM-Newton* data with two thermal components with individual absorption. We keep the parameters for *Chandra* and *XMM-Newton* coupled in the soft component and leave the temperature and normalisation between the hard components free, because it is observed to be much stronger in the *XMM-Newton* observation due to intrinsic variability. As an illustration we show the data recorded by the EPIC/PN camera which covers the broadest energy range in Fig. 1. As black and red/grey lines we show two fits to the soft components with different temperatures. The fits shown use solar abundances according to Grevesse & Sauval (1998).

Due to the low count numbers, the statistical uncertainties are large. In Fig. 1 the black line shows a model with kT = 0.3 keV and moderate absorption, very similar to that presented in GS08. However, a model with a much cooler temperature (kT = 0.08 keV), higher emission measure and larger absorbing column density reproduces the

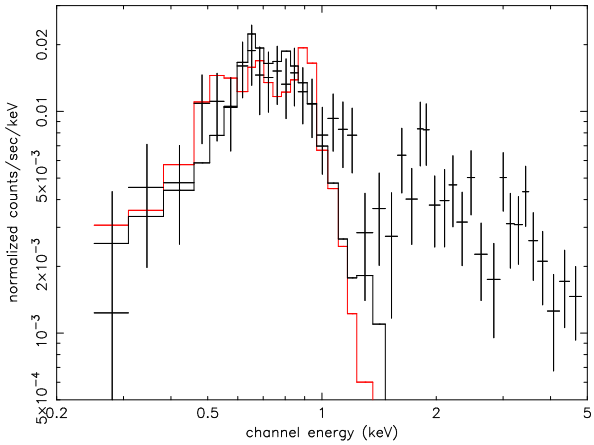

Fig. 1. *XMM-Newton* EPIC/PN data of DG Tau. Overplotted are the contributions by the soft component for two different scenarios: kT = 0.3 keV ($N_{\rm H} = 2.3 \times 10^{21}$ cm^{-2}; black line) and kT = 0.08 keV ($N_{\rm H} = 11 \times 10^{21}$ cm^{-2}; red/grey line).

data nearly as well, as illustrated by the red/grey line in the figure. Thus, for the soft component, there is an ambiguity that makes it difficult to precisely determine the temperature, emission measure, and absorption column.

To quantify this, we have run a grid of models, keeping all parameters for the hard component fixed and leaving the cool component's volume emission measure (VEM hereafter), temperature and absorption column density free. The resulting χ^2-distribution is shown in Fig. 2. At the 99.95 % confidence level the distribution ranges over ten orders of magnitude in emission measure and one order of magnitude in temperature, following a narrow valley in Temperature–VEM space. The most likely temperature region is 0.2-0.4 keV with a second region within the 99 % confidence contour around 0.08 keV. The secondary peak around 0.08 keV is caused mostly by *Chandra* data; it does not appear in a fit to the data from *XMM-Newton*, which is more sensitive to low energy X-rays than *Chandra*.

We verified that the position of this valley in χ^2-space does not change if the parameters of the hard component are left free. We fit the thermal emission with two APEC models. When using MEKAL, the minimum χ^2-valley is in the same place, but the absolute minimum χ^2 model is shifted to lower energies by up to 0.05 keV along the valley. We regard this as an estimate for the systematic uncertainty in the fit process.

Due to this and the ambiguity in fitting the temperature and VEM of the soft component, rather than taking the formal minimum χ^2 model, we consider a range of parameter space that is statistically allowed by the observations. Future observations will be needed to pin down more precise values. Thus, we fit a simple power-law to the minimum χ^2-valley of figure 2. This gives

$$\frac{\rm VEM}{10^{52}{\rm cm}^{-3}} \approx 0.45 \cdot \left(\frac{0.33\ {\rm keV}}{{\rm k}T}\right)^{5.5} . \quad (1)$$

The emission measure of the minimum χ^2-valley deviates less than a factor of 2 from equation (1) in the energy range 0.1-0.4 keV (Fig. 2). We will use this relationship in the following section.

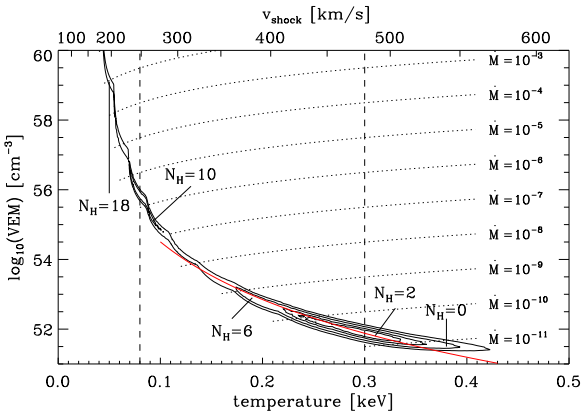

Fig. 2. This shows confidence contours (at 68 %, 90 %, 99 % and 99.95 % confidence level) fitting the VEM and the temperature of the soft component. The parameters in the hard component are held fixed. Assuming a simple shock model (see text for details) the shock velocity is given on the upper horizontal axis and mass loss rates in $M_\odot$ yr^{-1} are marked in dotted lines in the plot. For some models absorbing column densities N_H are given in units of 10^{21} cm^{-2}. The temperatures of the two models shown in Fig. 1 are marked with dashed lines. Our fit from Eq. 1 is indicated with a red/grey line.

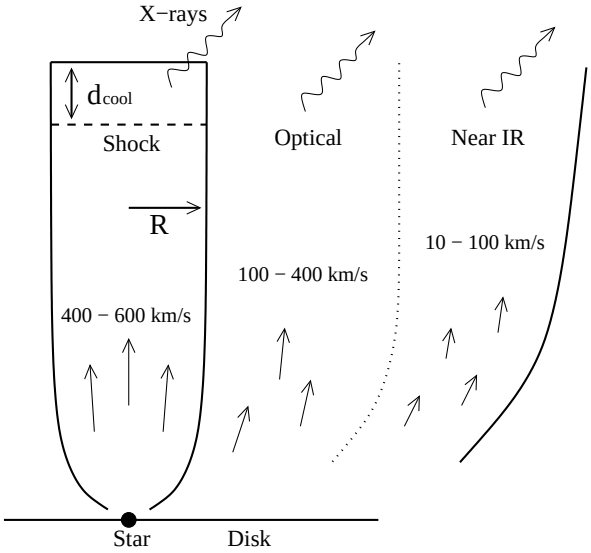

Fig. 3. Sketch of the geometry. The flow launched from the region closest to the star travels with the highest velocity, and internal shocks in the flow there can reach the highest temperatures.

To get a handle on the physical conditions in the emitting region further constraints are needed. The fact that the central component of the soft emission does not deviate significantly from a point source (Schneider & Schmitt 2008), gives an upper limit on the emitting volume and therefore a lower limit on the density. Its size should be less than 1″, corresponding to 140 AU at the distance of DG Tau. At the same time Schneider & Schmitt (2008) found the soft component to be significantly offset from the hard component at the stellar position by about 30 AU to the SW, the direction of the X-ray emitting, approaching jet.

3. A wind model

We use a simple, analytical model for the outflow. We discuss the observations giving rise to this model in detail in Sect. 4.3. Those observations indicate a collimated inner jet, which moves relatively fast. It is surrounded by slower and consecutively cooler components (e.g. Bacciotti et al. 2000, see Sect. 4.3 for more references). This situation – resembling the layers of an onion – is sketched in Fig. 3. The outer wind is launched from the disc whereas the origin of the inner jets could be either the inner disc region or the star itself. Disc winds are launched at temperatures of $\sim 10^4$ K or much less (Ardila et al. 2002; Herczeg et al. 2006). Stellar winds, even if launched at coronal temperatures, will cool adiabatically, and the radiative cooling time can also be very short (Matt & Pudritz 2007). Therefore, beyond several tens of stellar radii, we expect all components of the outflow to be too cool to emit X-rays. The outer layer contains molecular hydrogen and radiates predominantly in the IR; the more collimated and faster flows can be observed in the optical.

Raga et al. (2001) modelled successfully the optical observations with a jet model using a time-variable outflow speed. This gives rise to strong shocks, when faster gas catches up with previous ejecta. We assume that in the innermost outflow region the velocity of the flow is high enough to heat the post-shock material to X-ray emitting temperatures. The shock forms sufficiently far from the star that the flow is collimated.

Using the strong shock conditions we can transform the thermal energy kT, where k is Boltzmann's constant and T is the temperature, into the pre-shock velocity in the shock rest frame $v_{\rm shock}$:

$$\left(\frac{v_{\rm shock}}{500\ {\rm km\ s^{-1}}}\right)^2 \approx \frac{{\rm k}T}{0.33\ {\rm keV}}\ . \qquad (2)$$

This velocity is given on the upper horizontal axis in Fig. 2. We emphasise that, in the case of a travelling shock wave, the pre-shock gas velocity is the sum of $v_{\rm shock}$ and the motion of the shock front. Raga et al. (2002) provided a semi-analytical formulation for estimating the cooling length of gas heated in fast shocks ($\Delta v \gtrsim 200$ km/s). We checked this analytic relation with more detailed simulations of the shock cooling zone using our own code (Günther et al. 2007) and found that they agree within a factor of a few. Thus, for the semi-analytic treatment here, we will use the formula of Raga et al. (2002), which can be written

$$d_{\rm cool} \approx 20.9{\rm AU}\left(\frac{10^5{\rm cm^{-3}}}{n_0}\right)\left(\frac{v_{\rm shock}}{500\ {\rm km\ s^{-1}}}\right)^{4.5}, \qquad (3)$$

where n_0 is the pre-shock particle number density, equal to a quarter of the post-shock number density n in the strong shock approximation.

We assume an idealised cylindrical geometry for the post-shock flow, where the length of the cylinder is $d_{\rm cool}$. The mass flow rate $\dot{M}_{\rm shock}$ through the shock front with area A is then given by

$$\dot{M}_{\rm shock} = A v_{\rm shock} \rho_0, \qquad (4)$$

where $\rho_0 = \mu m_{\rm H} n_{\rm ion_0}$ is the pre-shock mass density of the flow, $n_{\rm ion_0}$ is the initial number density of heavy particles, i.e. atoms and ions, μ the mean relative ion particle weight, and $m_{\rm H}$ the mass of hydrogen. Assuming solar abundances, we adopt $\mu = 1.26$. It is worth noting that $\dot{M}_{\rm shock}$ is less than the total mass loss rate in the flow, since $v_{\rm shock}$ is measured in the rest frame of the shock, and shocks in these systems are observed to travel at speeds of tens to hundreds of km s^{-1}.

The area of the shock can be determined from

$$A = \pi R^2 = \frac{\rm Volume}{d_{\rm cool}} = \frac{VEM}{n_{\rm e} n_{\rm ion} d_{\rm cool}}, \quad (5)$$

where $n_{\rm e}$ and $n_{\rm ion}$ are the post-shock electron and ion number density. Combing Eqs. 2–5, and assuming $n_{\rm ion} = 4n_{\rm ion_0} = 0.83 n_{\rm e}$, the mass flow rate can be written

$$\dot{M}_{\rm shock} \approx 2.7 \cdot 10^{-11} \frac{M_\odot}{\rm yr} \left(\frac{VEM}{10^{52}\ {\rm cm}^{-3}}\right) \left(\frac{0.33\ {\rm keV}}{{\rm k}T}\right)^{1.75} \quad (6)$$

It is convenient that, by adopting a simple formula for the cooling length (Eq. 3) and a simple shock geometry, the determination of the mass loss rate is independent of the density of the flow.

We can now apply this specifically to the soft X-ray component of DG Tau. By combining the observed relationship of Eq. 1 with Eq. 6, one obtains

$$\dot{M}_{\rm shock} \approx 1.2 \times 10^{-11} \frac{M_\odot}{\rm yr} \left(\frac{0.33\ {\rm keV}}{{\rm k}T}\right)^{7.25}, \quad (7)$$

or, using equation (2),

$$\dot{M}_{\rm shock} \approx 1.2 \times 10^{-11} \frac{M_\odot}{\rm yr} \left(\frac{500\ {\rm km\ s^{-1}}}{v_{\rm shock}}\right)^{14.5}. \quad (8)$$

These formulae indicate that the mass loss rate required to explain the observed soft X-rays has a very steep dependence on the observed temperature. It is clear that a better determination of the mass loss rate requires a more precise temperature measurement. In Fig. 2 lines of constant mass loss rate are marked as dotted lines according to Eq. 6. Over the full length of the confidence contour the mass loss varies by ten orders of magnitude.

We now look at the physical size of the shock region, R, which is the radius of the base of the emitting cylinder of shocked gas. From Eqs. (2), (3) and (5), we can solve for the radius (in AU),

$$R \approx 0.97 \left(\frac{10^5 {\rm cm}^{-3}}{n}\right)^{0.5} \left(\frac{VEM}{10^{52}\ {\rm cm}^{-3}}\right)^{0.5} \left(\frac{0.33{\rm keV}}{{\rm k}T}\right)^{1.125} \quad (9)$$

and using the observed relationship for DG Tau (Eq. 1),

$$R \approx 0.65\ {\rm AU} \left(\frac{10^5 {\rm cm}^{-3}}{n}\right)^{0.5} \left(\frac{0.33{\rm keV}}{{\rm k}T}\right)^{3.875}. \quad (10)$$

In Fig. 4 the confidence contours for the lower mass loss rates are shown as functions of the radius of the shock at the cylinder base and the cooling length assuming a density of $n_{\rm ion} = 10^5$ cm^{-3} as motivated from the optical observations. For other densites the scalings are $R \sim \sqrt{\frac{1}{n}}$ (Eq. 9) and $d_{\rm cool} \sim \frac{1}{n}$ (Eq. 3).

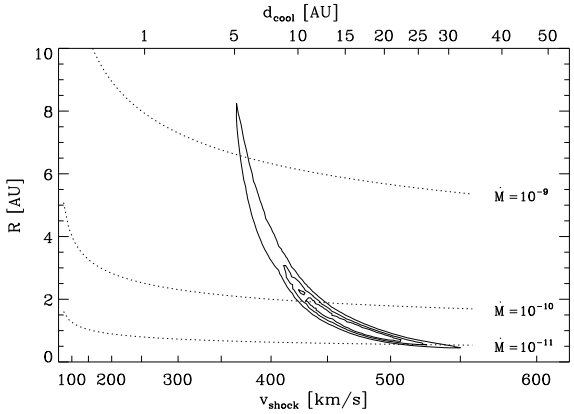

Fig. 4. Confidence contours (at 68 %, 90 % and 99 % confidence level) are shown for the parameters radius R and shock velocity $v_{\rm shock}$ for the case of a cylindrical cooling zone at a fixed density of $n = 10^5$ cm^{-3}. Dotted lines mark the mass loss rates in M$_\odot$ yr^{-1}.

4. Discussion

In this section we will use the formulas and conditions derived above to place limits on the physical mechanism producing the observed X-ray radiation.

4.1. Elemental abundance

The signal-to-noise ratio is not sufficient to fit elemental abundances, so we performed additional fits with the abundances found by Scelsi et al. (2007) for the Taurus molecular cloud. As usual there is a strong degeneracy between emission measure and metallicity. On average reduced abundances can be compensated for by a larger emission measure. Changes in the composition, that is particularly the Ne/O and Ne/Fe ratio, lead to different thermal structures. The confidence contours for fits with the abundances from Scelsi et al. (2007) follow the same valley in χ^2-space, but are displaced about 0.07 keV to higher energies. Models below 0.27 keV are excluded on the 99% confidence level.

It is not clear, however, if the coronal abundance is applicable to the jet, since the launching region of the X-ray emitting, fast jet component is unknown.

4.2. Limits on the size of the shock

Figure 2 shows two distinct regions of the parameter space within the 99% confidence level. That region in the upper left corner corresponds to a scenario of a large emission measure, which is heavily absorbed. The temperature is only around 0.08 keV and therefore the $v_{\rm shock} \approx 250$ km s^{-1}. As an upper limit we assume a density of 10^5 cm^{-3} (see next section). The cooling length according to Eq. 3 should be about 1 AU. In a simple cylindrical geometry the volume emission measure, transformed to a cylindrical radius with Eq. 9, requires a base shock with a radius of 1000 AU, but this would appear as an extended source, which is not observed for the central component (GS08, Schneider & Schmitt 2008). Only a density above

10^7 cm^{-3} could push all shock dimensions below ≈ 100 AU, so they appear as point source in the X-ray observation.

We deem this unreasonably high, also the low energy region is excluded in fits to the *XMM-Newton* data alone or in models with different – but reasonable – abundances, so we concentrate on the less absorbed case with a higher $v_{\rm shock}$ in Fig. 4. This parameter region can be realised with emission from the inner component of the jet only.

4.3. Limits placed by other observations

Observations with the *HST* allow to spatially resolve the outflow of DG Tau far below 1″ from the central source. The forbidden optical lines observed place density constraints. Bacciotti et al. (2000) conducted seven exposures with a long slit parallel to DG Tau's outflow in Hα and forbidden optical lines. They analyse the line shift within 0.″5 from the star and find that the faster moving gas is more confined towards the central axis. The emission of gas faster than 200 km s^{-1} is mostly confined to the inner slit, corresponding to a cylinder of radius 15 AU or less. Comparison of intensity maps in [O I], [N II] and [S II] leads them to conclude that the number density in the fast gas is higher than 10^4 cm^{-3} (the line ratios are not sensitive to densities above this value). The lower velocity emission occupies a larger area and originates in regions of lower densities of the order $10^3 - 10^4$ cm^{-3}. So, the inner, dense and fast components seem to be surrounded by slower and less dense outflows, maybe continuously down to a cool wind observed in H_2 with an opening angle of 90°(Takami et al. 2004). Consistent density estimates of $10^5 - 10^6$ cm^{-3} at distances less than 0.″5, deprojected to ≈ 100 AU, were obtained by Lavalley-Fouquet et al. (2000). Strictly speaking, their line ratios give only lower limits on the density for the fastest innermost components, too, but in any case the outer layers do not contribute significantly to the X-ray radiation.

From the total line intensity Lavalley et al. (1997) estimate a total mass loss rate of $6.5 \cdot 10^{-6}$ M$_\odot$ yr^{-1} if the gas is heated by shocks. With somewhat similar assumption Hartigan et al. (1995) obtain $3 \cdot 10^{-7}$ M$_\odot$ yr^{-1}. At a distance of 1.″2 from the central source Lavalley-Fouquet et al. (2000) estimate a mass loss rate of $1.4 \cdot 10^{-8}$ M$_\odot$ yr^{-1}. This evidence again favours the lower corner in Fig. 2, shown in more detail in Fig. 4.

In optical and IR line emission is detected blue-shifted up to deprojected velocities of 600 km s^{-1} (Lavalley-Fouquet et al. 2000; Bacciotti et al. 2000; Pyo et al. 2003). An analysis of data covering more than a decade by Pyo et al. (2003) indicates that the knots in the outflow move with a common proper motion of 0.″28 yr^{-1}, which translates into a deprojected velocity of 300 km s^{-1}.

4.4. The shocked gas component

As shown in Sect. 4.2 the X-ray emission is unlikely to originate in the slowly moving components of the outflow. This leaves the innermost component as the probable emission origin. Unrealistically high densities are needed to produce an emission measure of 10^{56} cm^{-3} for low shock speeds, so we favour a scenario where a strong shock with $v_{\rm shock} > 400$ km s^{-1} heats up a relatively small component of the jet. In this case the emission measure is much smaller, so the required mass flux to power this emission is several orders of magnitude smaller than the total mass flux observed in the optical. The dotted lines in Fig. 4 show the mass loss depending on $v_{\rm shock}$. Taking into account the observed proper motion of the knots, the gas velocities of e.g. Bacciotti et al. (2000) are too low to explain the X-ray spectrum. Because less than 10^{-4} of the total flow has to reach the highest velocity to produce the X-rays, this small component was possibly not detected in the optical observations. In scenarios with standing (collimation shock) instead of travelling shock waves the innermost component is fast enough to explain the observed emission easily.

After passing through the X-ray shock the material quickly radiates away its energy and cools down. Figure 4 shows all dimensions, the cooling length and the radius of the cylinder, to be small, therefore, they are not expected to be resolved in the *HST* observations. The X-ray emitting shock is only a small disturbance and within a few AU the material has cooled down again to match the temperatures of the surrounding gas. The shocks we discuss here cannot be resolved in images directly, so only a spectral analysis can help to further refine the model.

4.5. Formation of the shock front

Although the *Chandra* observations are separated by nearly two years, no evidence of motion has been detected (Schneider & Schmitt 2008), but given the size of the error circles a velocity $v_{\rm front}$ of the shock front of 100 km s^{-1} in the stellar rest frame cannot be excluded. In this case the wind mass loss rate $\dot{M}_{\rm wind}$ has to be calculated using the sum of $v_{\rm front}$ and $v_{\rm shock}$:

$$\dot{M}_{\rm wind} = \frac{v_{\rm front} + v_{\rm shock}}{v_{\rm shock}} \dot{M}_{\rm shock} \qquad (11)$$

If these knots represent internal working surfaces the associated $v_{\rm shock}$ is the difference between the gas motion and the proper motion of about 300 km s^{-1} for the knots. This by itself is not sufficient to power X-ray emission in the high temperature regime of Fig. 2. The knots seem to be launched irregularly, and the later *Chandra* observations could possibly probe a different knot than the earlier observations. A relatively slow shock speed of 400 km s^{-1} corresponding to a total mass loss rate of roughly 3×10^{-10} M$_\odot$ yr^{-1} (Fig. 4) is then just compatible with the highest optically detected outflow velocities. One more scenario can be postulated: Instead of a single (stationary or moving) shock front a higher number of small internal shocks could produce the same X-ray signature. Each of these "shocklets" would not show up in the optical observations, because radius and cooling lengths were far below the current resolution limit. This requires a clumpy outflow, where the jet contains a higher number of little knots surrounded by the optically detected fast wind. Our calculated shock area and cooling volume then represents the sum of all individual shocks. This argument is also valid, if the matter passes through multiple shock fronts and is reheated several times. The calculated mass flux rate still represents the summed flow of matter through all shock fronts, but it needs to be divided by the number of shocks to obtain the mass loss rate from the star. The optical observations discussed in Sect. 4.3 do not resolve the postulated X-ray shock front, but the optically resolved shock fronts seem to emerge separated by 150 AU (A1 and A2 in Bacciotti et al. (2000)), so it appears reasonable that the

X-rays may originate in a single shock front within 50 AU of the central star.

From our modelling there is no clear distinction between a stationary emission region as provided by a collimation shock or a moving knot. Only further observations with a longer time baseline can clarify this point. This is possible well within *Chandra*'s lifetime.

4.6. The outflow origin

The X-rays originate in the innermost and fastest component, which may originate from the innermost part of the disc or from the star itself. Matt & Pudritz (2007) showed that a T Tauri stellar wind with $\dot{M}_{\rm wind} \gtrsim 10^{-11}$ M$_\odot$ yr^{-1} cannot be coronally driven, but Alfvén wave driving may be possible (Cranmer 2008). The spin rate of DG Tau makes centrifugal launching of a stellar wind unlikely, whereas the outer layers with lower flow velocities are most likely centrifugally launched from the inner disc regions (Bacciotti et al. 2002; Anderson et al. 2003).

4.7. Relation to extended X-ray jet of DG Tau

The material heats up while passing through the shock front and we could show that the cooling length is very small compared to the spatial extend of the jet. While cooling, the jet looses energy, so the strength of the shock fronts decreases, their velocity jump diminishes with time. In their paper de Colle & Raga (2006) show this in magneto-hydrodynamical models with a time variable ejection velocity leading to travelling shock fronts. Additionally, according to the optical observations, the density decreases with the distance from the star. Therefore later heating events are less luminous, so the resolved source at $5''$ is weaker. Although the resolved shock is a spatially extended source, this does not necessarily require multiple heating events between $2''$ and $5''$, because the cooling length increases dramatically for low densities (GS08).

If the cause of the shock is a collision with slower, previously ejected matter we can expect this to happen more than once. In this picture the knot of X-ray emission at $5''$ is caused by matter catching up with an older ejection event. GS08 convincingly show that knots even further out are far too faint in X-rays to be detected.

5. Conclusion

The soft X-ray emission of DG Tau is consistent with our model of a shock in the outflow. The cause of the shock is not yet clear, but future observations can reveal if the position of the shock front is stationary. In this case it is likely caused by the collimation of the wind into the jet. If, on the other hand, the shock front moves, then we can take this as indication that the outflow ejection velocity is highly variable. In both cases only the fastest components of the optically detected outflow provide sufficient energy to power the X-ray emission. Possible future grating observations could greatly improve our estimate of the temperature in the emitting region and narrow down the range of possible shock velocities and therefore – via Fig. 4 – the mass loss rate.

DG Tau is an exceptional CTTS in the sense that its central component is so much absorbed that the origin of the soft emission cannot coincide with the star. This makes it an ideal case to search for alternative origins and our simple model successfully reproduces the observation. On other CTTS, most notably TW Hya, detailed models of an accretion shock explain the X-rays production very well (Günther et al. 2007). It seems possible, that TW Hya also has a weak contribution from wind shocks to its emission, but its outflows are much weaker than those of DG Tau, so the X-rays would be submerged in the stellar emission. Next to accretion and coronal activity the wind shocks, as discussed in this article, may hold as the third emission mechanism of soft X-rays, although it is difficult to disentangle the contributions except in special cases.

6. Summary

In the X-ray spectrum of DG Tau there is a spatially only marginally resolved soft component. Because no grating information is available, the temperature is only poorly constrained and plasma models with a wide range of temperatures can reproduce the observations. The absorbing column density is negligible in the case of plasma with a thermal energy of k$T = 0.4$ keV and rises to $N_{\rm H} > 10^{22}$ cm^{-2} for k$T = 0.1$ keV. For this second scenario the fitted emission measure would be several orders of magnitude higher. We reject this solution because it is not stable to small changes of the fit parameters and requires physically unreasonable values for the density in the shock region.

The emission can be explained by a shock and its corresponding cooling zone in the innermost and fastest component of the optically detected outflow. For densities $> 10^5$ cm^{-3} this is consistent with all available optical observations. Compared to the larger structures seen in the forbidden optical lines, this X-ray cooling zone could be a relatively thin layer. Only a small fraction of the total mass loss is needed in the innermost layer in order to produce the observed luminosity.

Acknowledgements. HMG acknowledges support from DLR under 50OR0105 and the Studienstiftung des deutschen Volkes. He thanks the University of Virginia for hosting him while this work was done. SPM is supported by the University of Virginia through a Levinson/VITA Fellowship, partially funded by the Frank Levinson Family Foundation through the Peninsula Community Foundation. ZYL is supported in part by AST-030768 and NAG5-12102. This research is based on observations obtained with XMM-Newton, an ESA science mission and Chandra, a NASA science mission.

References

Anderson, J. M., Li, Z.-Y., Krasnopolsky, R., & Blandford, R. D. 2003, ApJ, 590, L107
Anderson, J. M., Li, Z.-Y., Krasnopolsky, R., & Blandford, R. D. 2005, ApJ, 630, 945
Ardila, D. R., Basri, G., Walter, F. M., Valenti, J. A., & Johns-Krull, C. M. 2002, ApJ, 566, 1100
Argiroffi, C., Maggio, A., & Peres, G. 2007, A&A, 465, L5
Bacciotti, F., Mundt, R., Ray, T. P., et al. 2000, ApJ, 537, L49
Bacciotti, F., Ray, T. P., Mundt, R., Eislöffel, J., & Solf, J. 2002, ApJ, 576, 222
Bally, J., Feigelson, E., & Reipurth, B. 2003, ApJ, 584, 843
Beck, T. L., McGregor, P. J., Takami, M., & Pyo, T.-S. 2008, ApJ, 676, 472
Blandford, R. D. & Payne, D. G. 1982, MNRAS, 199, 883
Coffey, D., Bacciotti, F., Ray, T. P., Eislöffel, J., & Woitas, J. 2007, ApJ, 663, 350
Cranmer, S. R. 2008, ApJ, 689, in press
de Colle, F. & Raga, A. C. 2006, A&A, 449, 1061
Favata, F., Bonito, R., Micela, G., et al. 2006, A&A, 450, L17

Favata, F., Fridlund, C. V. M., Micela, G., Sciortino, S., & Kaas, A. A. 2002, A&A, 386, 204
Feigelson, E. D. & Montmerle, T. 1999, ARA&A, 37, 363
Grevesse, N. & Sauval, A. J. 1998, Space Science Reviews, 85, 161
Güdel, M., Skinner, S. L., Audard, M., Briggs, K. R., & Cabrit, S. 2008, A&A, 478, 797
Güdel, M., Skinner, S. L., Briggs, K. R., et al. 2005, ApJ, 626, L53
Güdel, M., Telleschi, A., Audard, M., et al. 2007, A&A, 468, 515
Günther, H. M., Liefke, C., Schmitt, J. H. M. M., Robrade, J., & Ness, J.-U. 2006, A&A, 459, L29
Günther, H. M., Schmitt, J. H. M. M., Robrade, J., & Liefke, C. 2007, A&A, 466, 1111
Hartigan, P., Edwards, S., & Ghandour, L. 1995, ApJ, 452, 736
Herczeg, G. J., Linsky, J. L., Walter, F. M., Gahm, G. F., & Johns-Krull, C. M. 2006, ApJS, 165, 256
Kastner, J. H., Huenemoerder, D. P., Schulz, N. S., Canizares, C. R., & Weintraub, D. A. 2002, ApJ, 567, 434
Kwan, J. & Tademaru, E. 1988, ApJ, 332, L41
Lavalley, C., Cabrit, S., Dougados, C., Ferruit, P., & Bacon, R. 1997, A&A, 327, 671
Lavalley-Fouquet, C., Cabrit, S., & Dougados, C. 2000, A&A, 356, L41
Matt, S. & Pudritz, R. E. 2005, ApJ, 632, L135
Matt, S. & Pudritz, R. E. 2007, in IAU Symposium, Vol. 243, IAU Symposium, ed. J. Bouvier & I. Appenzeller, 299–306
McGroarty, F., Ray, T. P., & Froebrich, D. 2007, A&A, 467, 1197
Pravdo, S. H., Feigelson, E. D., Garmire, G., et al. 2001, Nature, 413, 708
Preibisch, T., Kim, Y.-C., Favata, F., et al. 2005, ApJS, 160, 401
Pyo, T.-S., Kobayashi, N., Hayashi, M., et al. 2003, ApJ, 590, 340
Raga, A., Cabrit, S., Dougados, C., & Lavalley, C. 2001, A&A, 367, 959
Raga, A. C., Noriega-Crespo, A., & Velázquez, P. F. 2002, ApJ, 576, L149
Scelsi, L., Maggio, A., Micela, G., Briggs, K., & Güdel, M. 2007, A&A, 473, 589
Schmitt, J. H. M. M., Robrade, J., Ness, J.-U., Favata, F., & Stelzer, B. 2005, A&A, 432, L35
Schneider, P. C. & Schmitt, J. H. M. M. 2008, A&A, 488, L13
Shu, F., Najita, J., Ostriker, E., et al. 1994, ApJ, 429, 781
Stelzer, B., Flaccomio, E., Briggs, K., et al. 2007, A&A, 468, 463
Stelzer, B. & Schmitt, J. H. M. M. 2004, A&A, 418, 687
Takami, M., Chrysostomou, A., Ray, T. P., et al. 2004, A&A, 416, 213

List of Objects

Chapter 8

The enigmatic X-rays from the Herbig star HD 163296: Jet, accretion or corona?

H.M. Günther and J.H.M.M. Schmitt
Astronomy & Astrophysics, accepted

Astronomy & Astrophysics manuscript no. HD163296˙2
December 15, 2008

The enigmatic X-rays from the Herbig star HD 163296: Jet, accretion or corona? ⋆⋆⋆

H. M. Günther and J. H. M. M. Schmitt

Hamburger Sternwarte, Universität Hamburg, Gojenbergsweg 112, 21029 Hamburg, Germany
e-mail: moritz.guenther@hs.uni-hamburg.de

Received 22 September 2008 / accepted 28 November 2008

ABSTRACT

Context. Herbig Ae/Be stars (HAeBe) are pre-main sequence objects in the mass range 2 $M_\odot < M_* < 8$ $M_\odot$. Their X-ray properties are uncertain and, as yet, unexplained.
Aims. We want to elucidate the X-ray generating mechanism in HAeBes.
Methods. We present an *XMM-Newton* observation of the HAeBe HD 163296. We analyse the light curve, the broad band and the grating spectra, fit emission measures and abundances and apply models for accretion and wind shocks.
Results. We find three temperature components ranging from 0.2 keV to 2.7 keV. The O VII He-like triplet indicates an X-ray formation region in a low density environment with a weak UV photon field, i. e. above the stellar surface. This makes an origin in an accretion shock unlikely; instead we suggest a shock at the base of the jet for the soft component and a coronal origin for the hot component. A mass outflow of $\dot{M}_{\rm shock} \approx 10^{-10} M_\odot$ yr^{-1} is sufficient to power the soft X-rays.
Conclusions. HD 163296 is thought to be single, so this data represent genuine HAeBe X-ray emission. HD 163296 might be prototypical for its class.

Key words. stars: formation – stars: individual: HD 163296 – X-rays: stars

1. Introduction

The phase between protostar and main-sequence object is a key stage for planet formation and, furthermore, the properties of a star are determined precisely during that phase for the rest of its life. It is therefore important to study objects of this age in order to understand the origin of planetary systems. Herbig Ae/Be stars (HAeBes) are thought to be the predecessors of main-sequence (MS) stars in the mass range 2 $M_\odot < M_* < 8$ $M_\odot$, although the empirically defined object class of HAeBes may in fact encompass a wider range of evolutionary stages such as stars with magnetospheric accretion (Ae) and boundary layer objects (Be). HAeBes are certainly young, they do have clear signatures of surrounding disks and thus must be considered to be the more massive brothers of the better studied classical T Tauri stars (CTTS), which are young (< 10 Myr), low mass ($M_* < 3M_\odot$), pre-main sequence stars exhibiting strong Hα emission. CTTS are also surrounded by disks, as evidenced by a strong infrared excess, and are actively accreting material.

Strong X-ray emission is a characteristic property of most young stellar objects. A review of the observational situation before *XMM-Newton* and *Chandra* for low mass stars is given by Feigelson & Montmerle (1999). Zinnecker & Preibisch (1994) were the first to carry out a systematic X-ray survey of HAeBes. Restricting attention to those stars located within 500 pc, 70 % of all HAeBes were found to produce detectable X-ray emission with X-ray luminosities ranging between a few 10^{29} erg s^{-1} and 10^{31} erg s^{-1}, thus exhibiting a much larger detection rate than found for field A-type stars (10-15 %, according to Schröder & Schmitt (2007)). Also, Giardino et al. (2004) report the detection of a large X-ray flare (with *XMM-Newton*) from the Herbig Ae star V892 Tau, and present strong arguments that the flare in fact originated from the Ae star in the V892 Tau system; note, however, that Smith et al. (2005) show V892 Tau to be a close binary. Until today it is unclear whether the observed X-ray emission originates from the HAeBes themselves or from unresolved companions, which by necessity would have to be low-mass, young, and active stars. Skinner et al. (2004) studied a sample of ten close HAeBes and showed that the X-ray emission probably originates from a magnetically confined plasma, although it remains unclear if this plasma is associated with a companion. In a sample of 17 HAeBes Stelzer et al. (2006) find X-ray emission in about 80 % of the objects, more than can be reasonably expected from late-type companions, although it is possible that their sample is biased towards known X-ray sources. In a follow-up paper, Stelzer et al. (2008) detect **all objects in their sample**, but again many of them show spectral characteristics compatible with low-mass companions.

X-ray astronomy has been revolutionised by the availability of high resolution grating spectroscopy in the current generation of X-ray satellites. Grating spectra of HAeBes published so far are taken from AB Aur (Telleschi et al. 2007) and the spectroscopic binary HD 104237 (Testa et al.

⋆ Based on observations obtained with XMM-Newton, an ESA science mission with instruments and contributions directly funded by ESA Member States and NASA.
⋆⋆ Fig. 3 is available in electronic form via http://www.edpsciences.org

2008), where the main component is a Herbig Ae star with a CTTS companion of spectral type K3. More observations are available from CTTS; their high resolution X-ray spectra typically show a soft component (which may be hidden by large absorption columns) and unusually low f/i-ratios in the He-like triplets of Ne and O. For CTTS the most promising explanation for these phenomena is a magnetically funnelled infall model. The inner disk is truncated at the corotation radius and ionised material is loaded onto the field, flowing along the magnetic field lines and hitting the stellar surface close to free-fall velocities (e.g. Shu et al. 1994). In the photosphere an accretion shock develops, which produces the soft X-ray component. Because the plasma has relatively high densities, the f/i-ratios in the Ne IX and O VII triplets are small. This model has been successfully applied in explaining the X-ray emission from the CTTS TW Hya in terms of an accretion shock model plus a hot corona (Günther et al. 2007).

A question unanswered to date is whether the accretion disks surrounding HAeBes lead to similar phenomena as those surrounding CTTS or if other modes of X-ray generation operate in the more massive stars. This could be, e.g., magnetically confined winds colliding in the equatorial plane as suggested for IQ Aur by Babel & Montmerle (1997), or internal shocks in unstable winds as in the CTTS DG Tau (Güdel et al. 2005, 2008; Schneider & Schmitt 2008; Günther et al. 2008).

All these models require magnetic fields, which are only weak in evolved A and B stars, because of the absence of an outer convection zone required for a solar-type $\alpha-\Omega-$dynamo. Nevertheless the HAeBes could have magnetic fields, produced by the compression of a primordial field of the proto-stellar cloud. It has been suggested that they are the progenitors of the magnetic Ap/Bp stars (Wade et al. 2005), which comprise about 5% of the total A star population.

In order to investigate the origin of the X-rays from HAeBes we performed X-ray observations of HD 163296 with *XMM-Newton*, whose stellar properties we explain in Sect. 2, before presenting the observations in Sect. 3. We show the results of our analysis in Sect. 4 and discuss their implications in Sect. 5. Sect. 6 gives our conclusions.

2. Stellar properties

HD 163296 is an isolated HAeBe far from any natal molecular cloud. With its distance of 122^{+17}_{-13} pc (van den Ancker et al. 1998) it is one of the closest objects of its kind, making it an ideal target for studies of young A stars. The presence of cold dust around HD 163296 has long been known from spatially unresolved observations (Mannings 1994), and a few years ago the disk of HD 163296 has been coronographically imaged with *HST*/STIS showing indications for a planetary body in the disk (Grady et al. 2000). Furthermore, these observations allow us to trace an outflow in the Lyα line from 7.3 AU to 725 AU with a velocity of ≈ 350 km s^{-1} (Devine et al. 2000). This jet, called HH 409, contains knots up to about 3000 AU from the central star, with an asymmetry between jet and counterjet (Wassell et al. 2006). The surrounding disk has also been imaged in the millimetre range indicating a strongly evolved disk, where larger bodies already influence the evolution of the gas (Isella et al. 2007). The spectrum of HD 163296 displays a strong infrared excess, which can be attributed to the inner disk regions. Apart from a single outburst the optical lightcurve has been remarkably constant over the last 25 years (Sitko et al. 2008).

The star itself is of spectral type A1 with an effective temperature $T_{\rm eff} = 9300$ K, a radius $R = 2.1\ R_\odot$ and a mass $M = 2.3\ M_\odot$. According to evolutionary models this places it at an age of about 4 Myr. With an $A_V = 0.25$ the star is only mildly absorbed (van den Ancker et al. 1998). Hubrig et al. (2006) performed spectropolarimetric observations of circularly polarised light at the VLT for some HAeBes, but were unable to detect a significant longitudinal magnetic field ($B_Z = -57 \pm 33$ G) on HD 163296; they remark, however, that a monitoring campain, which could detect accretion funnels, is still missing. Deleuil et al. (2005) present *Far ultraviolet spectroscopic explorer (FUSE)* and *HST*/STIS observations of HD 163296 showing chromospheric signatures and over-ionised species. These can be explained by either an accretion shock or in a magnetically confined wind model. Hydrogen Lyα and C III lines show outflow signatures. Swartz et al. (2005) looked for signatures of a companion, but *HST*/STIS imagery excludes binarity down to $0\farcs05$ separation. Their long-slit STIS spectra also show only the emission of an early-type unresolved point source.

HD 163296 is a *ROSAT* X-ray source, detected in the *ROSAT* all-sky survey (RASS) data with an elongated source near the position of HD 163296 and resolved in three sources with an unpublished *ROSAT*/HRI pointing. Swartz et al. (2005) confirm the detection of X-ray emission from HD 163296 using *Chandra* ACIS-S in imaging mode. They find an extremely soft spectrum which can be well fitted with a 1-temperature model ($kT \approx 0.5$ keV, where k is Boltzmann's constant and T is the temperature). Additionally there are five X-ray photons at the position of the knot H in the jet. This is a significant source detection at the 95 % confidence level, with a luminosity more than two orders of magnitude below the central component.

Table 1. Observing log.

Observatory	ObsID	Obs. date	Exp. time
Chandra	3733	2003-08-10	20 ks
XMM-Newton	0144271401	2003-10-11	7 ks
XMM-Newton	0502370201	2007-09-23	106 ks
XMM-Newton	0502370301	2007-09-24	22 ks

3. Observations and data reduction

We observed HD 163296 for 130 ks with *XMM-Newton* with the RGS as the primary instrument, applying the medium filter to block out the bright optical radiation. The observation is split in two exposures in consecutive orbits. Additionally we retrieved archival observations from *XMM-Newton* and *Chandra*. Table 1 summarises the observation information. HD 163296 is optically bright, just below the formal brightness limits of the UVW2 and UVM2 filters, but all exposures of the optical monitor are overexposed and unusable for analysis in the inner region. All data was reduced using the standard *XMM-Newton* Science Analysis System (SAS) software, version 7.1 or the *Chandra* Interactive Analysis of Observations (CIAO) software, version 4.0, in the case of the *Chandra* observation. Because

the exposure is partially contaminated by energetic proton events we applied a time filtering, where a good time interval is defined in the usual way for the EPIC/PN camera as < 1 cts s^{-1}. For the EPIC/MOS detectors we lowered the cutoff values to 0.25 cts s^{-1} in order to suppress the high energy noise in the spectra. CCD spectra and count rates were extracted from a circular region within the 15″ around the target for the MOS. We obtained RGS spectra and found a strong contamination in the RGS1. We therefore reduced the extraction region for the RGS1 to the central 66% of the point spread function (PSF), keeping 90% of the PSF extraction region for the RGS2. This step helps to suppress the background. To increase the signal we merged the two exposures for each RGS using the SAS task `rgscombine`. Spectral fitting was carried out using XSPEC V11.3 (Arnaud 1996), and individual line fluxes were measured using the CORA line fitting tool (Ness & Wichmann 2002). Because the line widths are dominated by instrumental broadening, we keep them fixed at $\Delta\lambda = 0.06$ Å.

For comparison purposes we also analysed the *XMM-Newton* data on AB Aur (ObsID 0101440801) which was already presented in great detail by Telleschi et al. (2007). We extracted the central 80% of the PSF in order to minimise the contribution from the close source SU Aur and measured the line fluxes in the He-like triplets of neon and oxygen with the same method used for HD 163296.

4. Results

We first present the variability observed in HD 163296, before we show fits to the emission measure distribution. Then we give individual line fluxes and take a closer look at the density and UV-field sensitive He-like triplets. We compare the O VIII to O VII line ratio with the value found for MS stars.

4.1. Variability

Figure 1 shows the light curve and hardness ratio of the observations taken in 2007. They are binned to 2 ks. We define the hardness ratios as a count ratio of (hard-soft)/(hard+soft), where the hard band is in the range 0.8-2.0 keV and the soft band is 0.2-0.8 keV. HD 163296 exhibits only modest variability over most of the observations with a sudden increase of the count rate by 30% about 30 ks into the observation. No correlation between the hardness and the luminosity is visible. In the beginning low count rates coincide with a hard spectrum, but this pattern does not persist.

To analyse the long-term variability we compare the count rates in the EPIC/PN detectors of all *XMM-Newton* observations. In 2003 the average count rate was 0.166 ± 0.007 cts s^{-1} and in 2007 0.202 ± 0.002 cts s^{-1} and 0.218 ± 0.004 cts s^{-1}. The errors are statistical and do not represent temporal variation within each exposure. The exposure in 2003 is too short to extract a meaningful lightcurve. We obtained a *ROSAT*/HRI count rate of 0.012 cts s^{-1} for a pointing on HD 163296 observed in 1995 from the HRI catalogue and converted it to an energy flux in the band 0.3-2.0 keV using WebPIMMS assuming that a spectral model fitted to the *XMM-Newton* data is applicable. Fitting the same model to the *Chandra* CCD spectrum we also integrated the model flux in the same band as the other observations. The *ROSAT*/HRI luminosity is about 4.3×10^{29} erg s^{-1}; in 2003 *Chandra* recorded 3.8×10^{29} erg s^{-1}, and with 4.1×10^{29} erg s^{-1} the *XMM-Newton* observation taken in the same year shows a flux very similar to the value from 1995. Our new observations are slightly brighter, with average fluxes of 4.5×10^{29} erg s^{-1} and 4.8×10^{29} erg s^{-1} respectively. The uncertainty of the luminosities is dominated by the intrinsic variation, not by count statistics. We find short-term variations of 30% within a single exposure, and the separate observations differ on a similar scale. Thus, we conclude that the total luminosity has not changed much over the past decade, in accordance with the optical behaviour (Sitko et al. 2008).

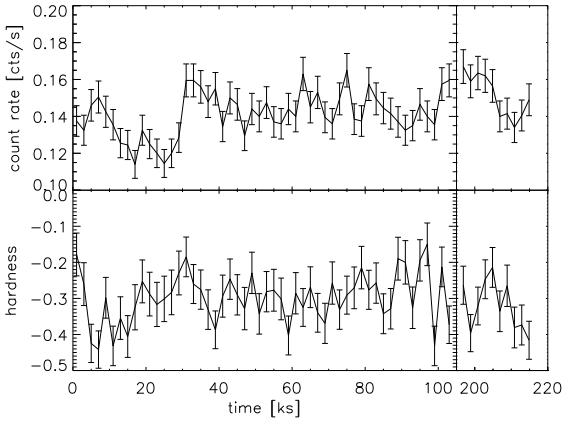

Fig. 1. Lightcurve and hardness (soft band: 0.2-0.8 keV, hard band: 0.8-2.0 keV) during the observations in 2007.

4.2. Emission measure and abundance

Because of the absence of significant variability during our observation in 2007 we jointly fit all available spectra from EPIC/MOS, keeping them separate, and the two RGS spectra, with the two exposures merged for each detector, again keeping data from the two detectors separate. The spectrum can be satisfactorily described by three thermal components with variable abundances. We use `VAPEC` models and give abundances relative to the solar values from Grevesse & Sauval (1998). Our best fit model is shown in Fig. 2, where it is plotted as a line on the MOS1 data. The data is binned to contain at least 15 counts per bin. We show the data only up to 3 keV because the source flux drops quickly and the high-energy spectrum is dominated by residual noise in the data. The spectrum is nearly flat on the low energy side, indicating a weak absorption. Several emission peaks are visible, most notably the Lyα lines of Mg XII at 1.35 keV and Si XIV at 1.85 keV. Line contributions identified in the high resolution RGS spectra are listed in Table 4.

In Tables 2 and 3 we give the best fit parameters for our model and the associated errors (90% confidence interval). The reduced χ^2 value for our model is only 1.1, but fewer components cannot reproduce the data: A fit with one or two components fails to produce the correct slope below 1 keV. This can only be compensated for by extra emission from unresolved carbon lines, which in turn requires a very low contribution from nitrogen around 0.5 keV. In total

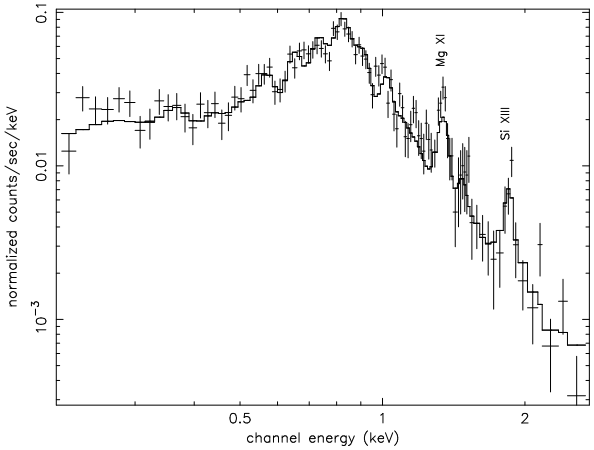

Fig. 2. Low resolution spectrum (MOS1) of HD 163296 and our best-fit model.

Table 2. Best-fit model parameters (90% confidence interval).

component		soft	medium	hard
kT	[keV]	$0.21^{+0.03}_{-0.01}$	$0.51^{+0.1}_{-0.03}$	$2.7^{+1.5}_{-0.8}$
EM	[10^{52} cm^{-3}]	$2.3^{+0.8}_{-0.4}$	$1.2^{+0.5}_{-0.6}$	$0.5^{+0.1}_{-0.2}$
$N_{\rm H}$	[10^{20} cm^{-2}]		7^{+4}_{-4}	

Table 3. Abundance of elements and first ionisation potentials (FIP); errors show 90% confidence intervals.

Element	abundance	FIP [eV]
C	$3.7^{+3.6}_{-1.5}$	11.3
O	$0.7^{+0.2}_{-0.2}$	13.6
Ne	$1.2^{+0.5}_{-0.6}$	21.6
Mg	$2.3^{+1.0}_{-0.8}$	7.6
Si	$2.8^{+1.2}_{-0.8}$	8.1
Fe	$1.6^{+0.7}_{-0.4}$	7.9

these models end up with a carbon abundance an order of magnitude above solar and virtually no nitrogen. We deem this an unphysical scenario and conclude that at least three temperature components are present in HD 163296. Within the error the fit using three components does not change if nitrogen is taken as a free parameter, but the error on its abundance is so high that we prefer to keep it fixed at the solar value. As a cross-check we test the model with the data of the EPIC/PN detector, which has a larger effective area but lower energy resolution; for this case we find the reduced $\chi^2_{\rm red} = 1.1$.

Table 3 shows the abundances as determined from the combined fit. Elements with a low first ionisation potential (FIP) are enhanced. A similar pattern is typical of inactive stars and its signatures can be found in many X-ray data sets (Robrade et al. 2008).

We measure the absorbing column density towards the source as $N_{\rm H} = 7^{+4}_{-4} \times 10^{20}$ cm^{-3}. Assuming a standard gas-to-dust ratio the optical reddening and the X-ray absorption should be related through the formula $N_{\rm H} = A_V \cdot 2 \times 10^{21}$cm^{-2} (Savage & Mathis 1979, see Vuong et al. (2003) for a compilation of other conversion factors in the literature, all roughly consistent with this value). The optical reddening of $A_V = 0.25$ (van den Ancker et al. 1998) is fully consistent with the X-ray value.

4.3. Line fluxes

The spectrum is dominated by emission lines; it is shown binned to a minimum of five counts per bin in Fig. 3 (online only). Applying the global model to the RGS data alone gives $\chi^2_{\rm red} = 1.7$, significantly more than in the joint fit. This is not surprising since our model of only three temperature components is a simplification of the real temperature distribution. Lines which are very sensitive to small temperature differences cannot match the model precisely. The fit can be improved to $\chi^2_{\rm red} = 1.1$ by increasing the abundance of carbon by a factor of two and iron by a factor of four. As explained above we used a smaller extraction region for the RGS1. A comparison between spectra extracted using the standard extraction region and our reduced extraction region shows that our choice of extraction area reduces the noise level. The line fluxes measured with both methods are compatible within the errors. We list the line fluxes in Table 4. Due to zero-point offsets the measured wavelength and its theoretical value can differ; in the table we give the theoretical wavelength of the identified lines together with the fitted values. To fit multiplets we keep the wavelength difference between the components constant. Only three lines are measured in both RGS detectors. In this case we use the error-weighted mean of the RGS1 and the RGS2 flux. The photon fluxes of O VIII Lyα are fully consistent between the RGS1 and the RGS2 within the errors; for Fe XVII 15.01Å and Fe XVII 16.78Å the derived fluxes differ by more than the formal 1σ-error due to the uncertain determination of the background level in particular in the presence of the very close Fe XVII 15.26Å line.

We significantly detect lines of neon, oxygen and carbon in the He-like or H-like ionisation stages and, with a significance just above 2σ, nitrogen. We also find a number of Fe XVII lines, which have a peak formation temperature around 8×10^6 K. From the fitted line fluxes we calculate the total line intensity, using the absorption cross section from Balucinska-Church & McCammon (1992). The relative errors on the line intensity are larger than those on the line fluxes, because here the uncertainty in the fitted $N_{\rm H}$ and the distance contribute to the total error budget.

4.4. He-like triplets

Of special interest are the line fluxes of the He-like triplets in O VII and Ne IX. These triplets consist of a recombination (r), an intercombination (i) and a forbidden (f) line (Gabriel & Jordan 1969; Porquet et al. 2001). So-called R- and G-ratios are defined as $R = f/i$ and $G = (f + i)/r$ respectively; for high electron densities or strong UV photon fields the R-ratio drops below its low-density limit, because electrons can be excited from the upper level of the forbidden to the intercombination line collisionally or radiatively. Figure 4 shows the O VII He-like triplet in the RGS1 detector. The R-ratio is 4.6, which is above the low-density ratio of 3.4 as obtained from the CHIANTI database (Dere et al. 1998; Landi et al. 2006) or 3.95 from APEC (Smith et al. 2001). The error on this ratio is dominated by the statistical

Table 4. Measured line fluxes for HD 163296 with 1σ errors

Line ID	λ (theory)	RGS1		RGS2		flux	unabs. intensity
	[Å]	λ (fit)[Å]	[counts]	λ (fit) [Å]	[counts]	[10^{-6} cts cm^{-2} s^{-1}]	[10^{27} erg s^{-1}]
Ne X Ly α	12.14	n.a.	n.a.	12.14 ± 0.01	38 ± 9	5.1 ± 1.2	17.7 ± 6.2
Ne IX r[a]	13.46	n.a.	n.a.	13.45 ± 0.01	32 ± 9	4.4 ± 1.2	14.5 ± 5.7
Ne IX i[a]	13.56	n.a.	n.a.	13.55 ± 0.01	21 ± 9	2.9 ± 1.2	9.6 ± 4.8
Ne IX f	13.70	n.a.	n.a.	13.69 ± 0.01	22 ± 8	3.0 ± 1.1	9.9 ± 4.6
O VIII Ly α	18.97	18.98 ± 0.01	74 ± 10	18.98 ± 0.01	117 ± 13	18.7 ± 2.2	54.6 ± 20.4
O VII r	21.6	21.57 ± 0.01	42.7 ± 7.8	n.a.	n.a.	14.6 ± 2.7	45.2 ± 21.5
O VII i	21.8	21.77 ± 0.01	7.8 ± 4.4	n.a.	n.a.	3.2 ± 1.8	10.0 ± 7.2
O VII f	22.1	22.07 ± 0.01	46.2 ± 8.1	n.a.	n.a.	14.6 ± 2.6	46.0 ± 22.6
N VII Ly α	24.78	n.a.	n.a.[b]	24.78 ± 0.01	14 ± 6	3.3 ± 1.4	8.0 ± 4.6
C VI Ly α	33.70	n.a.	n.a.	33.70 ± 0.01	50 ± 9	20 ± 3.6	73.0 ± 56.6
Fe XVII	15.01	15.01 ± 0.01	50 ± 9	15.03 ± 0.01	101 ± 13	11.5 ± 1.7	35.5 ± 11.6
Fe XVII	15.26	n.a.	n.a.[b]	15.28 ± 0.01	68 ± 11	8.7 ± 1.4	26.8 ± 9.0
Fe XVII	16.78	16.79 ± 0.01	26 ± 7	16.78 ± 0.01	59 ± 11	6.6 ± 1.3	20.0 ± 7.6
Fe XVII	17.05[d]	n.a.	n.a.	17.05 ± 0.01[c]	53 ± 14	7.4 ± 1.9	22.4 ± 9.3
Fe XVII	17.10[d]	n.a.	n.a.	17.10 ± 0.01[c]	59 ± 14	8.2 ± 1.9	24.9 ± 10.0

[a] line blended (see text)
[b] region contains empty bins
[c] lines are not resolved, but two components are necessary to reproduce the line width, for the fit we fix the difference in λ

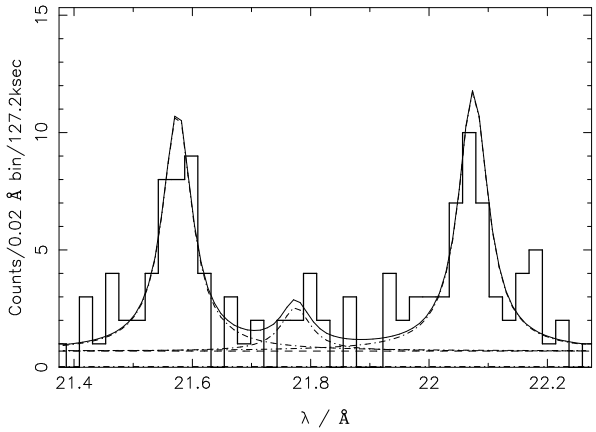

Fig. 4. O VII He-like triplet with our best fit to recombination, intercombination and forbidden line.

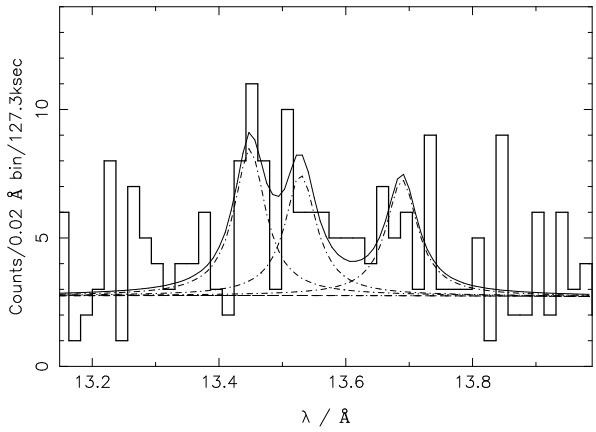

Fig. 5. Ne IX He-like triplet with our best fit to r, i and f line. The i lines is blended with strong iron emission.

error on the weak i line and is significantly asymmetric. We run a Monte-Carlo simulation to obtain lower limits on the R-ratio, which are described in detail in appendix A. We determine the background from the line-free regions in the range 20-25 Å to 30 counts Å^{-1}. At a 90% confidence level the R-ratio is higher than 2.6, at a 99% confidence level the lower boundary is 1.7, it is thus fully compatible with the low-density limit, but not with a high-density case. The G-ratio is $1.2^{+0.6}_{-0.4}$ (90% confidence), where the errors are based on the same method. According to the CHIANTI database this diagnoses a plasma temperature between 0.02 keV and 0.2 keV, a range below the coolest component fitted in the global emission measure analysis, but in nature the plasma is not divided between three components of fixed temperature, instead each component has to be interpreted as a representative for a range of temperatures. O VII forms only on the cool end of that distribution, O VIII is the dominant ionisation stage above 0.20 keV. Therefore it is not surprising to find a lower temperature from the O VII G-ratio. A small G-ratio could also be due to photoexcitation (Porquet & Dubau 2000).

The interpretation of the Ne IX triplet is more difficult as the i line can be strongly blended by iron lines, predominantly Fe XIX and Fe XX. The signal is not sufficient for a detailed deblending as in Ness & Jordan (2008). However, there are two indications that the counts in the i line are dominated by iron contamination: first, we fitted the He-like Ne triplet keeping the relative wavelength constant; the results of this step are given in Table 4 and shown in Fig. 5. Then we kept the wavelength for the r and f line where the blending is less severe and left it free for the i line. The best fit is $\lambda = (13.53 \pm 0.09)$ Å, just between Fe XIX at 13.52 Å and the Ne IX intercombination line at 13.55 Å. Second, from a theoretical point of view, we simulated the spectra in the region of the Ne IX He-like triplet with CHIANTI using the emission measures from Table 2 and the abundances given in Table 3. For the spectral resolution of the RGS detectors three distinct emission peaks

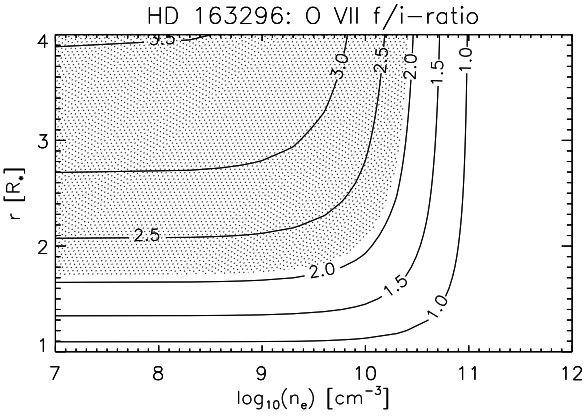

Fig. 6. O VII He-like triplet f/i ratio depending on the density of the emitting region and the position. Those regions of the parameter space within the 90% confidence range are shaded.

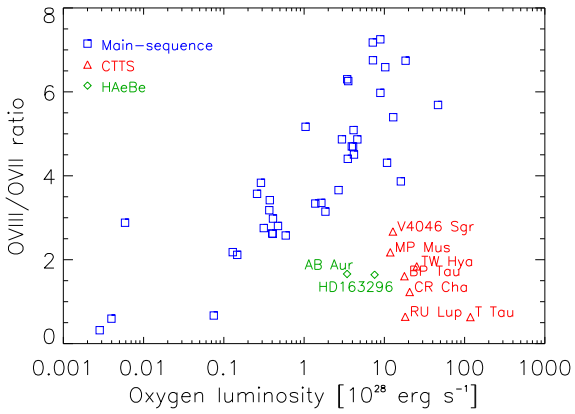

Fig. 7. Ratio of O VIII flux to O VII flux. (colour in electronic version only)

are expected. The middle one is always dominated by iron lines, even in the case of high densities or strong UV-fields. It is always predicted with a photon flux comparable to the r line. However, the f line is dominated by emission from neon. It is detected with the same flux as the r line in our observation (Table 4 and Fig. 5), but should be nearly absent in the case of high densities or strong UV-fields. From these arguments we cannot obtain a numerical f/i value, but qualitatively it is clear that the R-ratio of the Ne IX triplet is high, similar to the R-ratio of the O VII triplet.

The theory of the He-like triplets is well developed (Gabriel & Jordan 1969; Porquet et al. 2001) and the R and G-ratios are understood. To calculate the expected f/i we use the formula given in Blumenthal et al. (1972):

$$R = \frac{f}{i} = \frac{R_0}{1 + \Phi/\Phi_c + n_e/N_c} \quad (1)$$

where R_0 denotes the low density limit (3.95 for the case of O VII). N_c and Φ_c represent the critical density and photon field respectively, where the R-ratio becomes density or radiation sensitive. n_e is the electron density. The relevant wavelength to excite an electron from the upper level of the f to the i line is 1630 Å in the O VII triplet and we obtain the corresponding stellar flux from an *IUE* observation (Valenti et al. 2000). We deredden the flux with $A_V = 0.25$ (van den Ancker et al. 1998) according to the formula of Cardelli et al. (1989). This in turn gives a radiation temperature and allows us to calculate the stellar radiation field to get Φ/Φ_c (for details see Ness et al. 2002). We use a geometric dilution factor W to express the decrease of the radiation field with increasing distance r to the stellar surface R_*:

$$W = \frac{1}{2}\left(1 - \sqrt{1 - \left(\frac{R_*}{r}\right)^2}\right) . \quad (2)$$

Figure 6 shows contours of the expected R-ratio in the O VII He-like triplet depending on the density of the emitting region and its position, expressed in stellar radii, where we define the stellar surface as $r = 1$. The region compatible with the observation is shaded in grey. Qualitatively this agrees with the requirement of a large R-ratio in the Ne IX triplet. Clearly we need to look for emission scenarios, where the emission region is located above the stellar surface and the electron number density is below 10^{10} cm^{-3}.

The observation of AB Aur is less well exposed. Additionally the i line in the O VII triplet contains two missing data bins caused by damaged rows in the detector. The f line is clearly present and there can be no contamination of the oxygen triplet by the near, bright source SU Aur because it is strongly absorbed. So we agree with Telleschi et al. (2007) that there are indications for a large f/i ratio, but we cannot give a reliable number of counts in the i line. For neon we find $f/i = 2.4^{+3.4}_{-1.3}$ (90% confidence). Due to our small extraction region the contribution of SU Aur in the Ne IX triplet should be negligible, furthermore AB Aur seems to be iron depleted (Telleschi et al. 2007), but any iron contamination would further enhance the f/i ratio. This observation favours low-density emission regions above the stellar surface, too.

4.5. Cool excess

Robrade & Schmitt (2007) and Güdel & Telleschi (2007) present an analysis of the O VIII/O VII ratio as a measure of the excess of soft emission in CTTS with respect to stars on the MS. These studies show the observed excess to be confined to a narrow temperature range about the formation of the He-like O VII triplet at 1-2 MK. In Fig. 7 we add the two HAeBe stars with resolved O VII and O VIII lines to their sample. The MS stars are taken from Ness et al. (2004). The sample of CTTS has higher total luminosities in oxygen than the HAeBes. This is a selection bias because the analysis requires a clear separation of the O VIII and O VII line which only grating spectra allow. Those observations usually probe the most luminous members of each class. The O VIII to O VII ratio for a given luminosity is smaller for all young stars than for MS stars, indicating that the younger stars are cooler. Within the CTTS there is a tentative trend with the youngest stars in the Taurus molecular cloud and the Lupus-Auriga star forming region at the bottom and older objects like MP Mus and TW Hya closer to the MS. We can plot the ratio only for two HAeBes with approximately the same age, but both are set clearly

apart from the MS. As for CTTS, MS stars of the same luminosity would be considerably harder. In CTTS this soft excess is presumably caused by accretion but a contribution from winds and outflows is also possible. We present our interpretation of the cool excess in HAeBes in Sect. 5.4.

5. Discussion

First, we compare our results for HD 163296 to those obtained for AB Aur and HD 104237 (Sect. 5.1). In Sect. 5.2 we present reasons to reject the hypothesis that an as yet undetected companion is responsible for the X-ray emission. In Sect. 5.3 we discuss the speculation by Swartz et al. (2005) on the basis of *Chandra* imaging, that HD 163296 may be accretion dominated like the classical T Tauri star TW Hya. A full review of many possible X-ray generation mechanisms including accretion, winds, and disk-related models is given in Telleschi et al. (2007). Because little information is available to constrain many of those models from X-ray observations, we refer the reader to that publication for a larger variety of models. In Sect. 5.4 we discuss which mechanism might be responsible for the soft X-ray emission and in Sect. 5.5 we present a corona from primordial fields as a good candidate for the origin of the hard component.

5.1. Comparison to AB Aur and HD 104237

HD 163296 and AB Aur share many characteristics. They are of the same age and the spectrum differs only by one or two subtypes around A0. HD 104237 is of spectral type A8. It thus seems natural to expect similar X-ray properties from these stars. And, indeed, the total luminosity of $\log L_X$ for the first two stars is 29.6 erg s^{-1}, HD 104237 is brighter ($\log L_X \approx 30.5$ erg s^{-1}), although a contribution of about 10% from HD 104237-B has been removed from the grating spectrum (Testa et al. 2008). It is unknown how much luminosity the HAeBe primary contributes and which fraction is due to the unresolved, close CTTS companion of HD 104237. In a fit with two emission components, about one third of the total emission measure is found at 0.2 keV for AB Aur, in contrast to HD 163296 where, according to Table 2, 60% fall in this temperature region. Due to their lower signal, Telleschi et al. (2007) do not split the hotter component as we do. Their temperature is comparable to our medium component. We find the hardest component in HD 163296 to be the one with the lowest emission measure, although it is significantly detected in our observation. If the same emission mechanism is invoked for AB Aur and HD 163296 then a convincing explanation needs to be found as to why HD 163296 is softer. HD 104237 is significantly hotter; only little emission measure is found below 0.25 keV in the reconstructed emission measure distribution. Again, the hot plasma might be due to the unresolved CTTS.

As for elemental abundances we left carbon as a free parameter instead of nitrogen as Telleschi et al. (2007) did. To compare the fitted values for O, Ne, Mg, Si and Fe we first need to correct them to the same reference values. On the one hand, in AB Aur Ne and Si have the largest abundance and O, Mg, and Fe the smallest; in HD 163296 on the other hand C, Si, Mg and Fe, those elements which condense on grains easily, are found with enhanced abundance. A very similar pattern is found from the spectrum of HD 104237, only here S was left as a free parameter of the fit instead of C. We show the abundance pattern of all three stars in Fig. 8. The abundance distribution of AB Aur looks erratic, whereas in HD 163296 there is a trend with the FIP effect. For HD 104237 the pattern is very similar to HD 163296 except for a higher neon abundance. However, in young objects such as HD 163296 with ongoing accretion the physical mechanism might be different; the same abundance pattern can also be interpreted as an overabundance of elements released from refractory grains. The noble gas neon does not condense as easily on grains as the other elements in Table 3.

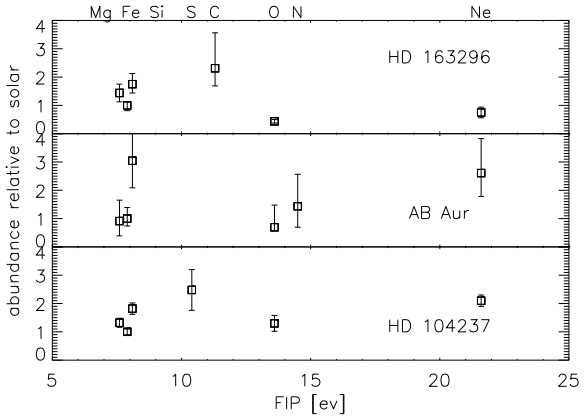

Fig. 8. Abundances for HD 163296, AB Aur (Telleschi et al. 2007) and HD 104237 (Testa et al. 2008). Error bars show 1σ uncertainties and all abundances are normalised to iron.

For line emission spectra with only little continuum the absolute metallicity is very uncertain. Although the luminosities of both stars are equal, Telleschi et al. (2007) find a larger emission measure for AB Aur and at the same time a lower metallicity. This likely does not point to a physical difference but only shows an ambiguity in the fitting process, so we normalised all abundances in Fig. 8 with respect to Fe. If different emission mechanisms, e.g. a corona and a jet contribute to the emission, then those abundances represent an average value. Therefore we conclude than an emission mechanism for soft X-rays, which is possibly based in a region of now gaseous former refractory grains, operates in HD 163296 much more strongly or in addition to the processes active in AB Aur and possibly HD 104237.

5.2. A companion?

Because HAeBe stars are not expected to posses an outer convective layer, X-ray emission detected from these objects is often attributed to low-mass companions. The high optical luminosity of the main component could overwhelm the optical emission of close CTTS. In several systems, high resolution *Chandra* images allow to separate multiple components (Stelzer et al. 2006, 2008); still as yet undetected companions closer to the central HAeBe star might exist. In the case of HD 163296 there is no second stellar source resolved in the images and the source position matches the expected coordinates within 1σ of the *Chandra* pointing accuracy (Swartz et al. 2005). Furthermore, the same authors obtained *HST*/STIS data with no sign of binarity. All this makes an origin in a late-type companion unlikely. Also, the

X-ray data differs significantly from both a CTTS in the f/i ratio and a weak-lined T Tauri star (WTTS) which display activity seen in hot plasma and variable, flaring lightcurves (Preibisch et al. 2005).

5.3. Accretion?

The relative softness of the spectrum lead Swartz et al. (2005) to speculate that HD 163296 may be dominated by a strong accretion component. Accretion of matter could proceed along magnetically funnelled streams from the disk to the stellar surface. This is the standard scenario for CTTS (Uchida & Shibata 1984; Koenigl 1991). The accretion proceeds with free-fall velocity and a strong shock develops on the stellar surface. We fitted HD 163296 with an accretion shock model (Günther et al. 2007) and two `VAPEC` components. In short, our model takes the infall velocities and densities as input. It heats the matter up in a strong shock and follows the cooling in the post-shock accretion zone in a 1D geometry. The code explicitly takes into account non-equilibrium ionisations. The soft emission around 0.2 keV and some of the medium emission could be produced by a shock with low densities of 4×10^{10} cm^{-3} or less which is falling in at around 550 km s^{-1}. A filling factor $f = 7 \times 10^{-4}$ of the stellar surface is sufficient to produce the observed luminosity. At the given shock parameters about 20 % of the total accretion luminosity are emitted in X-rays; the mass accretion rate in this case would be $\dot{M} = 10^{-11} M_{\odot}$ yr^{-1}. Given the stellar parameters of AB Aur a similar scenario could apply to that star, too. The accretion rate is much lower than the $\dot{M} = 10^{-8} - 10^{-7} M_{\odot}$ yr^{-1} found by optical observations (Garcia Lopez et al. 2006) or modelling of the spectral energy distribution (SED) (Dent et al. 2006). This resembles our results for CTTS (Günther et al. 2007; Günther & Schmitt 2007) and we attribute it to non-uniform accretion spots, which only produce X-rays in the innermost hottest and densest parts of the spot. Our argument contrasts with Telleschi et al. (2007): they take the optically determined accretion rate and the density and distribute it over the stellar surface, which results in a flux much higher than observed. Our models are more sophisticated and explicitly give the fraction of the accretion luminosity that is radiated in the soft X-ray band, but they are invalid in the case of strong absorption. The low column density found in the observation supports the validity of our model. We expect the post-shock cooling zone to penetrate the stars down to $0.97 R_*$, but most of the X-ray emission is generated close to the stellar surface. Due to the low density of the pre-shock material, the optical depth is low and the X-rays escape. Observationally a large optical depth would be seen as a significantly suppressed resonance line in the He-like triplets, whereas the intercombination and the forbidden lines remain unaltered. In all stars analysed so far the strength of resonance line is compatible with the expected G-ratio, thus proving that the emission is optically thin.

In addition to the energetics, the accretion shock model explains the small f/i ratios found in CTTS with the high densities in the post-shock cooling zone (Günther et al. 2007), but in HD 163296 and AB Aur we find an f/i which is fully compatible with the low-density limit. **This excludes an emission origin close to the stellar surface** because here the stellar radiation field of an A type star would radiatively shift emission from the f to the i line, if the accretion zone is not shielded from the radiation. If it is, e.g. by the outer layer of the accretion stream, then the X-ray emission should be more absorbed, but the measured absorbing column density already agrees well with the stellar optical reddening (Sect. 4.2) without an extra absorption component. So we reject the original idea by Swartz et al. (2005) that the soft X-ray emission in HD 163296 is powered by accretion shocks.

5.4. The origin of the soft component

The soft radiation in our three component model originates in a plasma with temperatures around 0.21 keV$\approx 2.4 \times 10^6$ K. Plasma can be heated to this temperature if gas moves with and passes through a strong shock (it can be slower then the 550 km s^{-1} mentioned above because we try to explain the soft component only), according to the Rankine-Hugoniot conditions, which lead to the following formula:

$$\left(\frac{v_{\rm shock}}{400 \text{ km s}^{-1}} \right)^2 \approx \frac{\mathrm{k}T}{0.21 \text{ keV}}, \tag{3}$$

where we transform the kinetic energy of the pre-shock velocity $v_{\rm shock}$ in the shock rest frame into the post-shock thermal energy kT. Situations other than the accretion shock discussed above can give rise to such scenarios. Shocks occurring in winds or outflows easily fulfil the conditions of the density and distance to the photosphere set by the analysis of the He-like triplets. In AB Aur temporal variation in the X-ray luminosity was detected which is compatible with the period of 42 h, observed in Mg II and He I lines which are tracers of winds and outflows (Telleschi et al. 2007). Shocks could develop where fast and slow winds collide either through magnetic collimation or because of temporal variability of the launching velocity. Here we want to discuss a scenario not covered by Telleschi et al. (2007).

HD 163296 drives two powerful collimated jets which are visible in coronographic images obtained with *HST* (Devine et al. 2000; Grady et al. 2000). In this respect it is similar to the lower mass CTTS DG Tau, where X-ray emission has also been detected from the jets (Güdel et al. 2005, 2008). The high extinction of the central source DG Tau itself allows us to detect a significant offset between the soft and the hard X-ray emission (Schneider & Schmitt 2008), because it absorbs all contributions from the star in the low energy band. This offset points to an origin of the soft emission in the jet forming region, possibly as a collimation shock or in an emerging knot where faster ejecta catch up with previous older outflows (Günther et al. 2008). We searched for an offset in the *Chandra* data for HD 163296, but could not find any deviation from the expected PSF, so the emission region must be within 100 AU of the star. Line ratios of Fe II indicate electron densities between 10^4 and 10^5 cm^{-3} in the knots of the jet (Wassell et al. 2006). Presumably the density increases towards the star, so we assume a pre-shock particle number density of $n_0 = 10^6$ cm^{-3} in the shock region. With this assumption we can apply the approximation to the post-shock cooling length $d_{\rm cool}$ of Raga et al. (2002):

$$d_{\rm cool} \approx 0.8 \text{AU} \left(\frac{10^6 \text{cm}^{-3}}{n_0} \right) \left(\frac{v_{\rm shock}}{400 \text{ km s}^{-1}} \right)^{4.5} \tag{4}$$

and find that $d_{\rm cool}$ is only 0.8 AU. Dividing the volume emission measure (VEM) by the density we obtain the volume and - using the equation above - we can transform this to a radius R of the shock front (in AU) (for details see Günther et al. 2008)

$$R \approx 0.5 \left(\frac{10^6 {\rm cm}^{-3}}{n}\right)^{0.5} \left(\frac{VEM}{10^{52} {\rm cm}^{-3}}\right)^{0.5} \left(\frac{0.21 {\rm keV}}{{\rm k}T}\right)^{1.125}, \quad (5)$$

where we assume a cylindrical geometry with the shock at the cylinder base. The mass flux $\dot{M}_{\rm shock}$ through the shock is independent of the density, because lower densities lead according to Eqn. 5 to larger shock areas:

$$\dot{M}_{\rm shock} \approx 6 \cdot 10^{-11} \frac{M_\odot}{\rm yr} \left(\frac{VEM}{10^{52}\ {\rm cm}^{-3}}\right) \left(\frac{0.21\ {\rm keV}}{{\rm k}T}\right)^{1.75}. \quad (6)$$

For HD 163296 a mass outflow of the order of $\dot{M}_{\rm shock} \approx 10^{-10} M_\odot\ {\rm yr}^{-1}$ is sufficient to power the soft X-ray component; this is two orders of magnitude lower than the mass loss rates determined from UV and optical data (Deleuil et al. 2005; Wassell et al. 2006). Only a small component of the total jet needs to be fast enough to be shocked to X-ray emitting temperatures.

This scenario seems feasible in the light of the optical observations. The velocity of the jet determined from a combination of radial velocity and proper motion is $v_{\rm jet} = 360 \pm 82$ km s^{-1} (Wassell et al. 2006) where the radial velocity is taken as the average of a broader distribution at the position of the innermost knot. The offset between the central source and the knot A is 9″, at the distance of HD 163296 this corresponds to 1100 AU. Certainly the jet is launched faster and decelerates as it goes through the shock and later moves through the surrounding matter. In the shock rest frame the velocity v_1 drops to a quarter of the pre-shock velocity v_0, where the matter passes through the shock front: $4 \cdot v_1 = v_0$. To heat the plasma to the required temperatures we need $\Delta v = v_0 - v_1 = 400$ km s^{-1}. This is all fullfilled if the shock front travels outward along the jet at $v_{\rm front} = 230$ km s^{-1} in the jet rest frame. The jet emerges at $v_{\rm launch} = v_{\rm front} + v_0 = 750$ km s^{-1} and the knot moves at $v_{\rm jet} = v_{\rm front} + v_1 = 360$ km s^{-1} with respect to the star.

Typical jets of CTTS reach up to 400 km s^{-1} (Eislöffel & Mundt 1998), comparable to the case of HD 163296. Rodriguez (1995) report velocities of up to 1000 km s^{-1} out in the jet, so an initial velocity of 750 km s^{-1} is not unreasonable. This X-ray generating mechanism may operate in addition to any of those already suggested for AB Aur or HD 104237. Possibly HD 163296 is softer because AB Aur has no jet that could emit soft X-rays.

Several models for the acceleration and collimation of outflows have been suggested. Even for the class of CTTS where the sample size is much larger than for HAeBes, the exact collimation mechanism is still uncertain. Yet, all models rely on a magnetic field. So the existence of two jets already makes the presence of magnetic fields in the environment of HD 163296 very likely. Spectropolarimetric observations by Hubrig et al. (2007) support this idea with signatures of magnetic fields in Ca II H and K lines likely of circumstellar origin. Unfortunately the signal does not allow a qualitative measurement of the field strength which is needed to estimate the radius of the magnetosphere for alternative models of magnetically confined winds. Also Wade et al. (2007) have questioned the method used in theses studies.

5.5. The origin of the hard component

To heat the plasma that is emitting the hot component, shocks with velocities above 1300 km s^{-1} are needed but the optical observations show no lines that are shifted by this amount. Other heating mechanisms must be responsible and a promising candidate **are reconnection events** in magnetic fields in analogy to the solar and other late-type coronae. No polarisation is found in photospheric lines (Hubrig et al. 2006, 2007) but this may be due to strong small-scale fields with only little global dipole contribution. Young A stars may either still posses primordial magnetic fields or generate their own. In this evolutionary stage the simulations of Siess et al. (2000) predict that HAeBes have a thin outer convective layer where a dynamo could operate or the shear in rapidly rotating stars could cause magnetic fields (Tout & Pringle 1995). Given the detection of polarisation in circumstellar matter and the collimation of the outflow we expect that magnetic fields exist on HD 163296 itself.

No flaring activity has been unambiguously observed on an HAeBe star and especially AB Aur, HD 104237 and HD 163296 show only little variability in their hard components during the observation, but Giardino et al. (2004) give good indications that the flare they observed occured on a HAeBe star and not on the known, but unresolved CTTS companion. We postulate that the medium and hard components of the X-ray emission originate in a stellar corona. At high temperatures the contribution to the O VII and the Ne IX He-like triplet is small so the observed f/i ratio cannot trace the UV field in the emission region of the hard photons.

6. Conclusion

We present an observation of HD 163296 with *XMM-Newton*. This is, after AB Aur, the second grating spectrum of an HAeBe star without -as far as we know- an unresolved companion. The signal-to-noise ratio (SNR) is significantly better than in the first observation. Congruently, both stars show soft spectra with little temporal variability. In all analysed He-like triplets the line ratios point to an emission origin in regions of low density and weak UV photon field, that is at a few stellar radii. On HD 163296 we find an FIP abundance pattern typical of inactive stars.

Both the spectral shape and data from other instruments make an origin of the X-rays in an unknown companion to HS 163296 very unlikely. Therefore we believe we are presenting genuine X-ray data for HAeBe which can be representative for the whole class of these objects.

The optically observed mass flux rates are much higher than required by the energetics of the X-ray radiation in the case of accretion shocks or emission from outflows, but the large f/i-ratios rule out an accretion shock scenario on the stellar surface. We favour a model where the main contribution to the soft X-ray emission comes from shock heated plasma in the jet or wind. Possible geometries include shocks in unsteady winds or collimation shocks on the base of the jet. The collimation of the jets is likely related to a magnetic field, whose origin is unclear. This field can

be a frozen-in primordial magnetic field or the star may generate one in a thin convective layer. We find no other convincing explanation for the hard emission than heating by energetic events from the magnetic field. Thus we predict that with longer observation times we should observe flare-like behaviour on HAeBes.

Acknowledgements. H.M.G. acknowledges support from DLR under 50OR0105.

Appendix A: Error estimation for line ratios

For experiments with low count numbers the observed counts can be taken to be Poisson distributed. For longer exposure times or stronger sources the Poisson distribution can be reasonably approximated by a Gaussian distribution. In this case the error on a line ratio can be calculated according to the conventional error propagation formulae. For weak sources, however, the Poisson distribution leads to significantly asymmetric errors, which are dominated by the statistical uncertainty in the weakest line.

We set up a Monte-Carlo simulation to determine confidence intervals. The instrumental and source background is combined in a total background b, which we assume to be uniform over a range of a few Å. It is measured from a larger line-free region on both sides of the triplet of interest. Thus the mean background level is well known. In the case of the O VII triplet in HD 163296 we determine the background from the line-free regions in the range 20-25 Å [**no a=... occurs here, because the b stands for 'background'**] to $b = 30$ counts Å^{-1}.

For a fit with i lines, the spectrum is divided into i bins centred on the lines,; each bin is $\Delta\lambda_i$ wide, thus the expected background per bin is

$$B_i = b \cdot \Delta\lambda_i \; . \tag{A.1}$$

The line profile is given by the instrument profile; in the case of *XMM-Newton* the data is best fit by a Lorentz profile. For each bin i we compute the fraction a_{ij} of the total line spread function of line j that is expected in bin i. For known line fluxes f_j the observed number of counts in each bin can then be calculated. We write this in form of a matrix equation

$$\boldsymbol{L} = \mathsf{A} \cdot \boldsymbol{F} + \boldsymbol{B}, \tag{A.2}$$

where A is constructed from the a_{ij}, $\boldsymbol{B}$ from B_i and F from f_j. $\boldsymbol{L}$ represents the observed counts per spectral region. Since the sum of Poisson distributions is again Poisson distributed, we can take the number of counts in each bin as Poisson distributed, even it is calculated as the sum over several detector bins. Thus the values of $\boldsymbol{L}$ are Poisson-distributed and we simulated 100 000 realisations of a Monte-Carlo calculation for each bin, taking the observed count number as expectation value [**"expectation value" is meant as the fixed term as it is used in statistics; I cannot use "expected value" here**]. Inverting Eqn. A.2 gives

$$\boldsymbol{F} = \mathsf{A}^{-1} \cdot (\boldsymbol{L} - \boldsymbol{B}) \, . \tag{A.3}$$

From the simulations we use this to obtain the values of the individual line fluxes f. Negative numbers occur if the simulated value of the Poisson distribution happens to be below the fixed background value. We reset these numbers to 0; in the analyses of real data they represent situations where the line seems to be absent, thus producing extreme values for the line ratio. The simulated count ratios are scaled by the effective area and the flux ratios are calculated. The simulated distribution of the f/i-ratio is shown in Fig. A.1. From the cumulative distribution (red/grey line) the confidence limits can be read off.

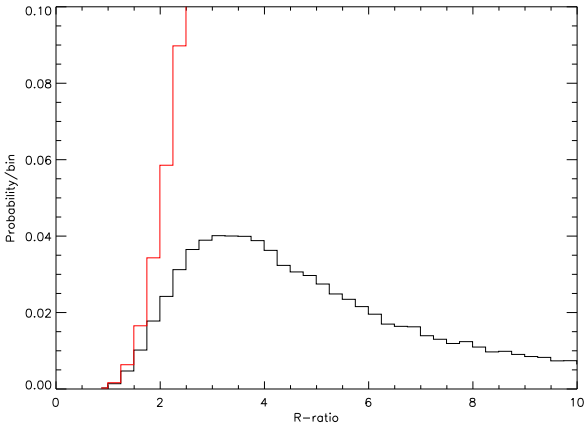

Fig. A.1. Statistical distribution of the R-ratio based on 10^5 realisations of a Poisson statistic for the forbidden and intercombination line. The red/grey line shows the cumulative distribution function.

References

Arnaud, K. A. 1996, in ASP Conf. Ser. 101: Astronomical Data Analysis Software and Systems V, 17–+
Babel, J. & Montmerle, T. 1997, A&A, 323, 121
Balucinska-Church, M. & McCammon, D. 1992, ApJ, 400, 699
Blumenthal, G. R., Drake, G. W. F., & Tucker, W. H. 1972, ApJ, 172, 205
Cardelli, J. A., Clayton, G. C., & Mathis, J. S. 1989, ApJ, 345, 245
Deleuil, M., Bouret, J.-C., Catala, C., et al. 2005, A&A, 429, 247
Dent, W. R. F., Torrelles, J. M., Osorio, M., Calvet, N., & Anglada, G. 2006, MNRAS, 365, 1283
Dere, K. P., Landi, E., Mason, H. E., Fossi, B. C. M., & Young, P. R. 1998, in ASP Conf. Ser. 143: The Scientific Impact of the Goddard High Resolution Spectrograph, 390–+
Devine, D., Grady, C. A., Kimble, R. A., et al. 2000, ApJ, 542, L115
Eislöffel, J. & Mundt, R. 1998, AJ, 115, 1554
Feigelson, E. D. & Montmerle, T. 1999, ARA&A, 37, 363
Gabriel, A. H. & Jordan, C. 1969, MNRAS, 145, 241
Garcia Lopez, R., Natta, A., Testi, L., & Habart, E. 2006, A&A, 459, 837
Giardino, G., Favata, F., Micela, G., & Reale, F. 2004, A&A, 413, 669
Grady, C. A., Devine, D., Woodgate, B., et al. 2000, ApJ, 544, 895
Grevesse, N. & Sauval, A. J. 1998, Space Science Reviews, 85, 161
Güdel, M., Skinner, S. L., Audard, M., Briggs, K. R., & Cabrit, S. 2008, A&A, 478, 797
Güdel, M., Skinner, S. L., Briggs, K. R., et al. 2005, ApJ, 626, L53
Güdel, M. & Telleschi, A. 2007, A&A, 474, L25
Günther, H. M., Matt, S. P., & Li, Z. . 2008, ArXiv e-prints
Günther, H. M. & Schmitt, J. H. M. M. 2007, Memorie della Societa Astronomica Italiana, 78, 359
Günther, H. M., Schmitt, J. H. M. M., Robrade, J., & Liefke, C. 2007, A&A, 466, 1111
Hubrig, S., Pogodin, M. A., Yudin, R. V., Schöller, M., & Schnerr, R. S. 2007, A&A, 463, 1039
Hubrig, S., Yudin, R. V., Schöller, M., & Pogodin, M. A. 2006, A&A, 446, 1089
Isella, A., Testi, L., Natta, A., et al. 2007, A&A, 469, 213
Koenigl, A. 1991, ApJ, 370, L39
Landi, E., Del Zanna, G., Young, P. R., et al. 2006, ApJS, 162, 261

Mannings, V. 1994, MNRAS, 271, 587
Ness, J.-U., Güdel, M., Schmitt, J. H. M. M., Audard, M., & Telleschi, A. 2004, A&A, 427, 667
Ness, J.-U. & Jordan, C. 2008, MNRAS, 385, 1691
Ness, J.-U., Schmitt, J. H. M. M., Burwitz, V., Mewe, R., & Predehl, P. 2002, A&A, 387, 1032
Ness, J.-U. & Wichmann, R. 2002, Astronomische Nachrichten, 323, 129
Porquet, D. & Dubau, J. 2000, A&AS, 143, 495
Porquet, D., Mewe, R., Dubau, J., Raassen, A. J. J., & Kaastra, J. S. 2001, A&A, 376, 1113
Preibisch, T., Kim, Y.-C., Favata, F., et al. 2005, ApJS, 160, 401
Raga, A. C., Noriega-Crespo, A., & Velázquez, P. F. 2002, ApJ, 576, L149
Robrade, J. & Schmitt, J. H. M. M. 2007, A&A, 473, 229
Robrade, J., Schmitt, J. H. M. M., & Favata, F. 2008, A&A, 486, 995
Rodriguez, L. F. 1995, in Revista Mexicana de Astronomia y Astrofisica Conference Series, ed. S. Lizano & J. M. Torrelles, 1–+
Savage, B. D. & Mathis, J. S. 1979, ARA&A, 17, 73
Schneider, P. C. & Schmitt, J. H. M. M. 2008, A&A, 488, L13
Schröder, C. & Schmitt, J. H. M. M. 2007, A&A, 475, 677
Shu, F., Najita, J., Ostriker, E., et al. 1994, ApJ, 429, 781
Siess, L., Dufour, E., & Forestini, M. 2000, A&A, 358, 593
Sitko, M. L., Carpenter, W. J., Kimes, R. L., et al. 2008, ApJ, 678, 1070
Skinner, S. L., Güdel, M., Audard, M., & Smith, K. 2004, ApJ, 614, 221
Smith, K. W., Balega, Y. Y., Duschl, W. J., et al. 2005, A&A, 431, 307
Smith, R. K., Brickhouse, N. S., Liedahl, D. A., & Raymond, J. C. 2001, ApJ, 556, L91
Stelzer, B., Micela, G., Hamaguchi, K., & Schmitt, J. H. M. M. 2006, A&A, 457, 223
Stelzer, B., Robrade, J., Schmitt, J. H. M. M., & Bouvier, J. 2008, submitted to A&A
Swartz, D. A., Drake, J. J., Elsner, R. F., et al. 2005, ApJ, 628, 811
Telleschi, A., Güdel, M., Briggs, K. R., et al. 2007, A&A, 468, 541
Testa, P., Huenemoerder, D. P., Schulz, N. S., & Ishibashi, K. 2008, ApJ, 687, 579
Tout, C. A. & Pringle, J. E. 1995, MNRAS, 272, 528
Uchida, Y. & Shibata, K. 1984, PASJ, 36, 105
Valenti, J. A., Johns-Krull, C. M., & Linsky, J. L. 2000, ApJS, 129, 399
van den Ancker, M. E., de Winter, D., & Tjin A Djie, H. R. E. 1998, A&A, 330, 145
Vuong, M. H., Montmerle, T., Grosso, N., et al. 2003, A&A, 408, 581
Wade, G. A., Bagnulo, S., Drouin, D., Landstreet, J. D., & Monin, D. 2007, MNRAS, 376, 1145
Wade, G. A., Drouin, D., Bagnulo, S., et al. 2005, A&A, 442, L31
Wassell, E. J., Grady, C. A., Woodgate, B., Kimble, R. A., & Bruhweiler, F. C. 2006, ApJ, 650, 985
Zinnecker, H. & Preibisch, T. 1994, A&A, 292, 152

List of Objects

Online Material

H. M. Günther and J. H. M. M. Schmitt: X-ray emission from HD 13296, *Online Material p 2*

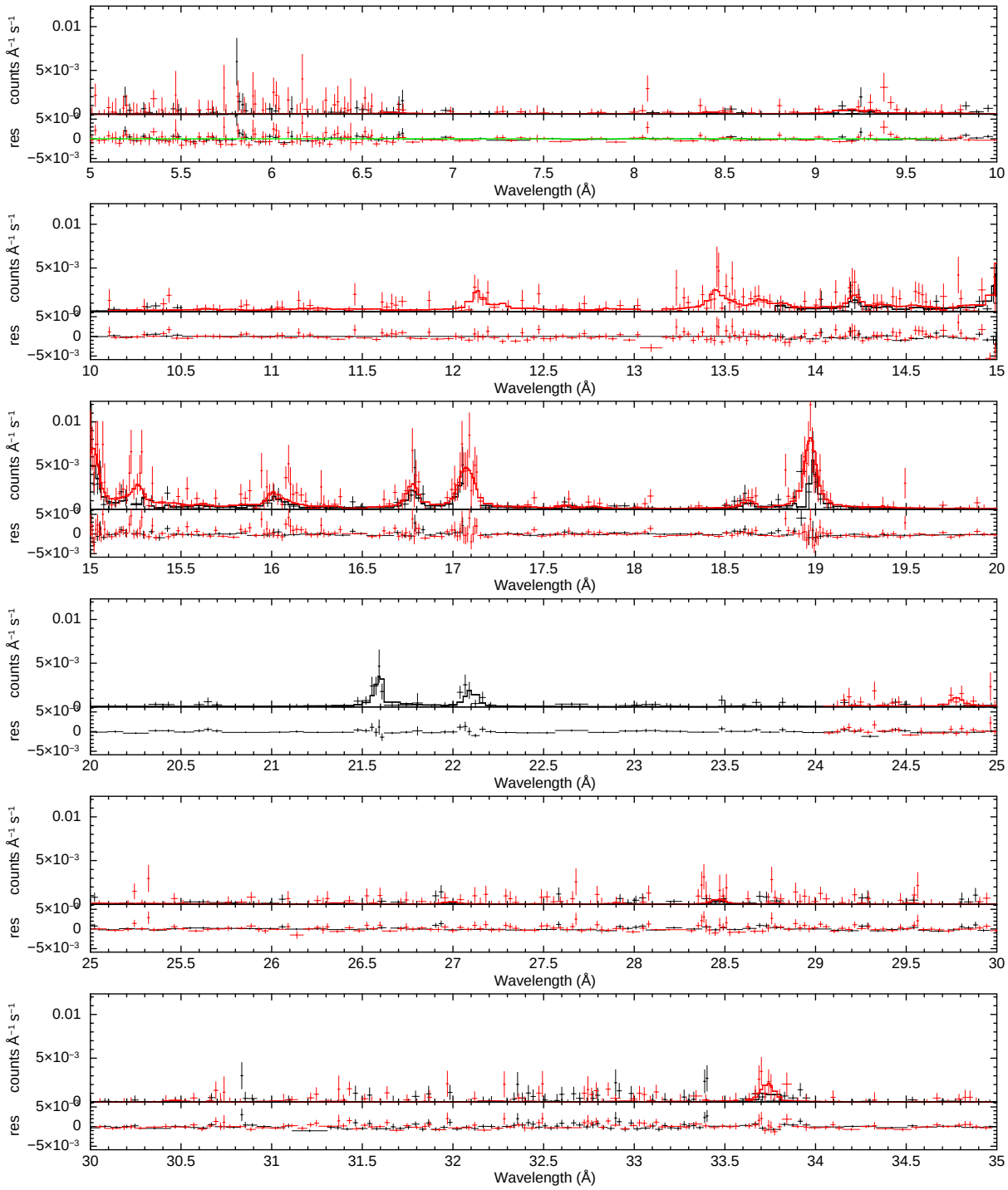

Fig. 3. High resolution RGS spectra with the best-fit model from the global fit in Sect. 4.2 with the corresponding fit residuals. The data is binned to a minimum of 5 counts per bin. *black:* RGS1 *red/grey:* RGS2

Chapter 9

Summary and outlook

In this chapter I first summarise the scientific results from this thesis. Then I comment upon future prospects to persue some issues further.

9.1 Summary

The results presented in the preceding chapters have already been presented on international conferences and published as separate articles, mostly in the refereed journal "Astronomy and Astrophysics". The intention of this approach was to provide the community as early as possible with the new findings and also to publish observational results within or close to the priority period of the PI. Still, they all deal with the common topic of the high-energy emission from young stars, highlighting different aspects of that theme, so it is appropriate to present a summary of all findings here.

Origin of the X-ray emission in CTTS: At least three different processes contribute to the X-ray emission from CTTS, their importance varies between individual objects. First, there is a solar-like corona, second, the post-shock cooling zone of the accretion shock cools radiatively in X-rays and other wavelengths and third, internal shocks in jets can heat matter to X-ray emitting temperatures. This is studied for the individual sources with the best spectra, but there is no reason why these results should not apply to CTTS as a class. For the stars TW Hya and V4046 Sgr the observed spectra were decomposed in the individual contributions. The combined models explain the observed line ratios in the He-like triplets of O VII and Ne IX very well.

Mass accretion rate: In TW Hya and V4046 Sgr the mass accretion rate required to power the X-ray emission (2×10^{-10} $M_\odot$/yr and 3×10^{-11} $M_\odot$/yr, respectively) is much lower than values estimated from other wavelengths. This might be due to inhomogeneous spots, partial absorption or accretion streams, which impact at velocities significantly lower than the free-fall speed.

Mass loss rate: The mass loss rate required to power the X-ray emission of the DG Tau jets is only a small fraction of the total mass loss rate. This is fully compatible with optical observations, that show only the innermost jet component to be sufficiently fast (400 to 500 km s^{-1}) to heat the gas in shocks to X-ray emitting temperatures. For a electron density $> 10^5$ cm^{-3} all dimensions of the shock cooling zone are only a few AU, so even in optical observations this cannot be resolved.

UV line profiles: In some CTTS the UV lines originate in outflows, in others there is likely a contribution from the accretion, however current models cannot explain the observed line profiles. Either there are multiple components or the models are still too simple in neglecting radiation transport and multi-dimensional effects.

Gas-to-dust ratio: The circumstellar environment of some CTTS differs markedly

from the interstellar gas-to-dust ratio. This can be explained, if the outflows of those CTTS are dust-depleted.

HAeBe stars: The X-ray emission from the HAeBe HD 163296 is very likely intrinsic and not due to an unresolved companion. It can thus be established that HAeBes have a hot emission component similar to a solar-like corona. The line ratio in the O VII He-like triplet rules out an accretion shock origin for the soft emission. We present a model, where a large fraction of the soft component is produced in the jet of HD 163296 similar to DG Tau.

9.2 The importance of high-energy observations

Observations in the X-ray and FUV range are expensive, because they are only possible with space-based observatories and their spectral resolution is often much lower than in optical data. If questions can be solved with either optical or X-ray observations, it is usually easier to obtain optical data, but the results summarised above clearly show that X-ray and FUV data contribute unique information to our understanding of young stars, which cannot be obtained from the ground alone. X-ray observations always probe the hottest gas component present in the system. In the case of an accretion shock only X-rays can reveal the physical conditions just behind the accretion shock. No other tracer than the He-like triplets used in this study gives the densities in the post-shock zone directly. This thesis shows that X-ray data is absolutely crucial, if we want to understand the physics of the accretion shock. The same is true for shocks in jets: Altough optical observations reveal much detail of the kinematic structure of the DG Tau jet, they obviously fail to detect the shock front, which is responsible for the X-ray emission. On the other hand, the X-ray emission alone does not show the outer layers of the onion-like nested structure of the jet, so observations in different wavelength regimes contribute complementary to our understanding of the physics of in- and outflows in young stellar objects.

9.3 Outlook

The results obtained in this thesis and by other scientists working in the same field have driven the field of high-energy processes in young stellar objects to maturity. With the new knowledge gained observationally and the refined theories developed, we can now work on details of the accretion which were inaccessible before and rework our original assumptions. In this section I outline new questions which can be asked from this thesis and describe projects which are already under way or could be persued in the future to answer them.

The model of the accretion shock has been applied to TW Hya and V4046 Sgr only, application to the other available CTTS spectra is not straightforward, but requires substantial work, because the shock component is less pronounced there and the signal in the individual lines is often not as good. The combined fitting in `XSPEC` does not yield meaningful results, instead a line based method for the decomposition in shock and corona has to be developed. Not only needs the sample size to be increased, also a larger parameter space has to be covered. One step in this direction will the observation of IM Lup, a relatively old TTS with a disk, but with only weak signatures of accretion. I proposed IM Lup as part of my doctoral work as PI and an observation of 150 ks will be carried out with *Chandra* in the on-going AO.

Also, the shock modelling itself can be improved. Recently an Italian group has presented a very similar model to the one used here, which is non-stationary (Sacco et al., 2008). The results shown in the letter are comparable to our stationary shock models, so they confirm the validity of our assumptions, but they also obtain the depth of the shock in the stellar atmosphere. It seems, that the shock is not buried, but travels outward in the accretion funnel, so only little absorption of the X-rays is to be expected. Although the magnetic field funnels the accretion matter along the flux tubes, so that a one-dimensional approximation seems reasonable, 2D (rotationally

symmetric) or full 3D simulations of the accretion shock should be done in the future to treat inhomogeneous spots. Given the hydrodynamical structure of the accretion spots radiation transfer codes like PHOENIX can be used to provide line profiles for optically thick lines. This could improve our understanding of the FUV line profiles.

Observationally we must look for shock oscillations. This is not trivial, because the count rate in the X-ray regime is not sufficient to resolve short timescales and in the optical the contribution from the photosphere is much stronger than from the shock. In collaboration with S. Dreizler and M. Hundertmark I proposed observations at *SALT* for photometry with subsecond resolution to check for very fast variations and check how far the observed situation deviates from stationarity. Furthermore, I will propose for *GALEX* observations, if a new call for proposals is issued next year in collaboration with G. Herczeg and others. The UV grisms in *GALEX* can resolve line profiles of UV lines like the C IV doublet 1548/1550 Å on time scales of seconds for bright targets and thus allow studies which have not been possible so far.

For the analysis of the X-ray emission produced in the jets, it is essential to obtain more data on DG Tau with *Chandra*, to verify or falsify the idea that the shock is moving along the jet material. An *XMM-Newton* observation can provide a better signal-to-noise ratio due to its larger effective area, and thus the errors on the shock temperature and consequently the errors on the shock velocities and the mass loss rate can be reduced. However, *XMM-Newton* cannot resolve the jet spatially. DG Tau is not the only CTTS with a resolved jet, just the one with the highest luminosity. Observations of comparable objects can test, whether DG Tau is a peculiar object or representative of the class of jet-driving CTTS. On the one hand the future planned X-ray mission *IXO* (formerly *XEUS* and *Constellation-X*) will allow much better CCD spectra due to its larger effective area, on the other hand its spatial resolution will not be sufficient to resolve the jet, so most of these observations have to be done with *Chandra* and will not be possible again until the generation after *IXO*, whose spatial resolution is not known yet and which not be launched within the next two or three decades. Today the observational input on the theory of X-ray jets is marginally, so major developments cannot be expected, before new observations are available.

Studies of the circumstellar environment of CTTS in X-rays, that is the ratio of the absorption column density to the optical determined reddening, are typical byproducts of other programs. With increasing sample size it might be possible to look for correlations between the stellar parameters like inclination or mass accretion rate and the absorption properties. If, e.g., it turns out that only pole-on stars show dust-free absorption, then this could be attributed to stellar winds.

Acknowledgements

I want to thank different people for supporting me in my work for this doctoral thesis and for making my time at the Hamburger Sternwarte a very enjoyable stage of my life.

First of all I want to thank my advisor Prof. Jürgen Schmitt for his advice on all questions I ever asked, personal and scientific ones. His principle to let his students participate in the scientific community through conferences and visits as early as possible has greatly helped me to gain confidence in my own work.

Further I thank my collaborators at the Hamburger Sternwarte (Jan Robrade, Carolin Liefke), at the University of Virginia (Sean Matt and Zhi-Yun Li) and elsewhere (Jan-Uwe Ness). It always was a pleasure to discuss all the magnetic fields and accretion stream and different forms of low number statistics with them.

I am also grateful to the University of Virginia for hosting me in spring 2008, when part of this work was done and to all the inspiring people I met there including all the grad student who included me in their parties straight away. Some institutions I got to know there, like the "Kovalenko Dinner", seemed strange to me, but turned out very favourable.

Additional thanks to "Costa" Wawrzyn and Jan Robrade for proof-reading parts of this thesis.

Greeting and thank goes to all people from the Hamburger Sternwarte, from various conferences, workshops and other scientific occasions for a lot of fun in the field.

Also thanks to my family and friends for everything.

I acknowledge support by the Deutsche Forschungsgemeinschaft, grant number SCHM 1032/29-1, the Deutsches Zentrum für Luft- und Raumfahrt (DLR) under DLR 50OR0105 and the Studienstiftung des deutschen Volkes, which financed my visit to Virginia with a grant.